Pushing Frontiers in Carrier-Envelope Phase Stabilization of Ultrashort Laser Pulses

D I S S E R T A T I O N

zur Erlangung des akademischen Grades

Dr. rer. nat.
im Fach Physik

eingereicht an der
Mathematisch-Naturwissenschaftlichen Fakultät
Humboldt-Universität zu Berlin

von
Dipl.-Phys. Bastian Borchers

Präsident der Humboldt-Universität zu Berlin:
Prof. Dr. Jan-Hendrik Olbertz

Dekan der Mathematisch-Naturwissenschaftlichen Fakultät:
Prof. Dr. Elmar Kulke

Gutachter:
1. Prof. Dr. Thomas Elsässer
2. Prof. Dr. Kurt Busch
3. Prof. Dr. Franz X. Kärtner

Tag der mündlichen Prüfung: 17.10.2014

Abstract

In the last decade, the measurement and stabilization of the carrier-envelope phase has become a mature technology, which offers diverse applications in the fields of frequency metrology and attosecond physics. The most limiting aspects of this technology are the achievable residual phase jitter and the long-term stability.

The present thesis is dedicated to improvements of the carrier-envelope phase stabilization in response to these aspects. In order to realize such improvements, the fundamental noise sources are identified, and suitable measures for their reduction are proposed. It is shown that both, the measurement of the carrier-envelope phase as well as its control are corrupted by different noise contributions.

On the one hand, the detection process is influenced by technical noise sources, which arise especially in the used nonlinear interferometers. It is demonstrated how such limitations can be minimized by a suitable choice of the interferometer topology. On the other hand, the detection noise in the electro-optic conversion represents a fundamental limitation, since the optical shot noise as well as the noise induced by the light detector inevitably influence the measurement of the carrier-envelope phase. A reduction of these constraints is solely achieved for higher detected light fluences, which are quantified in the framework of numerical calculations. On the basis of a numerical optimization of the spectral broadening process in a micro-structured fiber, an enormous improvement of the signal-to-noise ratio by 20 dB is obtained experimentally, which significantly reduces the limitation of detection noise.

So far, the best stabilization results have been achieved with a feed-forward approach, which is based on an acousto-optical frequency shifter. This technique, however, suffers from several constraints that are mainly caused by varying dynamics of the carrier-envelope phase in oscillator pulse trains. A novel double stabilization scheme solves this issue by combining the feed-forward stabilization with a classical feedback loop. This method enabled a reduction of the residual phase jitter to an unprecedented value of 20 milliradians, which corresponds to temporal fluctuations of the carrier-wave with respect to the envelope of only 8 attoseconds. Beyond that, several further concepts are introduced that are capable of stabilizing the CEP without any feedback to the laser oscillator. One of these concepts, referred to as the acoustic frequency comb, represents a pulsed feed-forward stabilization, which is specifically designed for the use in combination with a subsequent amplification stage. First experimental results indicate that residual phase jitters of less than 100 milliradian are within reach also for amplified laser systems.

Zusammenfassung

Die Messung und Stabilisierung der Carrier-Envelope Phase von ultrakurzen Laserimpulsen hat sich im letzten Jahrzehnt zu einer ausgereiften Technologie entwickelt, die vielfältige Anwendungsmöglichkeiten im Bereich der Frequenzmetrologie und der Attosekundenphysik bietet. Die Limitierungen dieser Technologie für derartige Anwendungen sind zum einen das erzielbare Restphasenrauschen und zum anderen die begrenzte Langzeitstabilität der bisher genutzten Ansätze.

Die vorliegende Arbeit ist der Verbesserung der Carrier-Envelope Phasenstabilisierung hinsichtlich dieser Aspekte gewidmet. Zur Realisierung solcher Fortschritte werden die grundlegendsten Rauschquellen identifiziert und geeignete Maßnahmen zu deren Verringerung vorgeschlagen. Es wird gezeigt, dass sowohl die Messung der Carrier-Envelope Phase als auch deren Kontrolle durch verschiedene Rauschbeiträge beeinträchtigt wird.

Der Detektionsprozess ist dabei einerseits durch technische Rauschquellen beeinflusst, die vor allem in den verwendeten nichtlinearen Interferometern auftreten. Es wird demonstriert, wie diese Beschränkungen durch geeignete Wahl der Interferometertopologie verringert werden können. Andererseits repräsentiert das Detektionsrauschen während der elektro-optischen Wandlung eine fundamentale Limitierung, da das optische Schrotrauschen sowie das Rauschen des Lichtdetektors die Messung der Carrier-Envelope Phase unausweichlich beeinträchtigen. Diese Beschränkungen können einzig durch eine Erhöhung der detektierten Lichtstärken verringert werden, was im Rahmen von numerischen Berechnungen quantifiziert wird. Anhand einer numerischen Optimierung des spektralen Verbreiterungsmechanismus in einer mikrostrukturierten Kristallfaser wird experimentell eine enorme Steigerung des Signal-Rauschabstandes um 20 Dezibel erreicht, was die Limitierung durch Detektionsrauschen deutlich reduziert.

Die bisher besten Stabilisierungsergebnisse von Laseroszillatoren wurden mit einem feed-forward Stabilisierungsansatz erreicht, welcher auf einem akustooptischen Frequenzschieber beruht. Dieses Verfahren unterliegt jedoch gewissen Beschränkungen, die im Wesentlichen auf eine variierende Dynamik der Carrier-Envelope Phase in einem Oszillatorpulszug zurückzuführen sind. Dieses Problem wird durch eine neuartige Doppelstabilisierung gelöst, welche die feed-forward Stabilisierung mit einer klassischen Feedback Regelung kombinert. Mit dieser Methode wird das Phasenrestrauschen auf beispiellose 20 Milliradian begrenzt, was zeitlichen Fluktuationen der Trägerwelle gegenüber der Impulseinhüllenden von lediglich 8 Attosekunden entspricht. Darüber hinaus werden weitere neue Stabilisierungskonzepte vorgestellt, die gänzlich ohne Feedback zu dem Laseroszillator auskommen. Bei einem dieser Konzepte, das als akustischer Frequenzkamm bezeichnet wird, handelt es sich um eine gepulste feed-forward Stabilisierung, die speziell für das Zusammenwirken mit einer nachfolgenden Verstärkerstufe konzipiert ist. Erste experimentelle Ergebnisse zeigen, dass zukünftig ein Phasenrestrauschen von weniger als 100 Milliradian auch für Verstärkersysteme möglich sein wird.

Contents

Chapter 1

Introduction

Ultrashort laser pulses with femtosecond pulse durations open interesting opportunities for the investigation of fast fundamental physical processes that cannot be temporally resolved by standard electronic measurement schemes, e.g., molecular dynamics or chemical reactions. While several different techniques for short pulse generation have been invented in the early days of laser science, it is the technique of mode-locking [1, 2] that has succeeded in the generation of the shortest laser pulses. In 1987, external pulse compression techniques led to the generation of optical pulses as short as three optical cycles [3], which, for the first time, questioned the validity of the slowly-varying envelope approximation (SVEA) [4]. Today, broadband Kerr-lens mode-locked Ti:sapphire lasers routinely generate such few-cycle pulses, and even pulse durations in the single-cycle regime have been demonstrated [5, 6]. As a consequence, this class of laser sources has become the workhorse for the whole field of ultrafast laser science.

With pulse durations approaching the few-cycle regime, the relative phase of the carrier wave with respect to the maximum of the intensity envelope starts to play an important role for pulse propagation, see Fig. 1.1. The stabilization of this parameter, which is referred to as the carrier-envelope phase (CEP), is particularly relevant for applications in extreme nonlinear optics, e.g., for the generation of high-harmonic radiation [7, 8], or the related synthesis of even shorter optical pulses with attosecond pulse durations [9]. In a pulse train of a mode-locked laser, however, the mismatch of the intracavity group and phase velocities gives rise to a pulse-to-pulse slip of the CEP. Since the dispersion inside the cavity is strongly influenced by environmental conditions, the slip of the CEP is subject to various external noise sources, necessitating an agile active stabilization scheme.

While this problem has been known for decades [10], it was only in 1996 when Xu *et al.* introduced the first approach for measuring the phase slip of two consecutive pulses with an interferometric cross-correlation technique [11]. Later, a more useful approach based on the heterodyning of different harmonics of the fundamental frequency comb has become the standard CEP detection scheme [12–14]. This

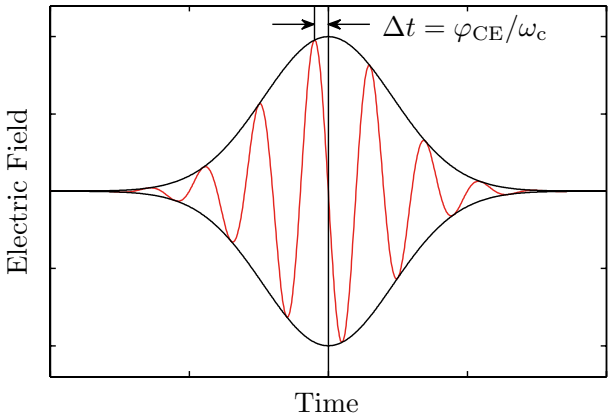

Figure 1.1: A few-cycle laser pulse as a product of the carrier wave oscillating with the angular frequency ω_{c} and the intensity envelope. The delay Δt of the envelope maximum to the closest positive field peak defines the carrier-envelope phase φ_{CE}.

new technology enabled the precise stabilization of frequency combs, which have become indispensable tools in the field of frequency metrology [15, 16], since they provide a direct link between optical and microwave frequencies [17, 18].

Until recently, the stabilization of the CEP relied almost exclusively on feedback schemes, which lock the slip of the CEP to a certain reference oscillator with a phase-locked loop. In 2010, a novel feed-forward type CEP stabilization approach was demonstrated by Koke *et al.*, in which the offset of the frequency comb is controlled with an external acousto-optical frequency shifter [19]. Due to the strongly increased control bandwidth of the feed-forward scheme, the CEP stabilization performance was greatly improved to a residual rms phase jitter of only 45 mrad for a 5 s long measurement, rendering this approach the most advanced CEP stabilization scheme at that time.

Starting from the current state-of-the-art CEP stabilization scheme, this thesis is dedicated to answer the question how far the frontiers in CEP stabilization can be eventually pushed. In this context, one can ask whether or not it is possible to achieve a CEP stabilization performance with zeptosecond (10^{-21} s) timing jitters of the carrier wave with respect to the envelope, and what are the physical mechanisms that ultimately limit such improvements.

In a first step, the fundamental noise sources preventing an exact detection of the CEP have to be identified. Beyond the significant impact of various technical noise contributions, it will be interesting to see to what extent already quantum noise is limiting the observed residual phase jitters. Numerical studies of this aspect should help to pinpoint the most promising measures to improve the accuracy of the CEP

detection. Moreover, new solutions for the remaining shortcomings of the feed-forward type stabilization scheme have to be found in order to push the performance of oscillator CEP stabilization to a new level. Especially in terms of long-term stability, there is still room for improvement, since the feed-forward scheme is susceptible to drifts of the free-running oscillator, which show up as beam pointing variations, fluctuations of the output power, or phase drifts in the stabilized output. Such issues render the integration of a feed-forward stabilization into amplified laser systems difficult, which has to be solved by new stabilization concepts that are specifically designed to meet the requirements for seeding amplifiers.

As a matter of fact, there is still a strong discrepancy between the stabilization performance of amplified laser systems and oscillators. While CEP stabilization of oscillator pulses has meanwhile become a mature technology, the additional noise that arises in the amplification stage typically increases the residual phase jitter of the amplified laser pulses by an order of magnitude. To this end, the most limiting aspects for amplifier CEP stabilization will be identified to find out whether it is possible to improve the stabilization performance to noise levels that are comparable to those of the seed laser.

Outline

After providing an introduction on the basic concepts and methods for the measurement and stabilization of the CEP in chapter 2, the most limiting constraints for the stabilization of mode-locked oscillators are investigated in chapter 3. In the first section of chapter 3, limitations of the CEP detection process are discussed. Here the focus lies on the different noise sources that arise in the individual steps of the CEP measurement, including technical noise as well as quantum noise. Moreover, measures for an improvement of the detection process by an optimization of the supercontinuum generation process are proposed and experimentally proven. In the second section of chapter 3, several new CEP stabilization schemes are presented that aim at the enhancement of the feed-forward stabilization. Particularly, the combination of the feed-forward stabilization with an additional feedback loop is found to further reduce the residual phase jitter.

Finally in chapter 4, the most limiting aspects of the CEP stabilization of amplified laser pulses are treated. The discussion of the technical noise sources in amplifier systems is followed by the introduction of a new stabilization concept that is specifically designed for seeding an amplifier system, solving some of the remaining issues of the feed-forward scheme. In closing, the fundamental limitations of the CEP detection process are revisited again for amplifier pulses, and calculations are presented that provide an overview on which materials are best suited to build a sensitive spectral interferometer least sensitive to detection noise.

Chapter 2

Principles of Carrier-Envelope Phase Stabilization

2.1 Ultrashort Laser Pulses

2.1.1 Mathematical Description

The description of all classical optic phenomena is founded on the set of partial differential equations that were introduced by James Clerk Maxwell in 1861 [20]. The macroscopic version of these equations, which describe the interplay of electric and magnetic fields with matter, are given in SI-units as [21]

$$\nabla \cdot \mathbf{D} = \rho, \tag{2.1.1}$$

$$\nabla \cdot \mathbf{B} = 0, \tag{2.1.2}$$

$$\nabla \times \mathbf{E} = -\frac{\partial \mathbf{B}}{\partial t}, \tag{2.1.3}$$

$$\nabla \times \mathbf{H} = \mathbf{J} + \frac{\partial \mathbf{D}}{\partial t}, \tag{2.1.4}$$

where ρ is the charge density, J the current density, $\mathbf{D} = \epsilon_0 \mathbf{E} + \mathbf{P} = \epsilon \mathbf{E}$ the displacement field in a medium with the polarization $\mathbf{P}$, and $\mathbf{H} = \mathbf{B}/\mu_0 - \mathbf{M} = \mathbf{B}/\mu$ is the magnetic field with magnetization $\mathbf{M}$. While ϵ_0 and μ_0 are the electric permittivity and magnetic permeability of the vacuum, respectively, they are replaced in a medium by the absolute quantities ϵ and μ, which account for the response of the material. In general, ϵ and μ are tensors, however, in the case of an isotropic material they become scalar quantities.

In the absence of free charges and free currents ($\rho = 0, \mathbf{J} = 0$), Maxwell's equations give rise to the wave equations of the electric and magnetic fields,

$$\nabla^2\mathbf{E} - \frac{1}{c^2}\frac{\partial^2\mathbf{E}}{\partial t^2} = 0, \tag{2.1.5}$$

$$\nabla^2\mathbf{B} - \frac{1}{c^2}\frac{\partial^2\mathbf{B}}{\partial t^2} = 0. \tag{2.1.6}$$

Possible solutions of the wave equations are monofrequent, continuous electromagnetic waves that are infinitely extended and propagate at the phase velocity $c = 1/\sqrt{\epsilon\mu}$. Moreover, all superpositions of such plane waves represent solutions as well. In fact, ultrashort laser pulses which are subject of this thesis can be understood as a superposition of plane waves of different frequencies that have a fixed phase relation. Mathematically, the electric field of an optical pulse as a function of space and time $E(t, z)$ is formally given by the Fourier transform of the complex spectral amplitude $\tilde{\mathcal{E}}(\omega, z)$ [22]

$$E(t, z) = \mathcal{F}\left[\tilde{\mathcal{E}}(\omega, z)\right](\omega) = \frac{1}{\sqrt{2\pi}}\int_{-\infty}^{\infty}\tilde{\mathcal{E}}(\omega, z)\mathrm{e}^{i\omega t}\mathrm{d}\omega. \tag{2.1.7}$$

Note that the electric field is now described as a scalar quantity, which is justified for linearly polarized light. In case of elliptically polarized light, one has to employ the full vectorized description if nonlinear effects come into play; otherwise the orthogonal components can be treated independently. As the electric field $E(t, z)$ is a real physical quantity its spectral amplitude has to be self-adjoint: $\tilde{\mathcal{E}}(\omega, z) = \tilde{\mathcal{E}}^*(-\omega, z)$. In many situations it is convenient to describe the electric field by the complex field amplitude $\mathcal{E}(t, z)$ that is obtained by the Fourier transformation of the single-sided spectrum $\tilde{\mathcal{E}}_{\mathrm{ss}}(\omega, z)$

$$\mathcal{E}(t, z) = \mathcal{F}\left[\tilde{\mathcal{E}}_{\mathrm{ss}}(\omega, z)\right](\omega) = \frac{1}{\sqrt{2\pi}}\int_{0}^{\infty}\tilde{\mathcal{E}}(\omega, z)\mathrm{e}^{-i\omega t}\mathrm{d}\omega, \tag{2.1.8}$$

where the connection of the complex and the real electric field is then given by

$$E(t, z) = \mathcal{E}(t, z) + c.c. = 2Re\left[\mathcal{E}(t, z)\right]. \tag{2.1.9}$$

For a given optical pulse one can define the spectral bandwidth $\Delta\omega$ as well as the pulse duration τ, which typically refer to the full width at half maximum (FWHM). It is a general outcome of Eq. (2.1.7) that a broader spectrum enables shorter minimum pulse durations. However, for a given spectral width, the shortest possible pulse duration is only obtained if the spectral phase is flat over the entire spectrum. In this case, the pulse duration is called bandwidth-limited or Fourier-limited. The product of this pulse duration and the spectral width, also referred to as the time-bandwidth product, is a constant parameter and is characteristic for a certain temporal pulse shape: $\tau\Delta\omega = \mathrm{const}$.

In most cases, the spectrum of an optical pulse is centered around a certain mean frequency or carrier frequency, which is defined by

$$\omega_\mathrm{c} = \int_0^\infty \omega \left|\tilde{\mathcal{E}}(\omega)\right|^2 d\omega / \int_0^\infty \left|\tilde{\mathcal{E}}(\omega)\right|^2 d\omega. \tag{2.1.10}$$

If the spectral amplitude contains only frequencies in a small interval around this carrier frequency ($\Delta\omega \ll \omega_\mathrm{c}$), the substitution $\omega \to \omega_\mathrm{c} + \Delta\omega$ separates the field amplitude in a complex envelope $\mathcal{A}(t,z)$ and a term oscillating at ω_c

$$\begin{aligned}
\mathcal{E}(t,z) &= \mathcal{F}\left[\tilde{\mathcal{A}}_\mathrm{ss}(\Delta\omega,z)\right](\Delta\omega)\cdot \mathrm{e}^{-i\omega_\mathrm{c}t} && (2.1.11)\\
&= \mathcal{A}(t,z)\mathrm{e}^{i\omega_\mathrm{c}t} && (2.1.12)\\
&= A(t,z)\mathrm{e}^{i\varphi(t,z)}\mathrm{e}^{-i\omega_\mathrm{c}t}. && (2.1.13)
\end{aligned}$$

Here $\tilde{\mathcal{A}}_{ss}(\Delta\omega,z)$ is the complex spectral amplitude shifted to the baseband, while $A(t,z)$ and $\varphi(t,z)$ represent the envelope and phase of the pulse. This description of optical pulses is only correct if the above mentioned criterion of a narrow spectrum is fulfilled, which is usually referred to as the slowly-varying envelope approximation (SVEA) [4]. As the term implies the approximation only holds if the temporal variation of the envelope is small within one oscillation of the optical field

$$\left|\frac{\partial\mathcal{A}}{\partial z}\right| \ll |k(\omega_\mathrm{c})\mathcal{A}| \quad \text{and} \quad \left|\frac{\partial\mathcal{A}}{\partial t}\right| \ll |\omega_\mathrm{c}\mathcal{A}|\,, \tag{2.1.14}$$

where $k(\omega_\mathrm{c})$ is the wavenumber at the carrier frequency. The generation of ever shorter optical pulses with modern ultra-broadband laser systems down to the few-cycle regime renders the validity of the SVEA more and more questionable. In the near infrared pulse durations of 10 fs, which correspond to only 4 optical cycles, represent the threshold down to which the SVEA and therefore the separation into an envelope and a carrier oscillation still holds. For even shorter laser pulses ($\Delta\omega \approx \omega_\mathrm{c}$) the carrier frequency and the phase of an optical pulse are no longer independent quantities and further use of the SVEA would violate the energy conservation and lead to unphysical DC electric fields. To this end, more sophisticated theories for the description of ultrashort laser pulses have been developed that are applicable even down to the single-cycle regime [23–25].

2.1.2 Propagation in Dispersive Media

Based on the approximations made in the previous section, the propagation of optical pulses is now investigated in dispersive media. In case of linear propagation in a transparent medium, the wave equations (2.1.6) can be transferred into a much simpler differential equation [4]

$$\frac{\partial}{\partial z}\tilde{\mathcal{A}}(\Delta\omega,z) + ik\tilde{\mathcal{A}}(\Delta\omega,z) = 0, \tag{2.1.15}$$

which is readily solved by the ansatz

$$\tilde{\mathcal{A}}(\omega, z) = \tilde{\mathcal{A}}(\omega, 0)e^{ikz}. \tag{2.1.16}$$

Here $k = k(\omega) = \omega n(\omega)/c_0$ is the dispersion relation of the material, which can be expanded in a Taylor series around the carrier frequency

$$k(\omega) = \sum_{m=0}^{\infty} \frac{1}{m!}\beta_m(\omega - \omega_\mathrm{c})^m, \tag{2.1.17}$$

with

$$\beta_m = \left.\frac{\mathrm{d}^m k(\omega)}{\mathrm{d}\omega^m}\right|_{\omega=\omega_\mathrm{c}} \tag{2.1.18}$$

being the propagation parameters. All of these propagation parameters represent different orders of material dispersion and describe the impact on different pulse parameters. Specifically, β_0 and β_1 are related to the phase velocity $v_p = \omega_\mathrm{c}/\beta_0$ and the group velocity $v_g = 1/\beta_1$, respectively. While the former defines the traveling speed of the carrier wave, the latter indicates the speed of the envelope of the pulse. Furthermore, β_2 and β_3 are referred to as group-velocity dispersion (GVD) and third-order dispersion (TOD). Higher order dispersion beyond β_3 will not be considered here. Due to the difference of the phase and group velocity, propagation of a pulse in a dispersive medium causes a phase slip of the carrier wave with respect to the envelope. This so called group-phase offset (GPO) changes a pulse parameter that is typically referred to as the carrier-envelope phase (CEP) or sometimes absolute phase [12, 26]. More precisely, the CEP is defined as the phase difference of the maximum of the pulse envelope and the closest field maximum. Propagation in a medium with the refractive index $n(\omega)$ will induce a GPO

$$\begin{aligned}
\Delta\varphi_\mathrm{GPO}(z) &= \omega_\mathrm{c}\left(\frac{z}{v_g} - \frac{z}{v_p}\right) && (2.1.19)\\
&= \frac{\omega_\mathrm{c} z}{c_0}\left(n_g(\omega_\mathrm{c}) - n(\omega_\mathrm{c})\right) && (2.1.20)\\
&= \frac{\omega_\mathrm{c}^2 z}{c_0}\left.\frac{\mathrm{d}n(\omega)}{\mathrm{d}\omega}\right|_{\omega=\omega_\mathrm{c}}, && (2.1.21)
\end{aligned}$$

where $n_g(\omega_\mathrm{c})$ is the group index at the carrier frequency, which is defined as

$$n_g(\omega_\mathrm{c}) = n(\omega_\mathrm{c}) + \omega_\mathrm{c}\left.\frac{\mathrm{d}n(\omega)}{\mathrm{d}\omega}\right|_{\omega=\omega_\mathrm{c}}. \tag{2.1.22}$$

While the propagation parameters β_0 and β_1 solely act on the CEP and the timing of a pulse, all higher orders will also influence the temporal pulse shape. The group velocity dispersion β_2, for instance, induces a linear chirp to an initially

Fourier-limited Gaussian pulse and increases the pulse duration according to [27]

$$\tau(z) = \tau_0 \sqrt{1 + \left(\frac{4(\ln 2)\beta_2 z}{\tau_0^2}\right)^2}, \tag{2.1.23}$$

where τ_0 is the Fourier-limited duration (FWHM) of a Gaussian pulse. Accordingly, third order or even higher order dispersion causes a nonlinear chirp. It should be noted that dispersion can also be used for the inverse process, i.e., compressing an initially chirped pulse. For this purpose, the dispersion and chirp parameters must have opposite signs.

The previous treatment of linear propagation has fully neglected material absorption. However, as real dispersive materials with a refractive index $n(\omega)$ inherently possess also an absorption function $\alpha(\omega)$, the ansatz in Eq. (2.1.16) has to be expanded by an additional absorption term. Generally, dispersion and absorption are related to the real and imaginary part of the dielectric function according to

$$\epsilon(\omega) = 1 + \chi^{(1)}(\omega) = \left(n(\omega) + i\frac{c}{2\omega}\alpha(\omega)\right)^2. \tag{2.1.24}$$

Here $\chi^{(1)}(\omega)$ is the linear susceptibility that describes the materials response in the frequency domain, which is connected to the polarization by $\tilde{P}(\omega) = \epsilon_0 \chi^{(1)}(\omega)\tilde{E}(\omega)$. The fact that absorption and dispersion are two intrinsically related phenomena is quantified by the Kramers-Kronig relation [28, 29]

$$n(\omega) - 1 = \frac{c}{\pi}\int_0^\infty \frac{\alpha(\Omega)}{\Omega^2 - \omega^2}\mathrm{d}\Omega, \tag{2.1.25}$$

which is a general consequence of causality and is observed also in electronic or acoustic wave systems.

Nonlinear Propagation

If the optical intensity $I = cn\epsilon_0 |E|^2 /2$ of an ultrashort laser pulses becomes as high as some TW/cm^2 the response of optical media starts to deviate from the linear behavior that has been assumed so far. Under these conditions the polarization is expanded in a Taylor series for the electric field

$$P(t) = P_\mathrm{L}(t) + P_\mathrm{NL}(t) = \epsilon_0 \left(\chi^{(1)}E(t) + \chi^{(2)}E^2(t) + \chi^{(3)}E^3(t) + \dots\right), \tag{2.1.26}$$

with $\chi^{(n)}$ being the nth order susceptibility, which is a tensor of rank $n+1$. While even-order susceptibilities vanish in all centro-symmetric materials [30], such as gases, liquids and most crystals, they are observed solely in materials without inversion symmetry. Propagation under the influence of such nonlinearities can lead to the generation of new frequency components. A prerequisite for efficient

frequency conversion, however, is that the radiation generated at different positions within the material interferes constructively with each other, which is referred to as *phase matching*. The nonlinear processes that are most relevant for the experiments presented in this thesis are second harmonic generation (SHG), difference frequency generation (DFG) and four-wave mixing (FWM) and will be treated later in more detail.

2.2 Mode-Locking

The generation of the ultrashort laser pulses that are considered throughout this thesis is only possible by a process known as mode-locking. The first demonstration of this technique in 1964 [1, 2] triggered the development of laser systems that eventually succeeded to generate optical pulses as short as a few optical cycles [5] and paved the way for the whole new field of ultrafast laser science. The process of mode-locking can be understood as the simultaneous lasing of a large number of longitudinal cavity modes

$$\nu_m = \frac{mc_0}{2nL} \tag{2.2.1}$$

that have a fixed phase relation, with L being the length of the cavity. The superposition of many phase-locked modes can result in a periodic concentration of light in short time intervals of constructive interference that are separated by the cavity round trip time $T_\mathrm{R} = L/c_0$ and destructive interference between these events. In analogy to the spectral phase of a Fourier-limited pulse, the production of short pulses by the process of mode-locking requires the phases of the individual modes to be not only coupled but also nearly constant over the entire spectral bandwidth.

Assuming that a number $N = 2M + 1$ of longitudinal modes of equal weight and identical spectral phases are superimposed, the resulting electric field reads [31]

$$\mathcal{E}(t) = \sum_{m=-M}^{M} \mathcal{E}_0 \exp\left[i(\omega_\mathrm{c} + 2\pi m\delta\nu)t\right] \tag{2.2.2}$$

$$= \mathcal{E}_0 \frac{\sin\left(N\delta\nu t/2\right)}{\sin\left(\delta\nu t/2\right)} \exp\left(i2\pi\omega_\mathrm{c} t\right), \tag{2.2.3}$$

where $\mathcal{E}_0$ is the complex field amplitude of all modes and $\delta\nu$ is the spectral mode spacing. The resulting pulse duration in this ideal case is approximately given by the inverse total bandwidth $\tau \approx 1/N\delta\nu$, showing that the generation of pulses with fs pulse durations requires mode-locking of many THz wide spectra. With typical oscillator repetition rates ranging from several 10 MHz to some 10 GHz the total number of locked cavity modes can therefore vary between hundreds and several millions.

The process of mode-locking can be obtained either by active or passive techniques. In active mode-locking, depicted in Fig. 2.1, the synchronization of the spectral phases is achieved via periodic modulation of the amplitude (AM) or phase/frequency (FM). If the modulation is done at a frequency that matches the mode spacing $\delta\nu$, the generated sidebands of a longitudinal mode coincide with the neighboring modes and tend to *injection lock* these resonant modes, which then oscillate in phase at the exact same frequency. Cascading of this process, see Fig. 2.1(c), will eventually create a broad frequency comb of many equidistant locked modes within the gain curve of the laser material. In the time domain, see Fig. 2.1(b), this comb is equivalent to a train of short pulses, which are created each time when the pulse circulating inside the cavity hits the output coupler.

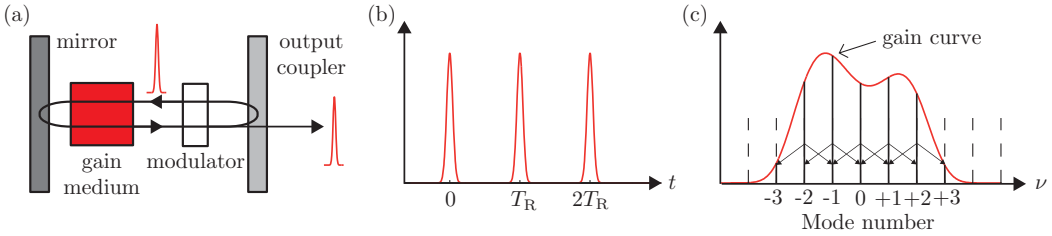

Figure 2.1: (a) Schematics of active mode-locking. (b) Temporal output of a mode-locked oscillator. (c) Active mode-locking in the spectral domain.

Apart from the technique presented above, mode-locking is also possible by passive means. In passive mode-locking, the amplitude modulation is induced by the optical pulse itself, which is thus referred to as *self-amplitude modulation* (SAM). This process can be realized if a saturable absorber (SA) is placed inside the cavity, the optical transmission of which increases with the intensity. If the lasing process starts with initially unlocked modes, the highest of the randomly distributed intensity spikes will be amplified until it reaches the intensity level at which the bleaching of the SA becomes relevant. In the following, the intense spike experiences less attenuation than the rest of the initial intensity noise and gains more amplification in subsequent cavity roundtrips. Finally, a steady state can be obtained in which the light is concentrated into a single short pulse that is circulating inside the cavity.

The first demonstration of passive mode-locking in 1966 was based on a dye solution as a SA [32], where the bleaching was caused by the depopulation of the ground state of the dye molecules. Nowadays, passive mode-locking is mostly based on the excitation of electrons from the valence band to the conduction band in semiconductors [33] or carbon nanotubes [34]. The lifetime of the induced transparency τ_A represents a limitation for the achievable pulse duration in SAM based mode-locking. While the lifetimes τ_A in dye solutions range from tens of picoseconds up to nanoseconds, the fastest relaxation processes in semiconductors, due to intraband thermalization, can be as fast as 100 fs, which makes these materials preferable for

short pulse generation.

An alternative passive mode-locking approach employs reactive nonlinearities far from resonance to mimic the saturable absorption behavior of real optical transitions. As these nonlinear processes can be considered quasi-instantaneous, i.e., having response times of less than a femtosecond [35], they enable passive mode-locking down to the few-cycle regime. Various mode-locking techniques based on such nonlinearities have been developed, e.g., *nonlinear polarization rotation* in fiber lasers [36, 37] or *additive-pulse mode-locking* of bulk lasers [38, 39]. However, the most relevant technique is certainly *Kerr-lens mode-locking* (KLM) [40, 41], which is typically used in modern Ti:sapphire oscillators. These light sources represent the workhorse of ultrafast laser science and will be considered throughout this thesis. In KLM the nonlinear refractive index of a $\chi^{(3)}$ medium

$$n = n_0 + n_2 I \tag{2.2.4}$$

causes a self-focusing of typical spatial beam profiles, as shown in Fig. 2.2. The higher the intensity maximum at the center of the beam, the stronger is the self-focusing effect. In combination with an aperture placed behind the Kerr-medium the sequence acts as an effective SA, since stronger intensity spikes experience less attenuation.

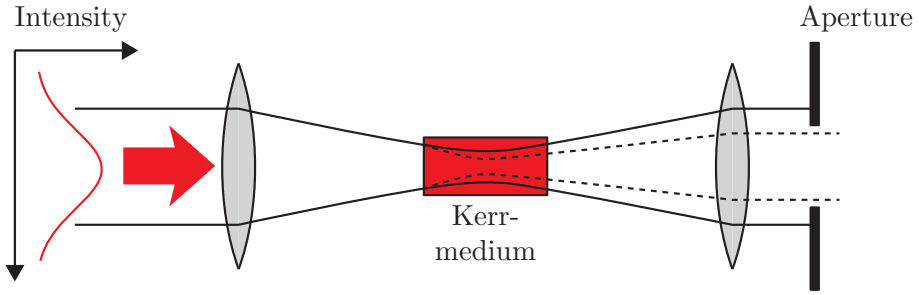

Figure 2.2: Schematic of Kerr-lens mode-locking

Independent from the self-amplitude modulation process, the generation of ever shorter optical pulses renders the dispersion management in the laser cavity more and more important. In fact, the balance of the nonlinear self-phase modulation (SPM) and a net negative group delay dispersion (GDD) is necessary to create self-stabilizing soliton-like pulses after every cavity roundtrip [42, 43]. While intracavity dispersion management was classically achieved by the use of prism or grating sequences, the invention of chirped mirrors [44] represented a breakthrough in this respect. The freedom in the design of these stacked dielectric mirrors allows the control of higher order dispersion, which enabled the generation of optical pulses as short as 4.5 fs directly from a KLM Ti:sapphire oscillator [5].

2.3 The Carrier-Envelope Phase of Mode-Locked Oscillators

In this section the outcomes of the two previous sections about short pulse propagation and mode-locking are combined to a general description of the carrier-envelope phase evolution in mode-locked oscillator pulse trains.

As discussed in section 2.1.1 optical pulses can be described as a carrier-wave multiplied with an envelope function, where the CEP defines the position relative to each other

$$\mathcal{E}(t) = A(t)e^{i(\omega_c t+\varphi_{CE})}. \tag{2.3.1}$$

Furthermore, propagation in a dispersive medium changes the CEP due to the difference of group and phase velocities. According to Eq. (2.1.21), the acquired GPO for one full roundtrip in the laser cavity is calculated by

$$\Delta\varphi_{GPO} = \frac{\omega_c^2}{c_0}\int_0^L \frac{\mathrm{d}n(\omega,z)}{\mathrm{d}\omega}\bigg|_{\omega=\omega_c} \mathrm{d}z, \tag{2.3.2}$$

where $n(\omega, z)$ is the refractive index along the optical path of length L. Apart from the cavity mirrors and the beam path in air, a major part of the dispersion is typically introduced by the laser crystal. For a Ti:sapphire oscillator crystal of a few millimeters length, the GPO is on the order of a hundred optical cycles [12]. Note that there is also a contribution to the GPO from the nonlinear refraction inside the gain medium $n = n(I)$, which has been neglected in Eq. (2.3.2). Despite the high intracavity peak intensities, this nonlinear effect is usually only on the order of a few cycles. Nevertheless, the nonlinear dispersion provides a convenient way to control the CEP of oscillators, as will be discussed in the next section.

Since CEP shifts of 2π or integer multiples thereof do not change the actual field structure of a pulse, the CEP difference of two successive pulses reduces to

$$\Delta\varphi_{CE} = \Delta\varphi_{GPO} \bmod 2\pi. \tag{2.3.3}$$

In a train of pulses, as shown in Fig. 2.3(a), this phase difference corresponds to a steady drift rate of the CEP that is referred to as the carrier-envelope frequency (CEF)

$$f_{CE} = f_{rep}\frac{\Delta\varphi_{CE}}{2\pi}. \tag{2.3.4}$$

Considering the above results, an optical pulse train emitted by an oscillator with the roundtrip time T_R is described as a convolution of Eq. (2.3.1) with a delta

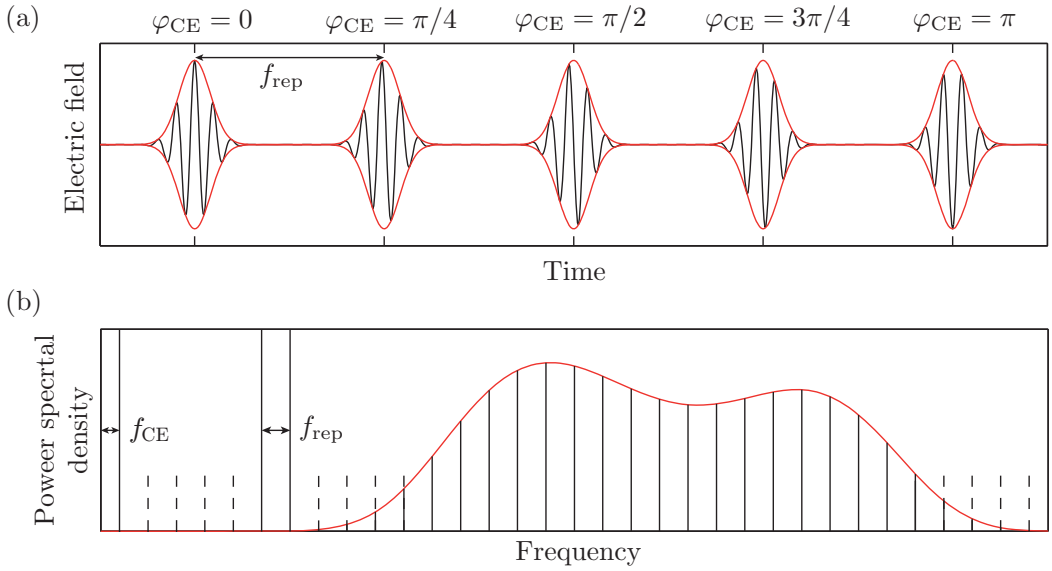

Figure 2.3: (a) Pulse train with constant pulse-to-pulse CEP slip $\Delta\varphi_{CE} = \pi/4$. (b) Corresponding frequency comb with offset f_{CE}

comb function [45]

$$\mathcal{E}(t) = \left[A(t)e^{i\omega_c t} \otimes \sum_{m=-\infty}^{\infty} \delta(t - mT_R)\right] \exp\left(i\omega_{CE} t\right), \tag{2.3.5}$$

with $\omega_{CE} = 2\pi f_{CE}$. In the spectral domain, the term in brackets in Eq. (2.3.5) corresponds to a frequency comb with mode spacing $f_{rep} = 1/T_R$ and spectral amplitude $\tilde{\mathcal{A}}(\nu)$, while the harmonic term $\exp\left(i\omega_{CE} t\right)$ leads to a common offset of this frequency comb, see Fig. 2.3(b).

$$\tilde{\mathcal{E}}(\nu) = \tilde{\mathcal{A}}(\nu - \nu_c - f_{CE}) \sum_{m=-\infty}^{\infty} \delta(\nu - m f_{rep} - f_{CE}). \tag{2.3.6}$$

The spectral position of every single mode within this frequency comb is defined simply by the two parameters $\{f_{CE}; f_{rep}\}$ and the respective mode index m:

$$\nu_m = f_{CE} + m f_{rep}, \qquad m \in \mathbb{N}. \tag{2.3.7}$$

Given that the uniformity of such mode-locked frequency combs has been tested to a precision of better than 6 parts in 10^{16} [46], these combs represent a ruler in the frequency domain with enormous accuracy and broad spectral coverage at the same time. Therefore, frequency combs represent a direct link between optical and microwave frequencies, which had been provided before solely by very complex and costly harmonic frequency chains at large scale facilities [17]. These features

make frequency combs from mode-locked oscillators a unique tool for applications in frequency metrology [15, 47, 48] and spectroscopy [49–51]. The steadily increasing precision of frequency standard measurements and their comparison [52, 53] even opens a path towards experiments that eventually may allow for testing the constancy of fundamental physical constants [54].

A prerequisite for the all the above-mentioned applications is the ability to measure and control both frequency comb parameters, the mode spacing f_{rep} as well as the offset frequency f_{CE}. While the repetition rate of an oscillator is readily measured with a simple photodiode, the offset of the frequency comb is not directly accessible. The techniques that provide access to this parameter will be discussed in the following section.

Apart from applications that are based on the spectral properties of frequency combs, there is a whole different class of applications that is preferably discussed in the time domain. The ability to control the exact field structure of intense few-cycle pulses, for instance, facilitates the generation of isolated attosecond pulses by the emission of high harmonic radiation [9]. According to Corkum's semi-classical three-step model [55], the interaction with high-intensity optical pulses excites short bursts of photo electrons for each optical half-cycle at the instant of the electric field maximum. Subsequently the electrons are accelerated in the driving laser field and finally recollide with the parent ions under emission of highly energetic photons, which can have energies up to several hundred electron volts. This process generates a burst of several UV attosecond pulses depending on the number of half-cycles that are contained in the driver pulse. In order to isolate single attosecond pulses, special filtering [9, 56] or gating techniques [57] have to be applied, all of which require the precise control of the electric field structure of the driving laser pulse. In fact, CEP stabilization of intense ultrashort few-cycle pulses made the generation of isolated attosecond pulses shorter than 100 as possible [58, 59]. From this perspective, it is evident that CEP detection and its stabilization is one of the enabling techniques for the currently active field of attosecond research [60–63].

2.4 Carrier-Envelope Phase Detection

Today many different schemes for the characterization of ultrashort optical pulses exist that rely on the nonlinear interaction with either replicas of the pulse itself or some well known reference pulse [64–66]. Even though the more advanced techniques, such as *frequency resolved optical gating* (FROG) [65] and *spectral phase interferometry for direct electric-field reconstruction* (SPIDER) [66], allow the retrieval of the spectral envelope and its phase in order to reconstruct the temporal shape of the pulses, none of these techniques provides access to the actual CEP nor its slippage rate.

The first successful approach to measure the so far inaccessible parameter $\Delta\varphi_{\mathrm{CE}}$ was demonstrated by Xu *et al.*, who employed a nonlinear cross-correlation of successive pulses [11]. This approach, however, has proven to be impractical as the

cross-correlation requires several meter long interferometer arms, which are difficult to isolate against external noise and therefore prevent accurate measurements. Only recently, a related scheme was developed that works without any nonlinearity and is based on a slightly off-resonant ring cavity [67, 68]. Although these techniques have the advantage of being applicable to many different kind of laser sources they fail to measure f_{CE} with better than MHz precision. To this end, measurement of f_{CE} is nowadays dominated by a different class of techniques that relies on the interference of different harmonics of the fundamental frequency comb in regions of spectral overlap [12]. This approach finally became feasible with the advent of octave-spanning frequency combs [14] and is most commonly realized by heterodyning the fundamental comb with some second harmonic or difference frequency radiation at the spectral wings [14, 69]. For the sake of completeness, it should be noted that also balanced homodyne detection can be used for CEF detection [70, 71], which, however, relies on the same basic principle of spectral interference as the heterodyne detection scheme that is thoroughly discussed in the following section.

2.4.1 RF-Heterodyning

The current standard techniques for oscillator CEP detection are referred to as f-$2f$ interferometry and 0-f interferometry, as they are based on heterodyning of the fundamental spectrum either with its second harmonic or with some difference frequency radiation, respectively. In order to understand how these techniques provide access to the CEP slippage in the pulse trains, it is necessary to study the behavior of the spectral phases $\phi(\omega)$ upon the nonlinear conversion steps that are involved, such as SHG, DFG and FWM. Assuming a pulse train with a constant CEP slip, the CEP for the nth pusle reads as $\varphi_{\mathrm{CE}}^{n} = n\Delta\varphi_{\mathrm{CE}}$, if we arbitrarily choose $\varphi_{\mathrm{CE}}^{0} = 0$. The temporal and spectral representations of the nth pulse are given by

$$\mathcal{E}(t)^{n} = A(t)e^{i\left(\omega_{\mathrm{c}}t+\varphi_{\mathrm{CE}}^{n}\right)} = \frac{1}{\sqrt{2\pi}}\int \tilde{\mathcal{E}}(\omega)e^{i\left(\varphi_{\mathrm{CE}}^{n}+\varphi(\omega)-\omega t\right)}\mathrm{d}\omega, \tag{2.4.1}$$

where the spectral phase $\phi^{n}(\omega)$ is decomposed into the value at the carrier frequency $\varphi_{\mathrm{CE}}^{n}$ and the spectrally dependent relative phase $\varphi(\omega)$, which defines the pulse shape and is identical for all pulses. It is now important to see that in case of nonlinear frequency conversion the spectral phases and therefore also the CEP behave essentially the same as the frequencies [72]. Typically in f-$2f$ interferometry, but also in 0-f interferometry, the initial spectrum has to be broadened in a first step by a FWM process to generate an octave-spanning spectrum, which later ensures the spectral overlap with the frequency-converted light. It can be shown that such FWM processes preserve the initial CEP [72], except for some additional

constant phase lag $\pi/2$ that stems from the Maxwell equations [73].

$$\begin{aligned} \omega_{\mathrm{FWM}} &= \omega_1 + \omega_2 - \omega_3 && (2.4.2)\\ \varphi^n_{\mathrm{CE,FWM}} &= \pi/2 + \varphi^n_{\mathrm{CE}} + \varphi^n_{\mathrm{CE}} - \varphi^n_{\mathrm{CE}} && (2.4.3)\\ &= \pi/2 + n\Delta\varphi_{\mathrm{CE}}. && (2.4.4) \end{aligned}$$

Here ω_{FWM} is the new frequency component that is generated by FWM of an arbitrary set of frequencies from the initial spectrum $\{\omega_1, \omega_2, \omega_3\}$. As a result, spectral broadening can be used for white-light generation while maintaining a high degree of spectral coherence [74]. The processes that are commonly used for supercontinuum generation will be treated in more detail in section 2.4.3.

The same analysis for SHG [72] reveals that in this case the CEP is doubled, just as the CEP slip $\Delta\varphi_{\mathrm{CE}}$ is doubled, except for the constant phase lag $\pi/2$:

$$\begin{aligned} \omega_{\mathrm{SHG}} &= 2\omega && (2.4.5)\\ \varphi^n_{\mathrm{CE,SHG}} &= \pi/2 + 2\varphi^n_{\mathrm{CE}} && (2.4.6)\\ &= \pi/2 + 2n\Delta\varphi_{\mathrm{CE}}. && (2.4.7) \end{aligned}$$

In the terminology of a frequency comb, this result is equivalent to a comb mode ν_m that is frequency-doubled according to

$$2\nu_m = 2f_{\mathrm{CE}} + 2mf_{\mathrm{rep}}. \tag{2.4.8}$$

If the frequency comb fulfills the condition of an octave-spanning spectrum and if the frequency-doubled mode originates from the long-wavelength wing, as shown in Fig. 2.4, this newly generated comb mode lies in the short-wavelength wing of the fundamental comb, close to the mode $\nu_{2m} = f_{\mathrm{CE}} + 2mf_{\mathrm{rep}}$. According to the mathematical representations of the fundamental and the second harmonic frequency comb, the difference frequency of these two modes is equal to the comb offset f_{CE}. If, next to the spectral overlap, also spatial and temporal overlap of the fundamental and frequency-doubled components is established with a suitable nonlinear interferometer, the beat of the neighboring modes results in an amplitude modulation of the pulse train that is detectable with an avalanche photodiode (APD) [12].

The same considerations can be made for the case of 0-f interferometry, where DFG within the fundamental comb produces comb modes of vanishing offset ($\nu_n = nf_{\mathrm{rep}}$) at the long-wavelength wing, see Fig. 2.5. Again, the difference frequency of two neighboring modes ($n = m$) in the region of spectral overlap yields a comparable beat signal that provides access to the carrier-envelope frequency,

$$\nu_m - \nu_n = f_{\mathrm{CE}} + mf_{\mathrm{rep}} - nf_{\mathrm{rep}} = f_{\mathrm{CE}}. \tag{2.4.9}$$

Figure 2.6 shows an amplitude modulated pulse train, as it is typically measured at the detection front-end of an f-$2f$ interferometer, as well as the corresponding

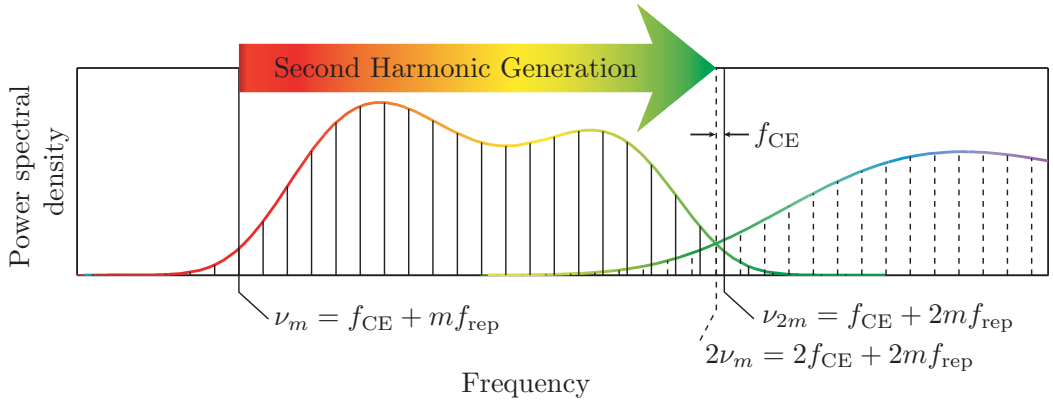

Figure 2.4: f-$2f$ interferometry: Beat signal generation in the region of spectral overlap of the fundamental and second harmonic frequency comb.

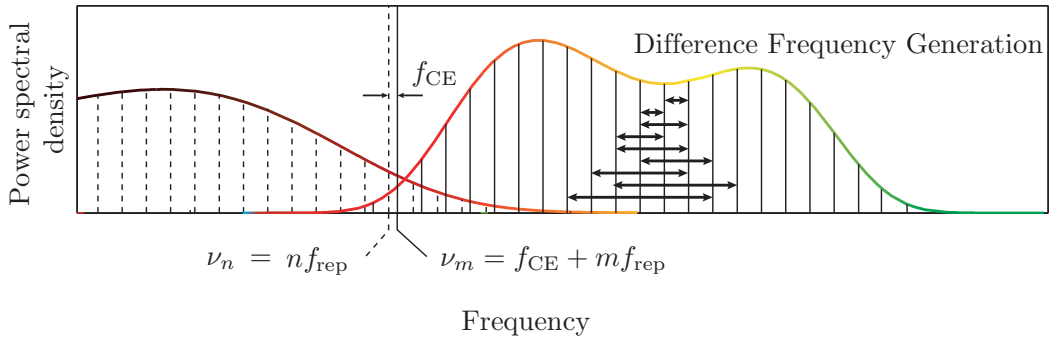

Figure 2.5: 0-f interferometry: Beat signal generation in the region of spectral overlap of the fundamental and the difference frequency comb.

RF power spectrum. Apart from the so-called *intermode beat* at f_{rep}, the beating results in two peaks that are symmetrically centered around $f_{\mathrm{rep}}/2$ at the positions f_{CE} and $f_{\mathrm{rep}} - f_{\mathrm{CE}}$. Due to the high number of modes in the region of spectral overlap, the spectrum on the interval $[0, f_{\mathrm{rep}}]$ is periodically repeated, as indicated in Fig. 2.6(b). From a first inspection of the power spectrum it is not immediately clear which one of the two peaks is the "real" beat signal that behaves according to Eq. (2.3.4), since it can be located anywhere on the interval $[0, f_{\mathrm{rep}}]$. In order to distinguish the "real" beat from the mirror beat, e.g., for a potential subsequent stabilization scheme, one has to change the dispersion and observe the opposite shift of the beats.

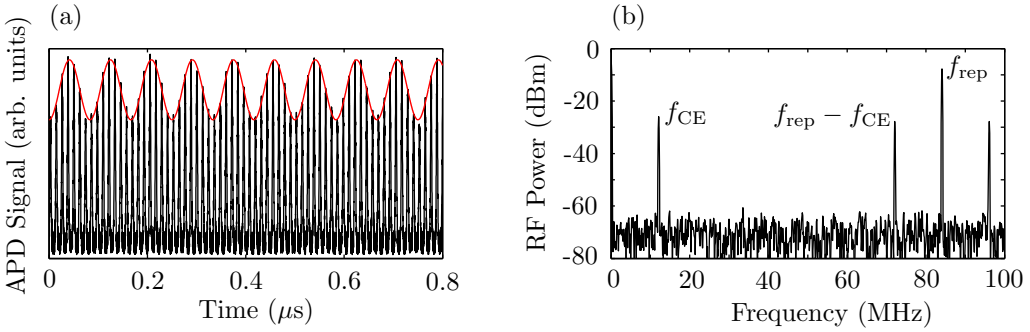

Figure 2.6: (a) Amplitude modulation of a pulse train generated by f-$2f$ interferometry. (b) Corresponding RF power spectrum.

Even though the f_{CE} signal only represents the slippage rate of the CEP and does not allow the measurement of the absolute CEP, it still contains the phase relative to some arbitrary moment in the past, provided that the f_{CE} signal has since been measured without interruption. This requires, however, that no additional interferometer phase drift has occured within the measurement time. In fact, the most stable monolithic interferometers allow the phase coherence to be maintained over many hours or even days [75].

In practice, different types of interferometers can be used to generate the overlap in the spatial, temporal, and spectral domain. The most straightforward realization is a Mach-Zehnder interferometer with two separate arms of variable length for the f and $2f$ components. After splitting the initial spectrum with a dichroic mirror, spectral content from the long-wavelength part is frequency-doubled in a suitable nonlinear crystal and subsequently recombined with the fundamental spectrum. If the arm lengths are correctly tuned, a signal, as shown in Fig. 2.6, is detected with a sensitive APD that is optimized for the respective wavelength range. Other possible interferometer types include collinear or partially collinear designs, which all have their pros and cons. The benefits from the different interferometer geometries will be discussed later in relation to the experiments that were conducted for oscillator CEP stabilization.

2.4.2 Spectral Interferometry

The CEP detection method presented in the previous section works well for oscillator systems with repetition rates in the MHz or GHz range, but runs into problems for amplifier systems at the kHz level or below. The CEP stable operation of an amplifier usually requires a preceding oscillator stabilization, with the exception of the passive stabilization scheme that is used for optical parametric amplifiers [72]. Therefore the phases of the amplified pulses are already locked to a certain value and exhibit only some residual phase jitter and explicitly no steady slip, as observed in an oscillator pulse train. The amount of residual noise is thereby determined by the oscillator stabilization performance and the noise that is added during the amplification process. As the CEP measurement with the heterodyning scheme used for oscillators is prevented at the DC baseband due to $1/f$ noise contributions, an alternative measurement scheme based on spectral interference is typically used for amplifiers, which is capable of resolving CEP fluctuation, in principle, on a single-shot basis [76, 77].

This approach also relies on the interference of different harmonics as the RF heterodyning presented above, but the intentional introduction of a relative delay τ_D between the different harmonics creates a spectral fringe pattern, whose spectral position is directly linked to the CEP. Taking Eq. (2.4.7) into account, the intensity distribution in the region of spectral overlap reads

$$
\begin{aligned}
I(\omega) &\propto \left|\tilde{\mathcal{E}}(\omega) + \tilde{\mathcal{E}}_\mathrm{SHG}(\omega)\right|^2 && (2.4.10)\\
&= \left|\tilde{\mathcal{A}}(\omega-\omega_\mathrm{c})e^{i\varphi_\mathrm{CE}} + \tilde{\mathcal{A}}_\mathrm{SHG}(\omega-\omega_\mathrm{c})e^{i(2\varphi_\mathrm{CE}+\pi/2+\omega\tau_\mathrm{D})}\right|^2 && (2.4.11)\\
&= \left|\tilde{\mathcal{A}}(\omega-\omega_\mathrm{c})\right|^2 + \left|\tilde{\mathcal{A}}_\mathrm{SHG}(\omega-\omega_\mathrm{c})\right|^2 + && (2.4.12)\\
&\quad 2\cdot\left|\tilde{\mathcal{A}}(\omega-\omega_\mathrm{c})\tilde{\mathcal{A}}_\mathrm{SHG}(\omega-\omega_\mathrm{c})\right|\cdot\cos\left(\varphi_\mathrm{CE}+\pi/2+\omega\tau_\mathrm{D}\right), && (2.4.13)
\end{aligned}
$$

where the last term represents the CEP dependent spectral modulation. In principle, this method allows measuring the absolute value of the CEP, however, in practice the constant but unknown phase added by the interferometer makes an absolute determination impossible. A further limitation of this scheme is given by the read-out speed of the spectrograph detectors, which can impede single shot measurements and make averaging over multiple pulses necessary. To this end, fully analog detection schemes have been developed, which reduce the latency to a minimum and enable single-shot detection at even higher repetition rates [78].

It should be noted that apart from spectral interferometry another class of amplifier based CEP measurement schemes has emerged, which utilizes the strong CEP dependence of multi-photon absorption (MPA) processes, e.g., the emission of photo-electrons from metal cathodes [79, 80] or the ionization of noble gases [81–83]. The latter methods determine the absolute value of the CEP from the asymmetry in the photo-electron yield from a laser focus with two opposing detectors. Although such stereo above-threshold ionization (ATI) methods have reached

a high degree of detection accuracy on the single-shot level [82], they have been used exclusively for CEP logging and hence still require some additional stabilization mechanism. The same applies so far to the recently introduced solid-state light-phase detector [84], which monitors the CEP by the measurement of electric currents in a metal-dielectric-metal nanojunction.

2.4.3 Supercontinuum Generation

The discussion of f-$2f$ interferometry and comparable techniques has shown that an octave spanning spectrum is a necessary condition to ensure the spectral overlap of the fundamental and frequency-doubled components. As most common laser oscillators are far from providing such broad spectral content, additional broadening techniques have to be applied. The same is valid for amplified laser pulses that typically provide even narrower spectra. As the amount of pulse energy that is available for the spectral broadening in oscillator and amplifier systems differs by several orders of magnitude, different approaches are chosen to perform this task.

Supercontinuum generation of amplified laser pulses

The generation of white-light from amplified laser pulses is typically achieved by a filamentation process in either solid, liquid, or gaseous media. A filament is formed in a medium if the laser power exceeds a certain critical power, which is given by [85]

$$P_{\mathrm{crit}} = \frac{3.77\lambda^2}{8\pi n_0 n_2}. \tag{2.4.14}$$

Under this condition the self-focusing action due to the Kerr effect, see section 2.2, is overcompensating the linear diffraction. As a result, the beam profile starts to collapse until it is finally arrested by the defocusing effect of the plasma that has built up by multi-photon ionization at a certain clamping intensity I_{clamp} [86, 87]. The balance of the two counteracting effects can lead to propagation of a filament over many centimeters in solids or even many meters in gases without lateral beam expansion, which is sometimes referred to as "non-diffracting" propagation. Interaction of a pulse with the medium in such filaments at extreme intensities in the range of TW/cm^2 significantly influences the spectral and the temporal shape. Since the optical phase of a pulse is influenced by the temporally varying nonlinear refractive index

$$\varphi(t,z) = \omega_{\mathrm{c}} t - kz = \omega_{\mathrm{c}} t - \frac{2\pi}{\lambda} n\left(I(t)\right) z, \tag{2.4.15}$$

it is helpful to define the momentary frequency as its temporal derivative:

$$\omega(t,z) = \frac{\mathrm{d}\varphi(t)}{\mathrm{d}t} = \omega_{\mathrm{c}} - \frac{2\pi z}{\lambda} n_2 \frac{\mathrm{d}I(t)}{\mathrm{d}t}. \tag{2.4.16}$$

The self-phase modulation (SPM) in the last term of Eq. (2.4.15) leads to the generation of new frequency components in case of a sufficiently steep intensity profile $I(t)$. These new frequency components are red-shifted on the leading edge of the pulse and blue-shifted on the trailing edge. For a temporally symmetric Gaussian pulse, SPM gives rise to a symmetrically broadened spectrum, which is modulated due to interference of frequency components generated in the leading and trailing edge of the pulse [88].

In the case of ultrashort few-cylce pulses, the nonlinear refraction gives rise to a self-steepening effect. This phenomenon is explained by the higher velocity in the trailing edge of the pulse that makes the latter eventually catch up with the slower pulse maximum. Hence, a very steep trailing pulse edge is formed that is referred to as an optical shock wave [89]. The result is an asymmetrically broadened spectrum that is pronounced on the blue side. Incorporation of dispersion effects up to various orders and a detailed description of the plasma build-up renders the modeling of the filamentation particularly complex [86, 87, 90, 91], which is why laser filamentation is still an active field of research. Recently, e.g., a filamentation experiment on the possible role of higher-order contributions to the Kerr effect in air acquired some attention, as it can explain filamentation without the necessity for plasma formation [92–95].

Nonetheless, already the basic theory of strong self-phase modulation by Yang and Shen [96] predicts the usually observed asymmetric broadening that is stronger on the anti-Stokes than on the Stokes side [97]. They found that the relative spectral broadening is described as

$$\frac{\Delta\omega_{\pm}}{\omega_{\mathrm{c}}} = 1/2\left(\sqrt{Q^2+4} \pm |Q|\right) - 1, \tag{2.4.17}$$

where $\Delta\omega_{\pm}$ is the spectral width on the anti-Stokes and Stokes side. The parameter Q depends on the clamping intensity, the propagation distance z and the pulse duration τ according to $Q = 2n_2 z I_{\mathrm{clamp}}/c_0\tau$. The condition of an octave-spanning spectrum is achieved at $Q = 0.707$, which defines the necessary filament length for a given pulse duration. Experimental studies have shown that the broadening is even more pronounced on the anti-Stokes side, the higher the bandgap of the material is [97]. Moreover, it was demonstrated that also the focusing geometry has some effect on the achievable spectral width [98]. In practice, the materials that are most commonly used for white-light generation from amplified laser pulses are wide-bandgap bulk materials such as sapphire or calcium fluoride.

Supercontinuum generation of oscillator frequency combs

In contrast to the situation of amplifiers, where the available pulse energies are in the μJ or even mJ range, the generation of supercontinua from oscillator pulses at the nJ level is far more challenging due to the weaker nonlinear effects. In principle, it is possible to compensate for this handicap in two different ways. First,

the interaction length with the nonlinear medium can be increased and second, the light can be confined to smaller cross-sections. The first approach is readily achieved by coupling the light into a standard optical fiber, which enables the spectral broadening to some extent by SPM [27] similar to the broadening in bulk materials. The generation of octave-spanning spectra, however, was not possible until the invention of the photonic crystal fiber (PCF) [99], which also addresses the aspect of a stronger confinement. These micro-structured fibers guide the light in a tiny core of only a few micrometer diameter that is surrounded by a photonic structure. The drastic enhancement of the nonlinear interaction in these fibers led to the first observation of supercontiuum generation at the oscillator pulse level [100]. Already shortly after this breakthrough it was found that also tapered fibers, in which the core diameter is gradually reduced down to the micrometer range, can be employed to perform the task of supercontiuum generation [101].

The design of the the micro-structures in a PCF allows tailoring the dispersion parameters that strongly influence the spectral broadening process. In particular, the ability to control the zero-dispersion wavelength λ_{ZD}, i.e., the wavelength at which the dispersion changes from normal ($\beta_2 > 0$) to anomalous ($\beta_2 < 0$) dispersion, is of great importance. This degree of freedom allows manufacturing of fibers that are pumped in the anomalous dispersion regime by common Ti:sapphire oscillators centered around 800 nm, which was found to be a prerequisite for strong spectral broadening. In this dispersion regime, stable pulse forms exist that do not spread in time due to the interplay of negative GVD and the counter-acting SPM, which are referred to as *solitons*. Husakou and Herrmann first developed a theoretical framework that correctly describes the observed spectra generated in PCFs by a process called *soliton fission* [102]. According to this work, the initial stage of spectral broadening is caused by symmetrical SPM associated with a temporal compression of the pulse, thereby forming a higher-order soliton. The influence of strong third-order dispersion at λ_{ZD}, however, makes these solitons unstable and leads to a successive split-off of fundamental solitons, which subsequently experience a Raman-induced frequency red-shift [103]. Moreover, the effect of higher-order dispersion on the split solitons gives rise to an energy transfer to narrow-band resonances in the normal dispersion regime, the positions of which can be determined from phase-matching considerations [104]. In the time domain these *dispersive waves* correspond to broad low-amplitude pedestals at the trailing edges of the soliton peaks.

In practice, the processes described above allow the generation of supercontinua that span over even more than one octave already at input pulse energies as low as 1 nJ [100]. Moreover, the generated spectra preserve the CEP information as all nonlinear conversion steps represent FWM processes, which makes CEP measurements of oscillator pulse trains possible.

Since the first demonstration of supercontinuum generation at the oscillator level very broadband Ti:sapphire oscillators have become available that provide more than 300 nm (FWHM) wide spectra. Because these laser sources need significantly

less additional broadening, SPM in highly nonlinear crystals can already be sufficient to obtain the necessary full octave wide spectrum [69]. In section 3.1.1 a special CEP detection setup will be presented, which makes use of such broadband laser sources.

2.5 CEP Stabilization

So far, the CEP slip of mode-locked oscillators has been considered as a constant parameter that is defined by the static dispersion in the laser cavity. This assumption, however, represents a strong idealization, as, in practice, every oscillator is exposed to the influence of the unsteady environmental conditions in the laboratory. Due to the large GPO of several hundred cycles for one cavity roundtrip, see section 2.3, tiny variations of the temperature or a changing humidity can strongly affect the CEP. Other possible noise sources are mechanical vibrations, pressure variations caused by acoustic noise or air flows, and fluctuations of pump laser parameters.

Although design improvements in recent years have led to significantly more stable mode-locked oscillators, an active CEP stabilization mechanism is still indispensable, as free-running lasers still exhibit f_{CE} jitters on short time-scales as well as slow long term drifts over minutes and hours. The different CEP stabilization approaches that are discussed in the following are generally divided into conventional feedback schemes and the recently developed feed-forward approach.

2.5.1 Feedback Stabilization

In principle, all the above-mentioned noise sources double as potential control parameters for a feedback stabilization scheme, as they all affect the intracavity dispersion. The most straightforward implementation of dispersion control is realized simply by changing the amount of dispersive material in the optical path, which is typically done with a pair of moveable glass wedges [105]. While this method allows for large phase shifts of several cycles, the inertia of the optical components strongly limits the control bandwidth, which applies to all stabilization schemes with mechanically moving parts. An exception to this rule is a method that introduces geometrical dispersion by tilting a cavity mirror in a prism-based oscillator. This approach was shown to support control bandwidths of up to 25 kHz [106] but is only applicable to this special type of oscillators that is not widely used anymore.

Certainly the most common feedback mechanism relies on the modulation of the oscillator pump power, which affects the CEP by the complex interplay of various processes. Apart from the thermal influence on the GPO [26], the CEP is changed by a combination of a power-dependent spectral shift and a non-vanishing GDD [11]. Another contribution to the GPO stems from the dispersion of the nonlinear phase shift that is predominantly acquired in the laser crystal [26, 90]. While the interplay of these processes and therefore the observed overall power dependence

strongly depends on the specific oscillator design and the exact conditions, it has been shown that the nonlinear dispersion effect $n_2(\omega)$ is the dominant contribution in modern dispersion-managed Ti:sapphire oscillators [107].

The key advantage of the nonlinear feedback mechanism is the intrinsically fast response time, which is, in principle, only limited by the laser dynamics that convert the pump power changes into intracavity peak power fluctuations. In practice, however, the achievable control bandwidth is mostly constrained by the servo electronics and the typically employed acousto-optical power modulation, which still enable control bandwidths on the order of 100 kHz [108]. The downside of this feedback mechanism is that the action on the CEP is accompanied by an amplitude modulation of the oscillator pulse train. Given that the B integral of most Ti:sapphire oscillators is on the order of 2π, the pump power induced phase shift is limited to some 100 mrad before the disturbance of the oscillator becomes too severe to sustain the mode-locked operation.

In fact, it is a characteristic feature of all feedback mechanisms, that side-effects on other laser parameters, such as repetition rate, output power or beam pointing, prevent a CEP stabilization without interrupting the performance of the free-running oscillator. In the next section 2.5.2, an extra-cavity feed-forward stabilization scheme will be presented that overcomes most of these limitations.

In order to ensure CEP stabilization via the feedback approach, first a suitable error signal has to be deduced from the measured in-loop beat signal. As the measurement and the stabilization of CEP noise at the DC baseband is prevented in RF-heterodyning schemes, the interferometrically detected beat signal V_{f-2f} is typically locked to another RF reference oscillator. To this end, the beat signal at f_{CE} is filtered and compared to the reference signal V_{ref} with a phase detector. In case of analog signal processing the phase comparison of two signals is accomplished by an electronic multiplication in a double-balanced mixer and subsequent low-pass filtering, see Fig. 2.7. Assuming the beat signal and the reference signal are given by pure sinusoidal oscillations

$$V_{f-2f} = \sin(\omega_{\mathrm{CE}} t + \varphi_{\mathrm{CE}} + \varphi_0) \tag{2.5.1}$$

$$V_{\mathrm{ref}} = \sin(\omega_{\mathrm{ref}} t + \varphi_{\mathrm{ref}}), \tag{2.5.2}$$

the multiplied signal will contain mixing products at $\omega_{\mathrm{CE}} + \omega_{\mathrm{ref}}$ and $\omega_{\mathrm{CE}} - \omega_{\mathrm{ref}}$. After low-pass filtering an error signal is yielded that reads

$$V_{\mathrm{err}} \propto \sin\left(\omega_{\mathrm{CE}} t + \varphi_{\mathrm{CE}} + \varphi_0 - \omega_{\mathrm{ref}} t - \varphi_{\mathrm{ref}}\right). \tag{2.5.3}$$

If the beat frequency approaches the reference frequency ($\omega_{\mathrm{CE}} \to \omega_{\mathrm{ref}}$), the error signal is reduced to a voltage that is proportional to the phase difference of the beat signal and the reference.

$$V_{\mathrm{err}} \propto \sin(\Delta\varphi) \approx \Delta\varphi \quad \text{for} \quad \Delta\varphi \ll \pi. \tag{2.5.4}$$

In the simplest case the control loop is closed by using this error signal directly to change the feedback parameter. This way, the phase difference is diminished until the error signal eventually shows just some residual jitter, which is referred to as a *phase-locked loop* (PLL), see Fig. 2.7. In practice, a PLL is equipped with an additional servo controller that further processes the error signal with an adjustable proportional, integral and differential element, in order to improve the stability and the performance of the lock. From the perspective of control theory, a stability criterion for a PLL is a transfer function with a positive phase margin, meaning that the phase difference between input and output signal is less than π at the frequency of unity loop gain [108]. Otherwise, phase errors experience amplification instead of damping and self-oscillations occur. A limiting factor of such analog PLLs is the occurrence of phase ambiguities if the phase errors exceed the interval $[-\pi/2, \pi/2]$. These ambiguities can produce cycle slips, or in the worst case force the PLL to unlock. To this end, either frequency division of the beat signal prior to the analog phase detection, or completely digital phase detection is often used to increase the phase ambiguity range [109]. While such measures render a PLL more robust against drop-outs, there is an intrinsic trade-off between the tolerance towards large phase errors and the achievable phase resolution that influences the residual phase jitter.

For many applications, e.g., for seeding a subsequent amplification stage, it is desirable to use a reference oscillator that is related to the laser repetition rate. A reference at the full repetition rate and integer multiples thereof creates the same issues as the stabilization at DC, namely the inability to distinguish the beat signal from the always present intermode beat and the ambiguity of positive and negative frequency excursions. Subharmonics of the repetition rate (f_{rep}/N) on the other hand are readily filtered and used as a reference, thereby creating pulse trains in which every Nth pulse yields the same field structure.

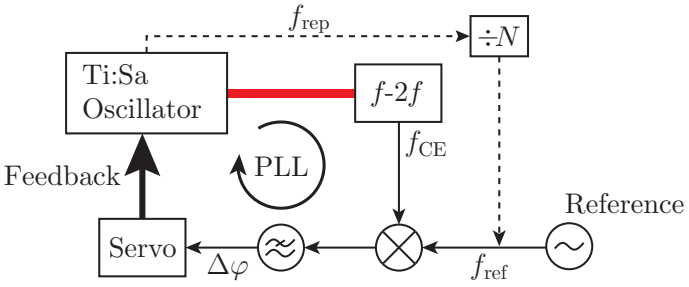

Figure 2.7: Phase-locked-loop (PLL) for locking the CEP drift to a reference oscillator. The phase error signal is derived by electronic mixing and subsequent lowpass filtering. This signal is further processed with a servo before it is fed back to the laser oscillator. Optionally a subharmonic of the repetition rate may be used as a reference signal (dashed lines).

2.5.2 Feed-Forward Stabilization

In 2010, Koke *et al.* introduced a conceptionally different feed-forward type CEP stabilization technique for oscillators, which no longer requires control of the intracavity dispersion [19]. Instead, the stabilization takes place in an external acousto-optical frequency shifter (AOFS), which eliminates many of the shortcomings of conventional feedback stabilization schemes.

The working principle of this acoustic device is presented in Fig. 2.8. A piezoelectric transducer is attached to a facet of an optically transparent crystal and is driven with a sinusoidal RF signal in the MHz range. The strain that is periodically exerted on the material propagates as an acoustic wave and is absorbed on the opposite facet to prevent the build-up of standing waves. As the acoustic wave locally changes the index of refraction through the photoelastic effect [110], a traveling index grating is formed that is described by:

$$n(\mathbf{r},t) = n_0 + \Delta n \sin\left(\omega_{\mathrm{ac}} t + \varphi_{\mathrm{ac}} - \mathbf{k}_{\mathrm{ac}}\mathbf{r}\right), \tag{2.5.5}$$

with Δn being the peak index change that depends on the applied RF power and on the photoelastic coefficient of the material. Further, ω_{ac}, φ_{ac} and $\mathbf{k}_{\mathrm{ac}}$ are the frequency, phase and wavevector of the acoustic wave. Light that is passing the index grating is deflected into various diffraction orders at angles of constructive interference. These angles fulfill the Bragg-condition known from solid-state physics

$$\alpha_{\mathrm{m}} = \arcsin\left(\frac{m\lambda_{\mathrm{opt}}}{2\lambda_{\mathrm{ac}}} - \sin\alpha_{\mathrm{in}}\right), \tag{2.5.6}$$

where the subscript m is referring to the diffraction order, α_{in} is the angle of incidence and λ_{opt}, λ_{ac} are the optical and acoustic wavelengths, respectively.

In order to gain maximum efficiency, the interaction in the AOFS is typically optimized to diffract the major part of the light into a single diffraction order by creating purely sinusoidal index gratings of several centimeter interaction length. In practice, diffraction efficiencies of 70-90% are possible, which, however, require the input of several watts of electrical power and make an active cooling system necessary.

An equivalent description to the diffraction formula (2.5.6) is given in k-space, when the wave vector of the acoustic wave is considered as a grating vector. For the geometry shown in Fig. 2.8, the k-vector addition of the optical waves and the acoustic wave reads as

$$\mathbf{k}_{\mathrm{out}} = \mathbf{k}_{\mathrm{in}} - \mathbf{k}_{\mathrm{ac}}, \tag{2.5.7}$$

where the negative sign accounts for reverse traveling direction of the acoustic wave. Apart from the relation in k-space, the interaction with the acoustical phonon has to conserve the energy in the spectral domain. It is this feature that provides the necessary leverage for CEP control as it gives rise to a spectral shift of the entire

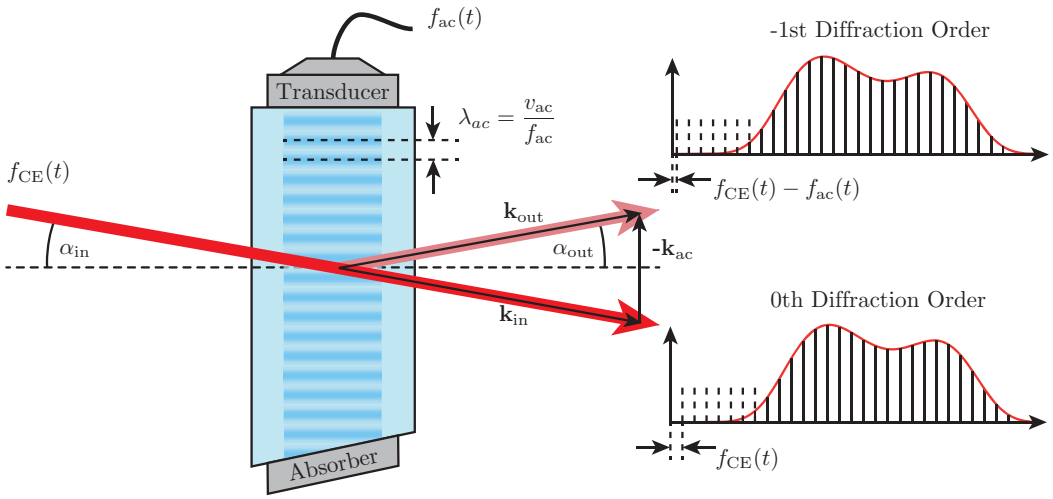

Figure 2.8: Frequency comb offset control with an acousto-optic frequency shifter (AOFS). Energy and momentum conservation are fulfilled for the interaction with an acoustical phonon of frequency f_{ac} and wavevector $\mathbf{k}_{ac}$ in the -1st diffraction order. The presented diffraction geometry ($\alpha_{in} = -\alpha_{out}$) is achieved if the angle of incidence is half the Bragg angle: $\alpha_{in} = \alpha_B/2 = 1/2\arcsin(\lambda_{opt}/2\lambda_{ac})$.

frequency comb. In the minus first diffraction order the down-shifted frequency comb is given by

$$\nu_m(t) = f_{CE}(t) - f_{ac}(t) + m f_{rep}. \tag{2.5.8}$$

A different way to explain the effect of the acoustic wave on the optical phase is based on the principle of the grating phase. By treating the diffraction of an optical grating in the Huygens picture, the interference of all secondary spherical waves shows, that the optical phase in a diffracted beam is directly linked to the phase of the grating, i.e., its lateral position. As can be seen in Fig. 2.9, a lateral grating phase shift of π will change the condition at a specific point from constructive to destructive interference and vice versa. Consequently, the optical phase of the diffracted beam is shifted accordingly, whereas the temporal envelope of the pulse is not affected. In the present situation, the phase of the induced index grating is changing continuously due to its propagation, which causes the previously described frequency shift by $\partial\varphi/\partial t = f_{ac}$.

For the purpose of CEP stabilization, f_{CE} is measured with a suitable nonlinear interferometer, preferably in the otherwise unused zero diffraction order, and is directly used as a driver signal for the AOFS [$f_{ac}(t) = f_{CE}(t)$]. This self-referenced CEP stabilization operation yields the particularly important case of a frequency comb with vanishing offset, which is inaccessible with standard feedback

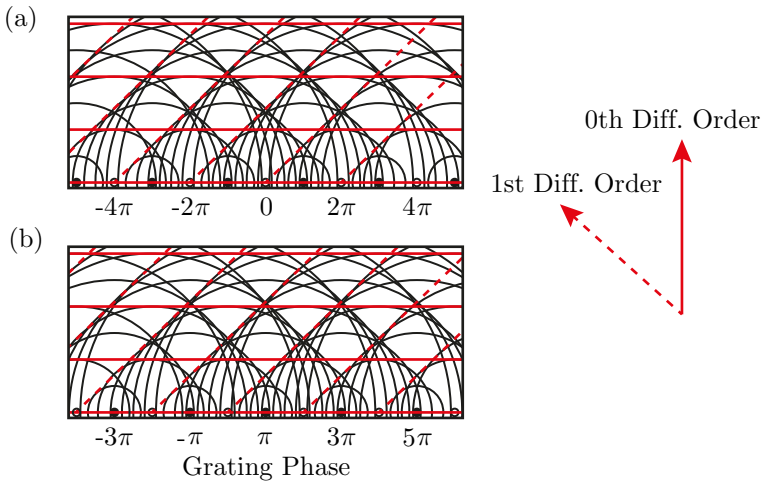

Figure 2.9: Emergence of the first diffraction order from a transmission grating in the Huygens picture. The different lateral positions of the grating in (a) and (b) demonstrate the dependence of the optical phase in the diffracted output on the grating phase.

stabilization schemes, except for the technically challenging direct locking scheme presented in [70].

Moreover, the measured beat signal is easily shifted with an additional local oscillator [$f_{\mathrm{ac}}(t) = f_{\mathrm{CE}}(t) - f_{\mathrm{loc}}$] before it is fed to the AOFS, which allows creating frequency combs with arbitrary offsets. The spectral representation then reads

$$\nu_m = -f_{\mathrm{loc}} + m f_{\mathrm{rep}}. \tag{2.5.9}$$

Next to the presented flexibility in the choice of the frequency comb offset, the feed-forward stabilization scheme has further distinctive advantages compared to the classical feedback schemes. First, the fact that no PLL is involved (that can lose the phase lock) renders the scheme intrinsically robust and lets it automatically regain stabilization after possible interruptions. Second, the absence of any back-action on the intracavity dispersion allows the free-running operation of the mode-locked oscillator without the influence on other laser parameters such as pump power or repetition rate. Finally, the achievable control bandwidth is on the order of 1 MHz, which is an order of magnitude improvement compared to optimized feedback schemes [108]. In fact, the total delay caused by electronic filters and especially the traveling time of the acoustic wave to the interaction zone can be limited to even less than a microsecond. Compared to the best feedback stabilization results [69], this fast response time gave rise to a more than two times improved stabilization performance, as it was demonstrated [19] by the record low residual phase jitter (root mean square) of 45 mrad.

Unfortunately, the feed-forward type stabilization with an AOFS is not free of side-effects on the laser parameters as well. The strong chirp that is acquired by the pulses while passing the dispersive material of the AOFS has to be compensated, if required for the subsequent application. In case of seeding an chirped pulse amplifier the compensation is not necessary, as the pulses need to be strongly chirped anyway. Otherwise, suitable pulse compression techniques have to be employed. Next to the temporal chirp, the diffracted beam also shows some angular dispersion, which is a consequence of the wavelength dependence of the Bragg-condition (2.5.6). This effect is compensated either by passing the AOFS a second time in the reverse direction, which requires the frequency division of the electric signal by two [111], or by placing a dispersive element (e.g. a glass wedge) behind the shifter that provides the same amount of negative angular dipsersion [75].

Apart from these static effects that are readily compensated, there are other severe effects that are related to a drifting AOFS driver frequency $f_{\mathrm{CE}}(t)$. In fact, an AOFS always acts as a beam deflector, since the diffraction angle is also dependent on the acoustic wavelength, see Eq. (2.5.6). This relation translates a drifting beat signal into beam-pointing instabilities, which is detrimental, e.g., for grating-based pulse stretchers that are used in some amplifier systems [112, 113]. Furthermore, a changing acoustic wavelength leads to a different grating phase at the interaction zone with the laser beam. As discussed before, this grating phase directly affects the optical phase, which gives rise to additional CEP noise.

The novel concepts that are presented in this thesis aim at the compensation of such remaining side-effects of the feed-forward approach, in order to bring CEP stabilization of oscillator and amplifier system to a new level with unprecedented low phase jitters.

Chapter 3

Absolute Limitations of Oscillator CEP Stabilization

In this chapter the most limiting constraints of Oscillator CEP stabilization are discussed, and respective measures to reduce their impact are presented.

In particular, the first section of this chapter treats the different noise sources that impede a flawless detection of the CEP. While section 3.1.1 deals with the less restrictive technical issues of CEP detection that are addressed by the interferometer design, section 3.1.2 covers the more fundamental limitation of shot noise that is a result of the particle nature of light. As will be shown below the only chance to lessen the latter restriction is an optimization of the light levels present in the detection front-end.

Finally, section 3.2 deals with limitations of the stabilization process that arise due to the inevitable time lag between the detection and the correction of the CEP. Besides a limited control bandwidth, this latency causes additional phase noise in a feed-forward type stabilization if the f_{CE} of the free-running oscillator is subject to drift. To this end, different stabilization concepts are presented that address these causality-imposed shortcomings.

3.1 Limitations of CEP Detection

The different noise sources that affect the CEP slip in an oscillator pulse train have been discussed in section 2.5. Theoretically, all of these correlated technical noise features can be removed, given that a sufficiently fast and flawless stabilization technique is at hand. In practice, however, such an ideal CEP stabilization performance is not within reach, as already the detection process is subject to external noise. If the measurement of the actual CEP slip in a pulse train is corrupted, a subsequent stabilization scheme will always suffer from residual CEP noise, as the phase errors of the measured beat signal are directly transferred to the stabilized

output. Unfortunately, such additional noise occurs to some extent in all of the different steps of CEP detection: Spectral broadening, nonlinear interferometry, and photo detection.

During the first of these steps, i.e., the generation of an octave-spanning spectrum, the amplitude noise of the seed pulses is amplified due to the highly nonlinear interaction, especially for the case of broadening in photonic crystal fibers [114–117]. Moreover, such amplitude fluctuations transfer into noise of the CEP (*amplitude-to-phase coupling*) due to the intensity dependent GPO, see also section 2.5.1.

On the one hand this input noise consists of technical noise, such as power fluctuations caused by instabilities of the laser itself or by variations of the coupling efficiency. On the other hand the input noise can be attributed to uncorrelated shot noise. While the former noise sources are in principle addressable by stabilization techniques, the latter represents a fundamental physical limitation that is solely determined by the available pulse energies.

It was determined in numerical studies by Washburn and Newbury [117] that the resulting noise figures strongly scale with the amount of spectral broadening, the length of the used fiber, and the initial chirp of the pulses. They concluded that it is optimal to seed a rather short PCF by high-energy pulses with vanishing initial chirp, in order to obtain the necessary amount of spectral broadening with the least possible phase noise.

In contrast to the broadening of common oscillators with microstructured fibers, modern ultra-broadband oscillators have the major advantage of needing only small additional broadening to obtain octave coverage, which can be achieved by SPM in bulk materials. The whole difficulty of power fluctuations due to beam pointing instabilities or vibrations is not present in bulk materials, which makes the broadening process less susceptible for seed noise and reduces the overall noise corruption in this step of CEP detection.

3.1.1 Interferometer Design

Next to the previously discussed process of spectral broadening, also the heterodyning of different harmonics of the fundamental frequency comb in a nonlinear interferometer is influenced by external noise. The optical components in such interferometers must be kept mechanically stable with better than wavelength accuracy in order to allow precise phase measurements. This requirement imposes severe challenges on the design of these setups. Even though nonlinear interferometers are often operated in a shielded environment, it is not possible to isolate the interferometers completely against all sorts of noise sources, such as air streaks, acoustic noise, mechanical vibrations, and thermal drifts. To this end, it is mandatory to employ an interferometer topology that is as insensitive as possible to said external noise sources.

Figure 3.1 shows an overview of various interferometer topologies that reportedly have been used for CEP detection. While in principle all the illustrated

interferometers can be used for both, f-$2f$ and 0-f interferometry, their features are treated exemplarily for the former technique. A very common interferometer topology is the Mach-Zehnder interferometer depicted in Fig. 3.1(a). In this setup the second harmonic is generated in a separate interferometer arm and is combined with the fundamental spectral components afterwards. The temporal overlap is thereby achieved via tuning the length of one interferometer arm with a delay stage. An issue of this topology is the limited potential for miniaturization, which results in a rather long unshared beam path of the f and the $2f$ components, making the interferometer very susceptible to noise stemming from relative phase jitters of the two separate arms.

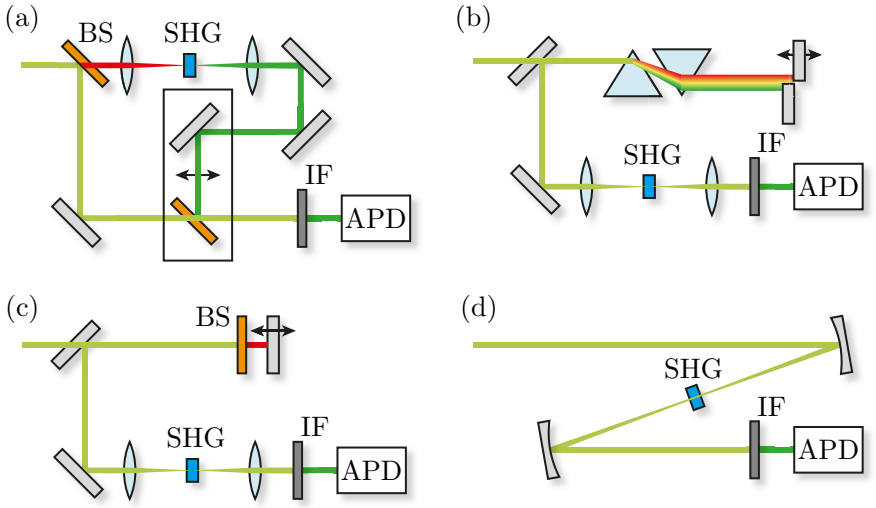

Figure 3.1: Different nonlinear interferometer topologies. (a) Mach-Zehnder interferometer (b) Prism-based quasi-common-path interferometer. (c) Dichroic quasi-common-path interferometer. (d) Monolithic interferometer. BS: dichroic beam splitter. IF: interference filter. APD: avalanche photo diode.

In principle, the issue of drifting interferometer arms can be avoided by using an entirely collinear interferometer, in which the f and $2f$ components have the same optical path. However, the compensation of the group delay that is introduced by the process of spectral broadening and by other optical components of the setup is usually difficult to achieve with a true common-path topology. One possibility to address this issue is to place a birefringent crystal in the beam path, which then introduces a relative delay to the orthogonally polarized f and $2f$ components [118]. Another solution is the use of so called quasi-common-path (QCP) interferometers, which include a geometrical group delay compensation while reducing the unshared beam path to the extent possible. A potential realization of such a QCP interferometer [19, 119] is depicted in Fig. 3.1(b), which utilizes a prism sequence to

separate the different spectral components and a pair of adjustable back reflecting mirrors to tune the temporal delay. Comparing the CEP stabilization performance of this interferometer design to a classical Mach-Zehnder interferometer yields a reduction of residual phase noise by 40% [119], clearly demonstrating the improved immunity of this setup against external noise.

Another realization of a QCP interferometer that is based on a dichroic beam-splitter, see Fig. 3.1(c), has been developed during the work for this thesis in collaboration with Sebastian Koke and was published in [120, 121]. In this rather simple interferometer design, the unshared beam path is further minimized to the small gap between a dichroic beam splitter, which reflects the short-wavelength part of the spectrum and a metallic mirror reflecting the long-wavelength spectral components. The spacing of the two mirrors is only on the order of a millimeter and is adjustable to tune the relative temporal delay. A further advantage of this setup compared to the prism-based approach is that no angular dispersion is introduced, which makes it less sensitive to CEP noise stemming from beam pointing instabilities. It is well known from the analysis of prism-based oscillators that such pointing fluctuations have a strong effect on the GPO and thus also on the CEP [26]. The comparison of the stabilization performances of the dichroic QCP interferometer and the prism-based approach yields again a vast reduction of residual phase noise, especially in the low frequency range (0.1 Hz-10 Hz), where the characteristic $1/f$ noise contribution was reduced fivefold [120]. A measurement based on this dichroic QCP interferometer is presented in section 3.2.1.

In terms of passive stability the dichroic interferometer is only surpassed by a completely monolithic interferometer as it is depicted in Fig. 3.1(d). This type of interferometer differs from all the previous designs, as it not only performs the frequency doubling or the DFG, but also provides the necessary spectral broadening by SPM in one and the same nonlinear crystal. Typically, quasi-phase-matched periodically poled lithium niobate (PPLN) crystals are used for this purpose, as they posses high conversion efficiencies and, moreover, they provide the opportunity to tune the conversion frequency to some extent via the crystal temperature. The truly collinear design that basically consists of the nonlinear crystal itself, renders the interferometer very robust against external noise and makes it nearly maintenance-free, as was demonstrated by the long-term measurements in [75]. On the downside, this design is only applicable to modern laser oscillators that already provide more than 300 nm broad spectra right from the cavity, so that the SPM in the PPLN crystal is sufficient to obtain the octave coverage. Moreover, the interferometer offers no opportunity to compensate the group delay of the different spectral components accumulated in the nonlinear crystal, which at least reduces the strength of the generated beat signal. Generally, the parameters of the nonlinear crystal (wavelength tuning, crystal length, material dispersion) have to be chosen very carefully, as there is almost no way to adjust the interferometer once it has been set up. Despite these obstacles, it has been demonstrated that such monolithic interferometers can provide rather strong beat signals with a signal-to-

noise ratio (S/N) of approximately 55 dB [69] in a 100 kHz resolution bandwidth (RBW). This result comes close to the best reported values that have been obtained with fiber-based spectral broadening [121], see also section 3.1.2. CEP stabilization results that were achieved with a monolithic $0\text{-}f$ interferometer will be presented in section 4.1.1.

3.1.2 Shot Noise Limitations in RF-Heterodyning

The final step of CEP detection is the electro-optic conversion of the beat signal in the detection front-end of the nonlinear interferometer, which is usually achieved with a sufficiently fast avalanche photodiode (APD) that preferably has a high quantum efficiency at the given detection wavelength. Depending on the strength of the illumination, the photo current provided by the APD is either dominated by optical shot noise or by noise that is stemming from the detector itself. The latter is observed under extreme low light conditions, where the signal is affected by noise of the leakage current, excess noise due to the avalanche process, and thermal Johnson-Nyquist noise in the electronics of the APD module. In total these effects result in a certain noise-equivalent power (NEP) that defines the ultimate white detection noise floor of the APD module. If, however, the illumination of the APD is increased, the noise of the photo current is also affected by optical shot noise, which is an unavoidable consequence of the particle nature of the incident light field [122–125]. From a statistical point of view, the emission and detection of photons is subject to pure Poissonian statistics, meaning that the occurrence of such events is completely uncorrelated, which is true unless non-classical light is considered [126, 127]. A random variable is called Poisson-distributed if its probability mass function is given by

$$p(k) = \frac{\lambda^k e^{-\lambda}}{k!}, \quad \lambda > 0, \quad k \in \mathbb{N}, \tag{3.1.1}$$

where the expected value of the random variable as well as its variance are equal to λ. Consequently, if the number of photons that are emitted by a light source in certain amount of time is $\langle N \rangle$ on average, the photon number standard deviation is $\sqrt{\langle N \rangle}$, showing that the impact of shot noise is decreasing with increasing light fluence. As a result, shot noise is often overruled by other technical noise sources when dealing with strong light sources that deliver milliwatt powers or above. However, when very weak optical signals are detected, shot noise has to be taken into account.

At first sight, it appears puzzling that shot noise may be a limiting constraint for heterodyne detection of the CEP slip at all, as typical oscillators provide on the order of a few 100 mW average power and pulse energies in the nanojoule range. While these energy levels correspond to photon numbers on the order of 10^{10} per pulse, thus enabling the precise determination of the energy level of individual laser pulses within a 10^{-5} noise margin, only a minor fraction of the total pulse energy

finally reaches the detection front-end of the nonlinear interferometer. First, the process of spectral broadening readily costs three orders of magnitude in terms of photon numbers, as the spectral densities in the wings of the supercontinuum are typically some 10 dB lower than the peak power density. Second, only a small wavelength interval at the spectral edge is then converted by either SHG or DFG, which is furthermore very inefficient at these low light levels. Even when using quasi-phase matched crystals the conversion efficiency is only on the order of 0.1 to 1%, realistically bringing the number of photons that contribute to the amplitude modulation down to 10^4, which eventually allows for a S/N of a mere 100.

These numbers clearly indicate the important role of shot noise in the detection of the CEP, which are systematically investigated in the following. Numerical simulations are presented to quantify the light level dependence of the shot noise induced phase jitter as well as the impact of detector noise. Moreover, a connection between the corruption by such white noise sources and the stability of a classical feedback loop is established. In order to address the limitation of shot noise, a numerical study for the optimization of the supercontinuum generation process is presented, which led to substantially improved S/N of the experimentally determined beat signals.

Numerical simulations of shot noise effects

For the investigation of shot noise effects a series of numerical simulations has been conducted in which a train of pulses with an average photon number $\langle N \rangle$ is synthesized, as it is detected in the front-end of an f-$2f$ interferometer. This type of interferometer is considered here without any loss of generality, and the findings are readily expanded to all methods relying on the optical interference of different harmonics. The generated pulse train is sampled at the repetition rate of the oscillator f_{rep}, so that each element of the time series $N(k)$, $k \in \mathbb{N}$ represents the photon number of one individual laser pulse. To account for the beating of the different harmonics an amplitude modulation is encoded on the time series according to

$$N(k) = \left| \sqrt{\langle N_f \rangle} + \sqrt{\langle N_{2f} \rangle} \exp(i\varphi(k)) \right|, \tag{3.1.2}$$

where $\langle N_f \rangle$ and $\langle N_{2f} \rangle$ are the average photon numbers in the heterodyned spectral regions and the phase is $\varphi(k) = 2\pi k f_{\mathrm{CE}}/f_{\mathrm{rep}}$. Next, Poissonian noise with an rms spread of $\sqrt{N(k)}$ is added to the time series to account for the shot noise, giving rise to a white detection noise floor in the RF power spectrum.

The repetition rate was set to 100 MHz in the simulations in order to match the situation of a typical Ti:sapphire oscillator. Scaling to other repetition rates is straightforward in the numerical simulations, albeit in practice it becomes increasingly challenging to achieve a reasonable S/N at higher repetition rates, simply due to the lower pulse energies. The actual value of the beat frequency does not affect

the resulting noise levels and was arbitrarily set to 2 MHz. In the first set of simulations, the length of the time series was fixed at $L = 1000$, which corresponds to a 100 kHz resolution bandwidth (RBW) of the RF power spectrum. For the reason of comparability, all given RF power S/N in this thesis, including experimentally dertermined values, refer to a 100 kHz RBW, even if later simulations are based on longer time series of one million data points.

In order to investigate the influence of the photon numbers, the noisy pulse trains, as well as the corresponding RF power spectra are plotted in Fig. 3.2 for two different total average photon numbers $\langle N \rangle = \langle N_f \rangle + \langle N_{2f} \rangle$. In both cases the average photon numbers of the f and $2f$ components are assumed to be ideally balanced

$$\langle N_f \rangle = \langle N_{2f} \rangle = \langle N \rangle /2, \tag{3.1.3}$$

which results in a 100% modulation depth of the pulse train and corresponds to a beat signal at 6 dB below the level of the intermode beat. At very low light levels of only 10 photons per pulse, see Fig. 3.2(a) and (c), the pulse train makes a rather noisy appearance, even though the visibility of the beat signal is already equivalent to a S/N of 37 dB. For a hundred times higher photon number $\langle N \rangle = 1000$, see Fig. 3.2(b) and (d), the pulse train becomes quite smooth, and the reduction of the noise floor enhances the visibility to 57 dB.

The determination of the beat visibility has been repeated systematically for various average photon numbers and the results are depicted as the red triangles in Fig. 3.3. It should be emphasized that the S/N of the RF power, which is linearly scaling with $\langle N \rangle$, is not to be confused with the optical S/N that is only scaling with the square root of $\langle N \rangle$. Apart from the ideally balanced situation, the S/N was also analyzed for the case that either the f or the $2f$ components become ten times larger (green circles) or even a hundred times larger (black squares) than the others. Given that the total number of photons is kept constant, the S/N is the lower the more asymmetric the distribution of photons among the f and $2f$ components becomes, as it is indicated by the vertical shift for the different cases in Fig. 3.3. From this one might conclude that a symmetric distribution always leads to the highest S/N possible. However, this conclusion is only correct if there is a fixed number of photons shared between the f and $2f$ components, which is typically not the case for broadening via SPM or soliton fission. If the photodetection is assumed to have a perfect quantum efficiency and is not corrupted by additional noise from the detector, the S/N reads

$$\mathrm{S/N}(@100\,\mathrm{kHz\ RBW}) = \frac{2\,\langle N_f \rangle\,\langle N_{2f} \rangle}{\langle N_f \rangle + \langle N_{2f} \rangle} \cdot 1000, \tag{3.1.4}$$

where $2\,\langle N_f \rangle\,\langle N_{2f} \rangle$ is the mean square of the beat signal and $\langle N_f \rangle + \langle N_{2f} \rangle$ is the variance of the corresponding Poissonian noise. The additional factor accounts for the integration over one thousand laser pulses at the resolution bandwidth of

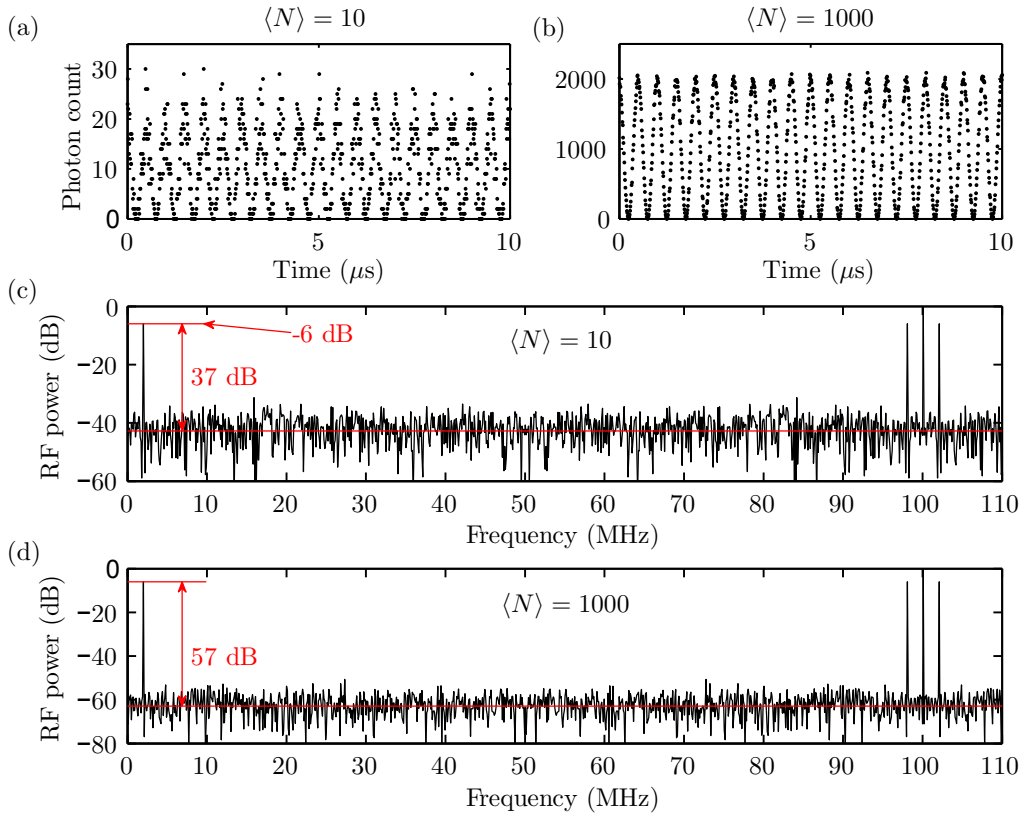

Figure 3.2: (a,b) Time series of the photon numbers of a f_{rep} =100 MHz pulse train amplitude modulated at f_{CE} =2 MHz for different average photon numbers: $\langle N\rangle = 10$, $\langle N\rangle = 1000$. (c,d) Corresponding RF power spectra as displayed by a spectrum analyzer at 100 kHz RBW with S/N indicated in red.

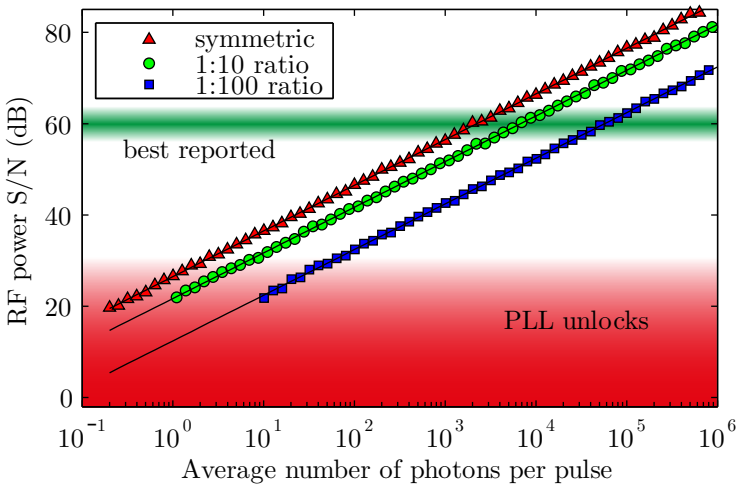

Figure 3.3: RF power S/N of the beat signal for pure Poissonian noise at 100 kHz RBW vs. total average number of photons per pulse for balanced f and $2f$ spectral components (red triangles) as well as for asymmetric cases (green circles, blue squares).

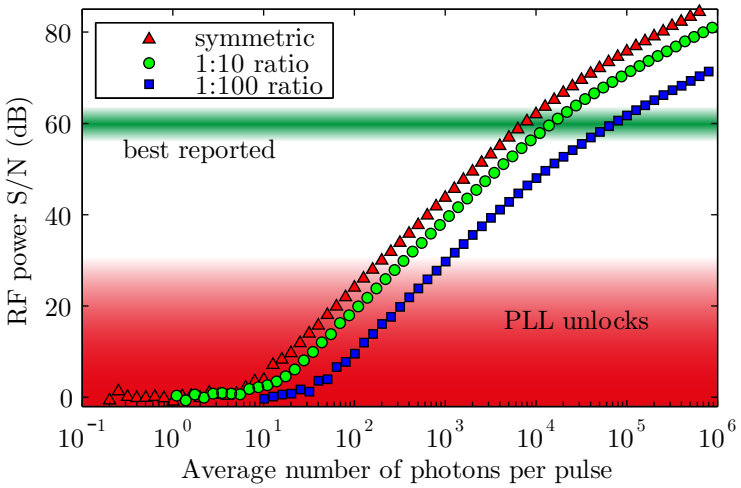

Figure 3.4: RF power S/N of the beat signal for Poissonian noise plus white APD detector noise of 134 photons per pulse vs. total average number of photons per pulse for balanced f and $2f$ spectral components (red triangles) as well as for asymmetric cases (green circles, blue squares).

100 kHz, which increases the acquired number of photons accordingly. In case the supercontinuum generation process allows the optimization of the f and $2f$ components independently from each other, one finds that an asymmetric situation can yield a higher S/N than a symmetric situation where both components are at the same low light level. However, since this improvement is limited to a factor of two, even for an arbitrary high ratio of $\langle N_f \rangle$ and $\langle N_{2f} \rangle$, it is often more effective to optimize the level of the weaker signal. In fact, the bottleneck in most setups is the level of the frequency doubled components, as it suffers from the low efficiency of both, spectral broadening and SHG, typically leading to orders of magnitude weaker light levels than for the fundamental spectral components.

While so far the dependence of the S/N on the light level has been calculated exclusively for pure Poissonian noise, a more realistic calculation has to incorporate the limiting detection noise floor of the photo diode. Ready-to-use APD modules that are optimized for short wavelength detection with a bandwidth on the order of 100 MHz typically possess a noise equivalent power of about $0.5\,\mathrm{pW}/\sqrt{\mathrm{Hz}}$ [1]. This value defines the optical power level of a signal that yields a S/N= 1 for a measurement time of half a second. By adapting the detection bandwidth to the situation in the simulations (100 MHz), the reduction of the measurement time by a factor 10^8 increases the detectable power level to 5 nW. Assuming the practically relevant detection wavelength (532 nm), the power level of the detection noise already corresponds to a photon number standard deviation of $\sigma_{\mathrm{Det}} = 134$ photons per pulse. To this end, the calculation of the S/N according to Eq. (3.1.4) has to be expanded by the respective noise term in the denominator:

$$\mathrm{S/N}(@100\,\mathrm{kHz\ RBW}) = \frac{2\,\langle N_f \rangle\,\langle N_{2f} \rangle}{\langle N_f \rangle + \langle N_{2f} \rangle + \sigma_{\mathrm{Det}}^2} \cdot 1000. \tag{3.1.5}$$

In the numerical calculations the additional detector noise was taken into account by adding white Gaussian noise with the same spread as specified above. The systematic determination of the resulting S/N has been repeated in the same fashion as before and the results are shown in Fig. 3.4. This more realistic dependence of the S/N on the photon number can be divided into three different regimes. First, at very high photon numbers of 10^5 and above, the comparison to Fig. 3.3 reveals almost no deviation, which is explained by the strong domination of shot noise effects over detector noise. Second, at very low light levels of less than 10 photons per pulse, the detection noise is prevailing so that no beat signal is resolvable at all. Third, in the intermediate regime both noise sources have to be considered and the scaling of the S/N is proportional to N^2. Even the best reported S/N [69, 121], which are indicated by the green zone in Fig. 3.4, fall into the range where the detector noise cannot be completely neglected.

With the ability to determine the best achievable S/N from the number of photons present in the interferometer detection front-end, the next step is to calculate

[1] Noise equivalent power determined from the specifications of the used Hamamatsu APD module C5331-11.

the phase jitter that is induced by the respective white noise floor, in order to give an estimate about what kind of stabilization performance can be achieved at a given beat note visibility. One possibility to quantify this functional dependence is to demodulate the phase from the noisy pulse train by the Fourier transform-based Takeda algorithm [128] and compare it to the reference phase from a noise-free pulse train. This procedure is very useful when the rms phase jitter is rather small ($\delta\varphi \ll \pi$), but runs into difficulties when the phase jitter becomes as large as a few hundred milliradians. The reason for this issue is that the algorithm fails to distinguish between real phase errors and discontinuities that stem from the phase ambiguities on the interval $[-\pi;\pi]$. Therefore a different phase detection approach was used that is based on the multiplication of the noisy beat signal with a reference signal in the time domain according to the trigonometric identity

$$\sin(\varphi_1)\cos(\varphi_2) - \sin(\varphi_2)\cos(\varphi_1) = \sin(\varphi_1 - \varphi_2). \tag{3.1.6}$$

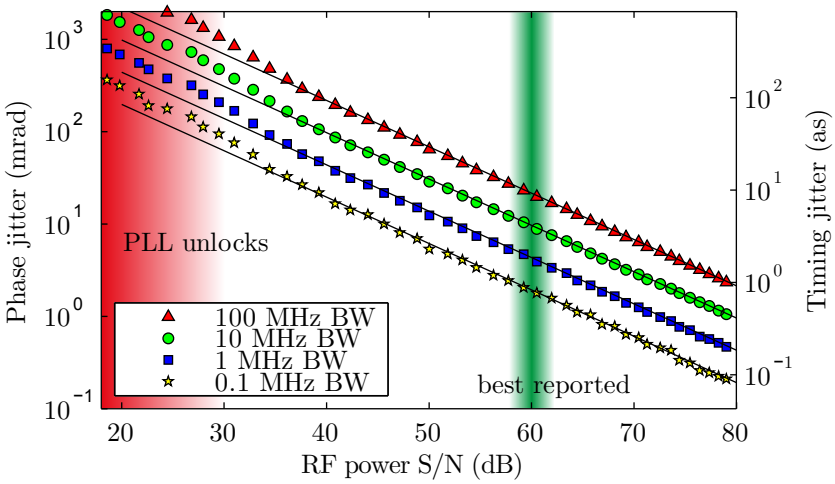

Figure 3.5: Simulated functional dependence of the rms phase jitter that is induced by shot noise and detector noise on the S/N of the beat signal for different detection bandwidths. The scale on the right ordinate yields the respective timing jitter for an optical cycle of 2.7 fs.

Taking the inverse sine of the mixing result then yields the shot-to-shot phase errors of the time series. This procedure was repeated for the same average photon numbers as it was done in Fig. 3.4 for the balanced situation. The full rms phase jitters deduced from these time series are plotted vs. the respective S/N ratios, indicated by the red triangles in Fig. 3.5. One finds that these data points mainly follow a straight line with the slope $-1/2$ on the double-logarithmic plot, revealing

that a tenfold decreased detection noise induced phase jitter corresponds to a 20 dB improvement in beat note visibility. This finding is explained by the fact that the noise floor in the RF power spectrum, determined by the S/N, scales in the same fashion as the noise floor in the power spectral density (PSD) of the phase noise σ_φ^2 (rad^2/Hz). The plotted rms phase jitter is then given by the square root of the integrated PSD

$$\delta\varphi(f_{\mathrm{low}}, f_{\mathrm{high}}) = \sqrt{\int_{f_{\mathrm{low}}}^{f_{\mathrm{high}}} \sigma_\varphi^2(f)\ \mathrm{d}f}, \tag{3.1.7}$$

where the value of the phase jitter obviously depends on the integration limits. For this reason, one has to be careful when comparing the residual phase jitters of different stabilization setups that were sampled at different bandwidths. Figure 3.5 illustrates the phase jitter dependence for various bandwidths down to 100 kHz, indicated by the colored data sets. One optical cycle at a center wavelength of 800 nm has a duration of 2.7 fs, which allows the conversion of the calculated phase jitters into relative timing jitters of the carrier and the envelope, as indicated by the right ordinate in Fig. 3.5. It is found that an enormous beat visibility of more than 80 dB is necessary to achieve a shot-to-shot timing jitter in the sub-attosecond regime.

Alternatively to the presented simulations, the coupling of amplitude noise to the phase jitter can be deduced analytically from a phasor diagram, as shown in Fig. 3.6. In this treatment the amplitude modulation of the pulse train is considered to be the projection of the two-dimensional circular motion onto the y-axis. According to trigonometrical considerations, an infinitesimally small amplitude deviation from the reference signal dy gives rise to an error in the phase retrieval

$$\mathrm{d}\varphi = \mathrm{atan}\left(\frac{\mathrm{d}y\cos\varphi}{\hat{y}}\right) \approx \frac{\mathrm{d}y}{\hat{y}}\cos\varphi, \tag{3.1.8}$$

which depends on the current phase φ and the modulation amplitude $\hat{y}$. The approximation in Eq. (3.1.8) is only valid for optical signal-to-noise ratios $\hat{y}/\mathrm{d}y$ that are much greater than one. In order to calculate the resulting rms phase jitter, one has to extract the square root of the squared phase error $(\mathrm{d}\varphi)^2$ that is averaged over all possible phase values:

$$\delta\varphi = \sqrt{\frac{1}{2\pi}\int_0^{2\pi} (\mathrm{d}\varphi)^2\ \mathrm{d}\varphi} \tag{3.1.9}$$

$$\approx \sqrt{\frac{(\mathrm{d}y)^2}{2\pi\hat{y}^2}\int_0^{2\pi} \cos^2\varphi\ \mathrm{d}\varphi} \tag{3.1.10}$$

$$= \sqrt{\frac{1}{2}\frac{(\mathrm{d}y)^2}{\hat{y}^2}}. \tag{3.1.11}$$

Considering the S/N of the RF power instead of the optical S/N one yields the same scaling behavior ($\propto 1/\sqrt{\mathrm{S/N}}$) that was found in the numerical calculations.

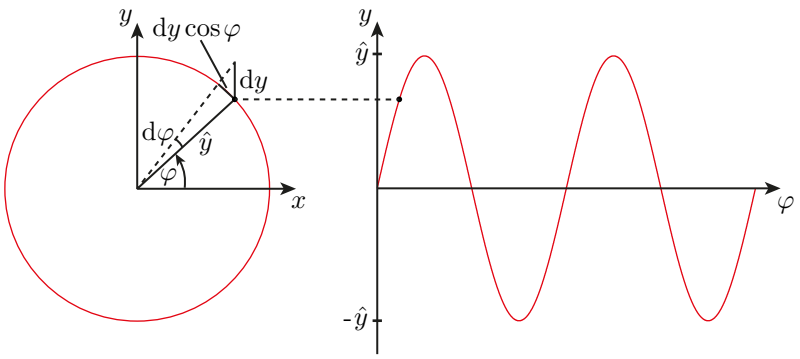

Figure 3.6: Amplitude-to-phase coupling in a phasor diagram.

For rather low S/N of 30 dB and less, however, the phase jitter dependence starts to deviate from the linear slope on the logarithmic scale in Fig. 3.5 when the shot-to-shot phase errors are no longer small compared to π. While at higher S/N the mixing product in Eq. (3.1.6) is directly proportional to the phase error itself, the approximation $\sin(\Delta\varphi) \approx \Delta\varphi$ starts to fail when the shot-to-shot phase errors approach a few hundred milliradian, explaining the deviation observed at lower S/N.

Interestingly, in experiments at similar S/N of 30 dB or less, the beat signal is reportedly found to be too weak to establish a stable feedback loop. It is therefore advisable to investigate the impact of the white noise from the electro-optic conversion on the stability of a PLL. Based on the previous simulations, the mean time that such a PLL can be preserved before it unlocks is determined in its functional dependence on the beat visibility. This allows the estimation of the minimum signal level that is required to get a reasonably stable lock in the absence of any other technical noise.

The calculations are based on the assumptions that all-analog locking electronics with a phase ambiguity range of $[-\pi/2; \pi/2]$ are used and that the lock is likely to be lost if the phase error exceeds this phase interval within a given locking bandwidth. It has been confirmed that the phase errors always follow Gaussian statistics when the bandwidth is reduced to the bandwidth of an optimized feedback loop $f_{\mathrm{loop}} = 100\,\mathrm{kHz}$ [108]. Fig. 3.7 exemplarily depicts the histogram plot of the numerically determined phase jitter sampled at f_{loop} for a S/N as low as 20 dB. The standard deviation $\sigma = \delta\varphi(f_{\mathrm{low}}, f_{\mathrm{loop}})$ of the Gaussian fit is then used to compute the probability for an event outside of $[-\pi/2; \pi/2]$, which causes the feedback loop to unlock. This probability is calculated from the complement of the respective cumulative Gaussian distribution. Multiplication of the probability for such events

with the time of one loop cycle ($1/f_{\mathrm{loop}}$) yields the mean locking time

$$\langle t_{\mathrm{lock}} \rangle = \mathrm{erfc}\left(\frac{\pi/2}{\sqrt{2\sigma^2}}\right)/f_{\mathrm{loop}}, \tag{3.1.12}$$

where $\mathrm{erfc}(x) = 1 - \mathrm{erf}(x)$ is the complementary error function of the normal distribution. In combination with the previous results Eq. (3.1.12) enables the plot of the mean locking time as a function of the the beat visibility, see Fig. 3.8. Under the given assumptions it is found that already a rather small S/N of 23 dB is sufficient to achieve locking times of several hours. This beat visibility corresponds to an rms phase jitter of 250 mrad. Owing to the steepness of the curve in Fig. 3.8, only a mere 50 mrad additional phase noise brings the mean locking time down to one minute. Eventually, for a visibility of less than 19 dB and 400 mrad rms phase jitter, phase locking becomes practically impossible, as the mean locking time is already less than a second. In summary these results indicate that the impact of shot noise and detector noise alone give rise to a threshold S/N of 23 dB that has to be surpassed in order to establish a stable PLL.

It has to be emphasized again that these results were derived in the absence of any correlated technical noise, which can explain the discrepancy to the experimental observation, that a stable lock requires a beat note visibility close to 30 dB. For a more precise estimate of a PLL's mean locking time one has to incorporate all potential other noise sources that influence the CEP, such as seed noise from the mode-locked oscillator, as well as the noise acquired during the different stages of CEP detection, which have been discussed above.

Optimization of the supercontinuum generation process

The only viable way to lessen the previously discussed restrictions of CEP detection is to increase the light levels in the interferometer detection front-end. The minimization of optical losses in the interferometer bears only a limited potential for such improvements, and also the efficiency of the frequency doubling is already mostly optimized by the use of quasi-phase matching techniques, see section 3.1.1. Certainly the most effective measure to improve the photon numbers of the f and $2f$ spectral components is an optimization of the supercontinuum generation process in the PCF. In practice, one finds that already small changes of the input peak power, caused, e.g., by variations of the coupling efficiency, strongly influence the spectral distribution of the supercontinuum. Apart from this, the observed amount of spectral broadening also depends on the length of the used fiber.

To this end, a numerical study of the soliton fission-based broadening process inside the micro-structured fiber was performed to find the conditions under which the spectrum is optimally distributed so that the highest possible S/N is achieved. To match the conditions of the experiments presented in this thesis, the dispersion profile and the geometrical properties of the employed commercial PCF (NL-PM-750, NKT photonics) were taken into account for the numerical simulations.

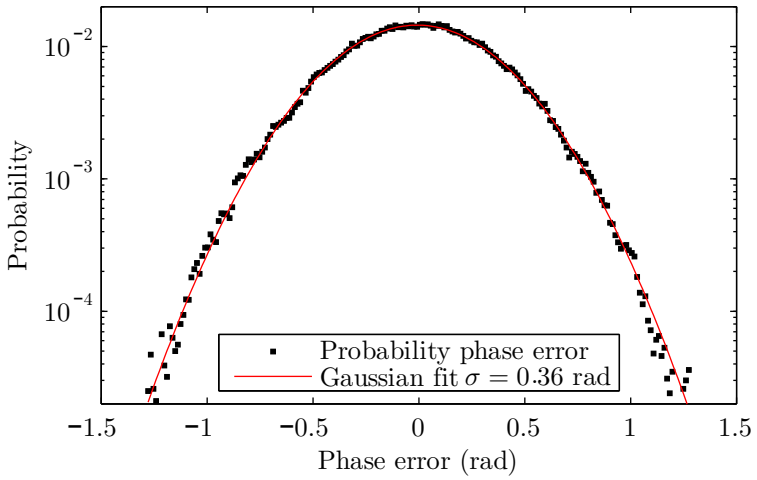

Figure 3.7: Histogram plot of the numerically determined phase error at a bandwidth of 100 kHz and a Gaussian fit with a standard deviation of $\sigma = 0.36$ rad.

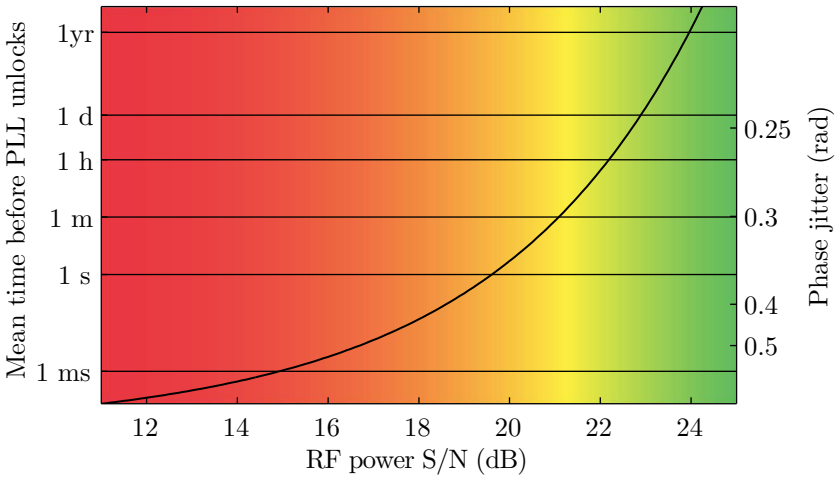

Figure 3.8: Mean time before an analog PLL unlocks as a function of the beat note visibility at 100 kHz RBW and a loop bandwidth $f_{\text{loop}} = 100$ kHz.

This polarization maintaining fiber combines a very small effective mode area of only $2\,\mu\mathrm{m}^2$ and a zero dispersion wavelength of 750 nm. The input center wavelength and the initial pulse duration were set to 770 nm and 15 fs, respectively. Computation of the spectra was performed in dependence on the propagation distance for different input powers according to the numeric model described in [129]. In cooperation with the group of Joachim Herrmann, these simulations were conducted by Anton Husakou and have been published together with the following experimental results in [121].

The simulated evolution of the spectral distribution under propagation in the PCF is shown in Fig. 3.9(a) for an input peak power of 22.8 kW (3 nJ pulse energy), where the spectral density is encoded in the logarithmic color scale. The horizontal black lines represent the spectral positions (530 nm and 1060 nm) heterodyned in the f-$2f$ interferometer, which are mainly predefined by the used PPLN crystal. In the anomalous dispersion regime close to the lower black line at 1060 nm one can observe the successive split-off of fundamental solitons and their subsequent redshift as it was discussed in section 2.4.3. Moreover, the build-up of dispersive waves in the normal dispersion regime is reproduced, which gives rise to strong spectral content close to the upper black line at 530 nm. Based on the computed spectral map it is now possible to calculate a figure of merit (FOM) for the achievable S/N in dependence of the propagation distance from the spectral power densities at the relevant spectral positions (E_{530}, E_{1060}). The definition of the FOM basically follows the same scaling as the S/N in Eq. (3.1.4), but has to account for the SHG efficiency of the PPLN crystal

$$\mathrm{FOM} = \frac{E_{\mathrm{SHG}} E_{530}}{E_{\mathrm{SHG}} + E_{530}}, \tag{3.1.13}$$

where $E_{\mathrm{SHG}} = d_{\mathrm{eff}} E_{1060}^2$ is the spectral power density of the frequency doubled light. Here the efficiency d_{eff} is determined according to a PPLN conversion efficiency of 2%/mm/W for a converted wavelength interval of 1.5 nm FWHM. The FOM deduced from the spectral map is plotted as a function of the propagation distance in Fig. 3.9(b), revealing that the optimal fiber length at this input peak power is $\approx$ 6 mm, which is by far shorter than the 10-20 cm long fibers usually employed [19]. The additional local maxima of the FOM can be attributed to the propagation distances at which the split-off fundamental solitons cross or come close to the lower black line at 1060 nm. Such maxima are most likely the reason why f-$2f$ interferometry can also produce reasonable S/N with fibers that are even longer than the 6 cm considered in the simulations. Nevertheless, the highest possible S/N is solely reached with very short fibers, which is even more pronounced at higher input peak powers, as shown by the trend in Fig. 3.9(c). Vice versa, one can infer that the shorter the fiber is, the more light has to be coupled into it in order to get the optimal spectrum. After all, a shorter fiber can thus lead to a higher number of photons in the relevant spectral regions. In conclusion, the somewhat counterintuitive outcome is that an actual reduction of the effective nonlinearity gives

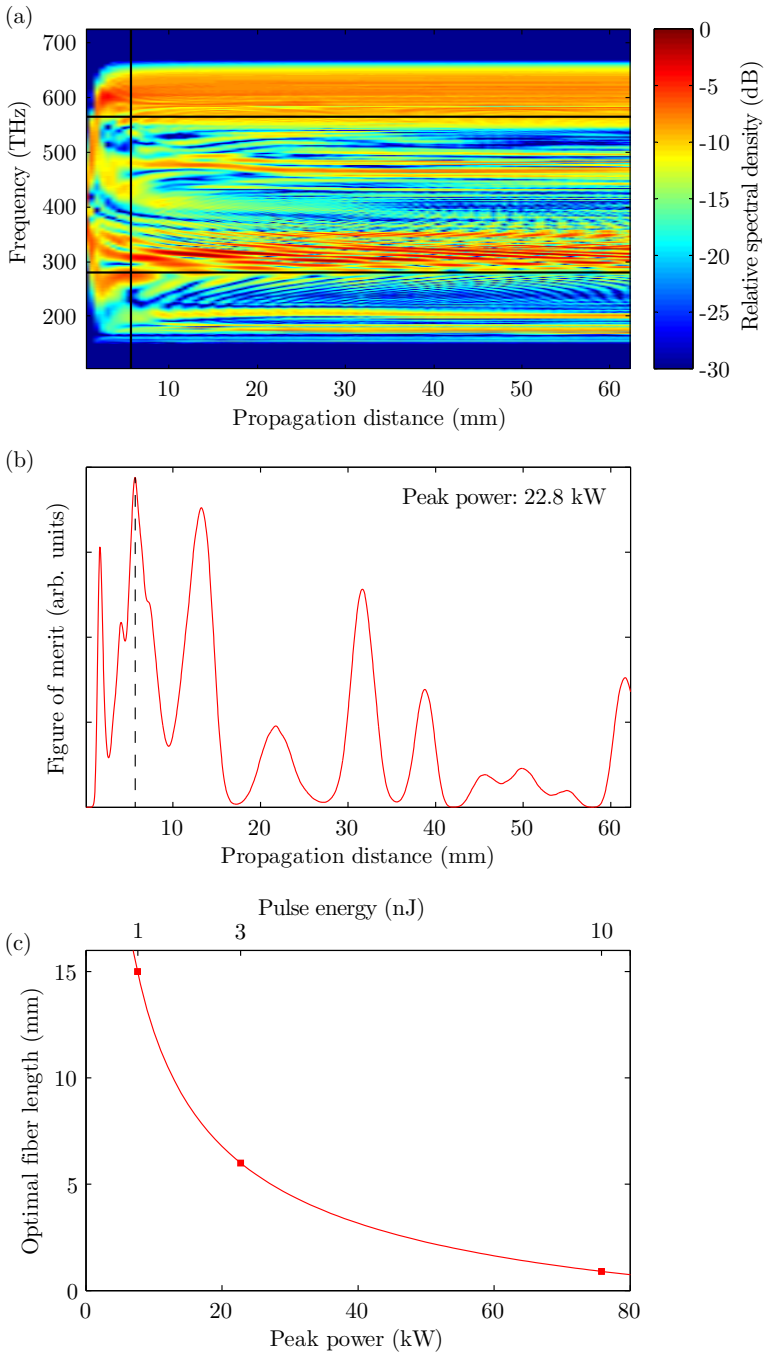

Figure 3.9: (a) Spectral distribution in the frequency domain as a function of the propagation distance. Spectral power density encoded in false colors. (b) Dependence of the figure of merit for an optimal S/N on the propagation distance for a 15 fs input pulse at 770 nm. (c) Peak power dependence of the optimal propagation distance.

rise to an improved signal quality if at the same time the power level is increased accordingly.

However, in practice there is a lower limit for the fiber length down to which the preparation of such micro-structured fibers is still feasible. Given that the preparation involves multiple steps, such as cutting the fiber, collapsing the microscopically small holes with a fusion splicer, gluing the fiber into a capillary and polishing both facets, the practical limit was found to be a length of approximately 10 mm. For the experiments presented in [121] such a short fiber was prepared, and the resulting supercontinuum greatly improved the S/N of the beat signal by 20 dB compared to the measurements in [19], where a fiber of 20 cm length was used. The measured in-loop and out-of-loop beat signals achieved with the 10 mm fiber are illustrated in Fig. 3.10, showing a S/N of 60 dB and 53 dB, respectively. These results, in all conscience, mark the highest visibility of a CEP beat signal that has been reported so far.

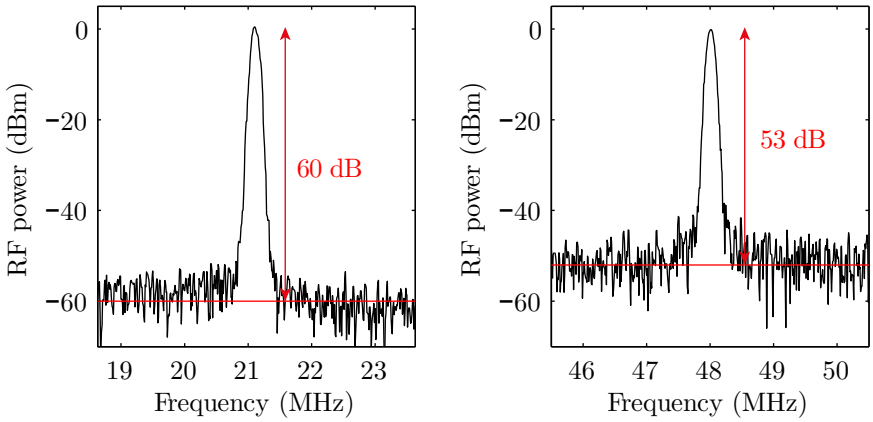

Figure 3.10: In-loop and out-of-loop beat signals generated with a dichroic QCP interferometer and measured with a RF spectrum analyzer at 100 kHz RBW.

While this achievement already denotes an enormous improvement of the ability to detect CEP noise, a closer inspection of the spectral distribution in Fig. 3.9(a) reveals the potential for further optimizations to even higher light levels. Shifting the f and $2f$ components to higher optical frequencies can yield an even better S/N, given that the major part of the spectral content is located at slightly shorter wavelengths than the used 530 nm and 1060 nm. To make use of this finding, a short wavelength-optimized PPLN crystal or a different material, such as periodically poled potassium titanyl phosphate (PPKTP), are promising alternatives under the given spectral conditions.

3.2 Limitations of CEP Stabilization Schemes

Apart from the restrictions of the CEP detection process that have been treated in the previous section, the eventual CEP stabilization performance is limited by the applied control mechanism as well. Fig. 3.11 provides a comparison of the two different types of stabilization schemes that have been used so far to control the CEP slip in an oscillator pulse train. On the one hand, there is the conventional feedback stabilization, which controls the CEP slip by changing the intracavity dispersion, e.g., via a power dependent nonlinear phase shift. This way a stable PLL can be established, locking the CEP slip to a certain RF reference oscillator. On the other hand, one can use the recently introduced feed-forward type stabilization scheme, which controls the CEP independently from the oscillator with an external acousto-optic frequency shifter. While the latter technique has some distinct advantages, such as the ability to directly produce frequency combs with vanishing offset mostly without crosstalk to other laser parameters, both of the presented control mechanisms suffer from a limited control bandwidth. This bandwidth is simply defined by the time lag between the measurement of the error signal in the in-loop interferometer and the instant of time at which the correction takes place. In case of a feedback stabilization this time lag is usually substantially higher than for the feed-forward type stabilization, due to the additional delay from the locking electronics and the necessary time it takes to change the intracavity dispersion. Optimized locking electronics combined with acousto-optic power modulation, as shown in Fig. 3.11(a), allow for feedback control bandwidths of 100 kHz [108], whereas the control bandwidth of the feed-forward type stabilization can be an order of magnitude higher [19].

In principle, a control mechanism with a bandwidth of 1 MHz is sufficient to compensate for all technical noise sources present in the CEP of a Ti:sapphire oscillator pulse train, since the fastest technical noise contributions transferred to the CEP are limited by the lifetime of the upper laser level. This is the reason why one solely observes white phase noise above several hundred kilohertz for Ti:sapphire oscillators [108]. Fiber lasers, on the other hand, typically exhibit much stronger CEP noise that shows up as very broadband free-running beat signals on a spectrum analyzer. This can be partly explained by the longer lifetime of the upper laser level that results in relaxation oscillation frequencies on the order of 10 kHz. As a result, external technical noise contributions are closer to resonance and are much stronger transferred into intracavity power fluctuations, which in turn induce fast drifts of the f_{CE}. On the other hand, fiber lasers exhibit much higher cavity gain and loss, larger nonlinearities, and also larger net cavity dispersion, which is why the typically longer laser pulses experience much stronger envelope timing jitters than Ti:sapphire oscillators. In contrast to that, phase jitters of the carrier waves are not increased [130]. As a consequence, the level of CEP noise in fiber lasers is often substantially higher than in bulk lasers, which renders the CEP stabilization of such lasers more challenging. The best reported CEP

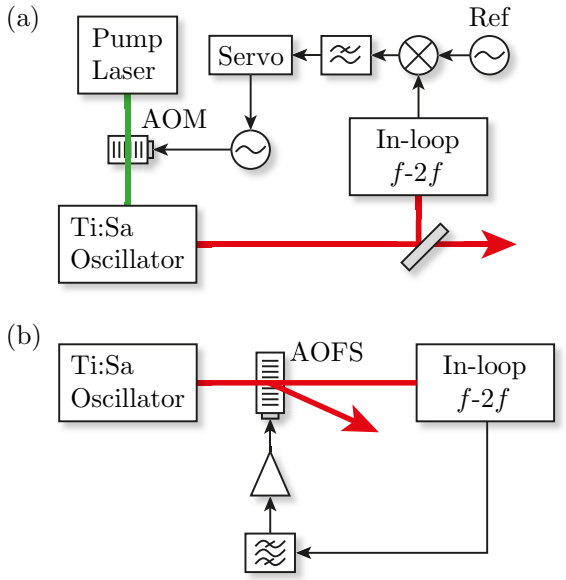

Figure 3.11: (a) Feedback CEP stabilization via back action on the oscillator pump power with an acousto-optical modulator (AOM) to lock the measured beat signal to the reference (Ref). (b) Extra-cavity feed-forward type CEP stabilization with an acousto-optic frequency shifter (AOFS).

stabilization performance was demonstrated with a fast graphene-based electro-optical loss modulator inside the cavity of a thulium fiber laser [131], which showed an rms phase jitter of 144 mrad. This result is still more than three times worse than the residual phase noise observed by Koke *et al.* with a Ti:sapphire oscillator [19] and it shows almost an order of magnitude more phase noise than the results presented below. This gap demonstrates that there is still room for improvement of the CEP stabilization performance of fiber lasers, which can potentially be filled by the feed-forward type stabilization scheme and its high control bandwidth.

Despite the proven benefits, the feed-forward type stabilization shown in Fig. 3.11(b) essentially does not represent a true feed-forward stabilization scheme, as the time lag Δt between the detection and the correction of the CEP prevents a stabilization on a shot-to-shot basis. In practice, for a time lag of $\Delta t \approx 1\,\mu$s, more than one hundred laser pulses pass the AOFS before the measured in-loop signal reaches the interaction zone. This delayed correction gives rise to a strongly frequency dependent phase response $\varphi(f_{\mathrm{CE}})$, which in turn introduces additional CEP noise if the frequency of the measured beat signal is subject to drift.

The effect of a drifting beat frequency on the CEP is readily deduced from the schematic plot in Fig. 3.12. The time delay is mainly introduced by the acoustic traveling time and to some extent by the GD of the used electronic filters. This delay corresponds to a certain phase difference $\Delta\varphi$ of the beat signal. The resulting phase error made in the correction, by itself, does not compromise the CEP stabilization as long as the phase difference stays constant over time. If, however, the frequency of the beat signal varies gradually, see the dashed and solid lines in Fig. 3.12, the phase difference changes according to

$$\Delta\varphi(t) = 2\pi\Delta t f_{\mathrm{CE}}(t). \tag{3.2.1}$$

As a consequence, a drift of the f_{CE} by only 100 kHz at a delay of $1\,\mu$s already causes a phase shift of one tenth of a full cycle, i.e., 628 mrad. The fact that such drifts easily occur in a free-running oscillator on a minute time scale strongly highlights the need for further measures to diminish the effect on the CEP by passive or active means. In the following, several different new schemes are presented that deal with the limitation of the delayed correction, which all have their advantages and disadvantages. In particular, a combination of the feed-forward and the feedback stabilization is presented in section 3.2.1, which led to new record low residual phase noise. Further concepts to address the shortcomings of the different stabilization schemes are discussed in section 3.2.2.

3.2.1 CEP Double Stabilization

The previous considerations have shown that the combination of a finite control bandwidth and a drifting frequency comb offset gives rise to significant phase noise in a feed-forward type CEP stabilization. In practice, the passive stability of the CEP slip in a Ti:sapphire oscillator pulse train is not sufficient to prevent the

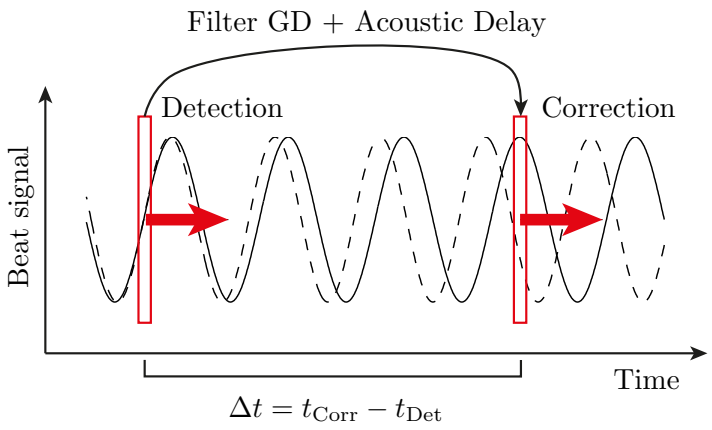

Figure 3.12: Origin of the frequency dependent phase response $\varphi(f_{\mathrm{CE}})$ of the feed-forward type stabilization scheme.

appearance of such phase drifts, even on the time scale of minutes or seconds. A possible solution to this problem is the control of the laser oscillator in order to keep the beat signal at a specific frequency. To this end, a novel stabilization setup is realized in which the feed-forward type stabilization is combined with a classical feedback loop that controls the CEP slip by the modulation of the pump power.

The schematic of the combined double stabilization setup, published in [121], is depicted in Fig. 3.13. The setup is essentially divided into three different sections that are indicated by the dashed boxes, labeled (1)-(3). While the first box represents the feedback stabilization, the second and third boxes illustrate the feed-forward stabilization and the independent out-of-loop characterization of residual phase noise, respectively. About one half of the output from a Ti:sapphire oscillator (Scientific Pro, Femtolasers), i.e., 250 mW average power at 85 MHz repetition rate and 10 fs pulse duration, is used to generate an octave-spanning spectrum by soliton fission in a 1 cm long PCF (NL-PM-750, NKT Photonics) as described in section 3.1.2. The resulting supercontinuum is then focused into an AOFS (QZF-70-10-.800, Brimrose), which is made from a 27 mm long quartz crystal and features a diffraction efficiency of 70% at a wavelength of 800 nm. To reach this efficiency the shifter has to be driven with a strong 38 dBm RF signal at 70±10 MHz, which requires active cooling of the device. The angle of incidence is tuned to optimize the diffraction efficiency of the zero and first diffraction orders, which is achieved by the symmetric situation described in Fig. 2.8, where the angle of incidence is chosen to be half the Bragg angle. The speed of sound in the quartz material is specified as 5960 m/s, which corresponds to a Bragg angle of 4.7 mrad at an acoustic frequency of 70 MHz. These numbers show that there is a further reason to keep the CEP slip of the oscillator stable, since a frequency deviation of the AOFS

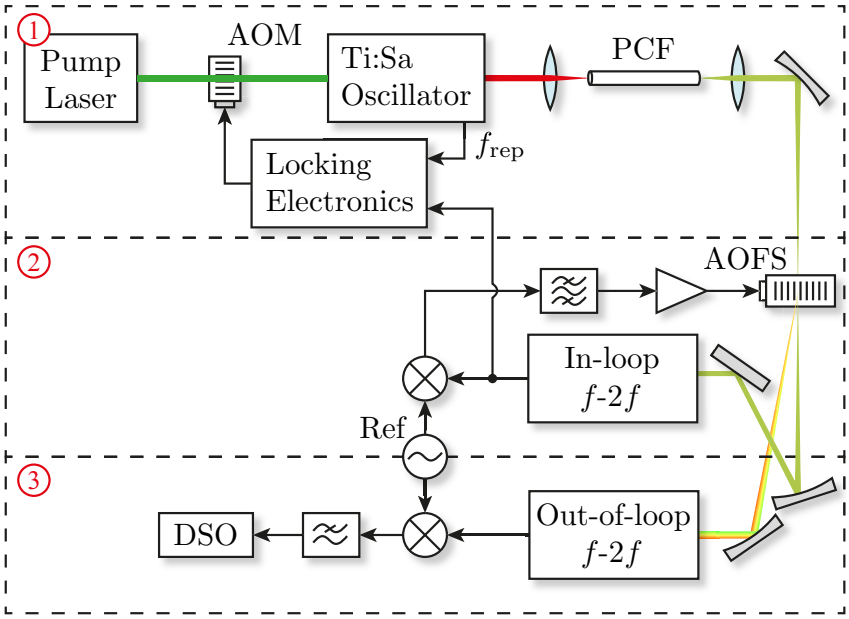

Figure 3.13: CEP stabilization scheme combining a feedback stabilization via pump power modulation (1) with a feed-forward type stabilization (2) and out-of-loop characterization of residual phase noise (3). AOM: acousto-optical modulator. PCF: photonic crystal fiber. AOFS: acousto-optical frequency shifter. Ref: reference oscillator. DSO: digital sampling oscilloscope.

driver signal by only 1 MHz already results in beam a pointing variation of 67 μrad, which can be detrimental, e.g., for seeding a subsequent amplification stage.

After re-collimation, the zero and first diffraction orders are separated and sent to two independent but identically built f-2f interferometers used for the in-loop and the out-of-loop measurements. The angular dispersion in the first diffraction order is thereby compensated by a prism pair made of SF16 glass (not shown). To exclude common phase noise features as well as a relative dephasing of the two interferometers to the extent possible, the robust dichroic quasi-common-path interferometer design presented in section 3.1.1 has been employed. The interferometers are built on a common base plate and shielded against environmental influences as best as possible.

The advantage of performing the supercontinuum generation prior to the splitting into the two diffraction orders is that the actual potential of the stabilization technique is demonstrated when both interferometers are fed with the same supercontinuum. This way the phase noise acquired during the spectral broadening process is virtually eliminated by the stabilization. For most real-life applications,

however, the fiber-based spectral broadening has to be done directly in front of the in-loop interferometer, since the temporal structure of the pulses is completely destroyed by the soliton fission process in the PCF, which is undesirable in the diffracted output that is used for the actual application.

Thanks to the optimization of the length of the PCF, see section 3.1.2, the beat signals measured in the in-loop and out-of-loop interferometer show an unprecedented RF power S/N of 60 dB and 53 dB, respectively. The fact that the out-of-loop signal does not quite reach the same S/N as the in-loop signal is partially explained by the losses at the facets of the used prisms and partially by the lower than specified AOFS diffraction efficiency at the spectral wings. Especially the efficiency in the infrared wing of the spectrum is critical, due to the additional reduction of the photon numbers during the subsequent SHG.

The first step of CEP stabilization is now to lock the in-loop measured CEP slip to a quarter of the oscillator repetition rate ($f_{\mathrm{IL}} = f_{\mathrm{rep}}/4 \approx 21\,\mathrm{MHz}$) by using the commercial locking electronics from Menlo Systmes (XPS 800). The electronics, consisting of a frequency divider, a digital phase detector, and a PID controller, generate an error signal, which in turn controls the amplitude modulation of an AOM driver that modulates the oscillator pump power. Once the feedback loop is closed and once a stable lock is established, the in-loop signal is further used to drive the AOFS for the purpose of removing residual phase noise. To this end the beat signal is mixed with an additional local oscillator $f_{\mathrm{OOL}} = 49\,\mathrm{MHz}$ to operate the AOFS at its optimal working point of 70 MHz. This way the frequency comb in the first diffraction order is stabilized to the offset $-f_{\mathrm{OOL}}$, which allows characterizing the residual phase noise by simple comparison of the measured out-of-loop beat signal and the same local oscillator in a balanced mixer. Of course, also other combinations of reference oscillators than the one presented here ($f_{\mathrm{IL}} = 21\,\mathrm{MHz}$ and $f_{\mathrm{OOL}} = 49\,\mathrm{MHz}$) are possible to produce frequency combs with arbitrary offsets. Especially the technically important case of a frequency comb with vanishing offset is readily achieved if the reference oscillator of the feedback loop is set to the working point of the frequency shifter so that the in-loop signal can be directly used as a driver signal for the AOFS. However, the proposed RF heterodyning CEP detection scheme is not capable of characterizing the residual phase noise at $f_{\mathrm{CE}} = 0$, due to the ambiguity of positive and negative frequency excursions. Such measurements in the baseband are only feasible with a balanced homodyne detection scheme [70], which requires the usage of unfavorable non-common-path interferometers and has to deal with imperfect balancing and $1/f$ noise contributions in the electronics. In order to circumvent these difficulties, the phase noise measurements were performed out of the baseband at $f_{\mathrm{OOL}} = 49\,\mathrm{MHz}$.

For the measurements presented in Fig. 3.14(a) the phase noise was recorded with a digital oscilloscope over 5 s at a sampling rate of 5 MHz. In order to identify the effect of the additional feedback loop, the noise was measured for the double stabilization (red trace) as well as for the feed-forward stabilization without the feedback loop (gray trace). The comparison reveals much stronger phase noise in

the latter case, which shows up as a slow drift in the moving average, but also as a higher phase jitter on shorter time scales. The fact that the measured phase noise is flat over the entire trace in case of the double stabilization confirms that the phase excursions observed for the open loop are indeed caused by the variations of f_{CE}, which are then suppressed by closing the loop.

For further insight, a Fourier analysis of the measured noise traces is given by the single-sided phase noise density σ_φ plotted in Fig. 3.14(b). The additional black trace is the result of a background measurement, which represents the shot noise-induced detection limit of the out-of-loop interferometer. This measurement is realized simply by detuning the temporal delay of the f and $2f$ components until no amplitude modulation remains. Owing to the strong improvement of the S/N in both interferometers, the stabilization of CEP noise is not limited by shot noise up to a frequency of some 10^5 Hz, which is in strong contrast to the results in [19], where the performance was limited by shot noise over almost the whole resolved frequency range. It has to be noted that the background measurement as well as the double stabilization measurement have been corrupted by some other unknown RF source in the range of the detection frequency. This parasitic signal corresponds to a comb of equally spaced lines, which is not visible in the logarithmically plotted PND in Fig. 3.14(b), due to a reduction of the printer resolution. These features, however, are very narrow-band and do not significantly contribute to the overall phase noise but are responsible for the distortion of the noise floor in the frequency region around 1 MHz.

Comparing the noise densities of the different stabilization schemes, one finds that closing the feedback loop strongly reduces the phase noise at all frequencies below some 10^4 Hz. Especially in the acoustic region from 10 Hz to 5 kHz, where a lot of technical noise is influencing the beat frequency, the PND is reduced by two orders of magnitude. Above this region at 10^5 Hz, though, the PND of the double stabilization is slightly increased by a rather broad noise band that is caused by the servo electronics, marking the limited control bandwidth of the feedback loop. In the low frequency region both stabilization schemes give rise to characteristic $1/f$ noise, which is shifted to lower frequencies for the double stabilization setup. The underlying physical origin of this characteristic low frequency noise is still unresolved. To some extent such noise scaling can be explained by a slow dephasing of the interferometers, but even measurements with the most stable common-path interferometers give rise to similar results [75]. A different approach to explain why such $1/f$ noise can not be fully suppressed is that quantum noise inside the laser oscillator transfers into uncorrelated white noise of f_{CE}, which then accumulates on long time scales to the observed CEP noise [120].

In Fig. 3.14(c) the integrated phase noise, see Eq. (3.1.7), is plotted as a function of the lower integration limit, revealing that the total integrated rms phase jitter (0.2 Hz – 2.5 MHz) is reduced from more than 80 mrad to 20 mrad if the additional feedback loop is closed. Given that the duration of one optical cycle at 800 nm is 2.7 fs, this phase error translates into a carrier-envelope timing jitter of only 8 as,

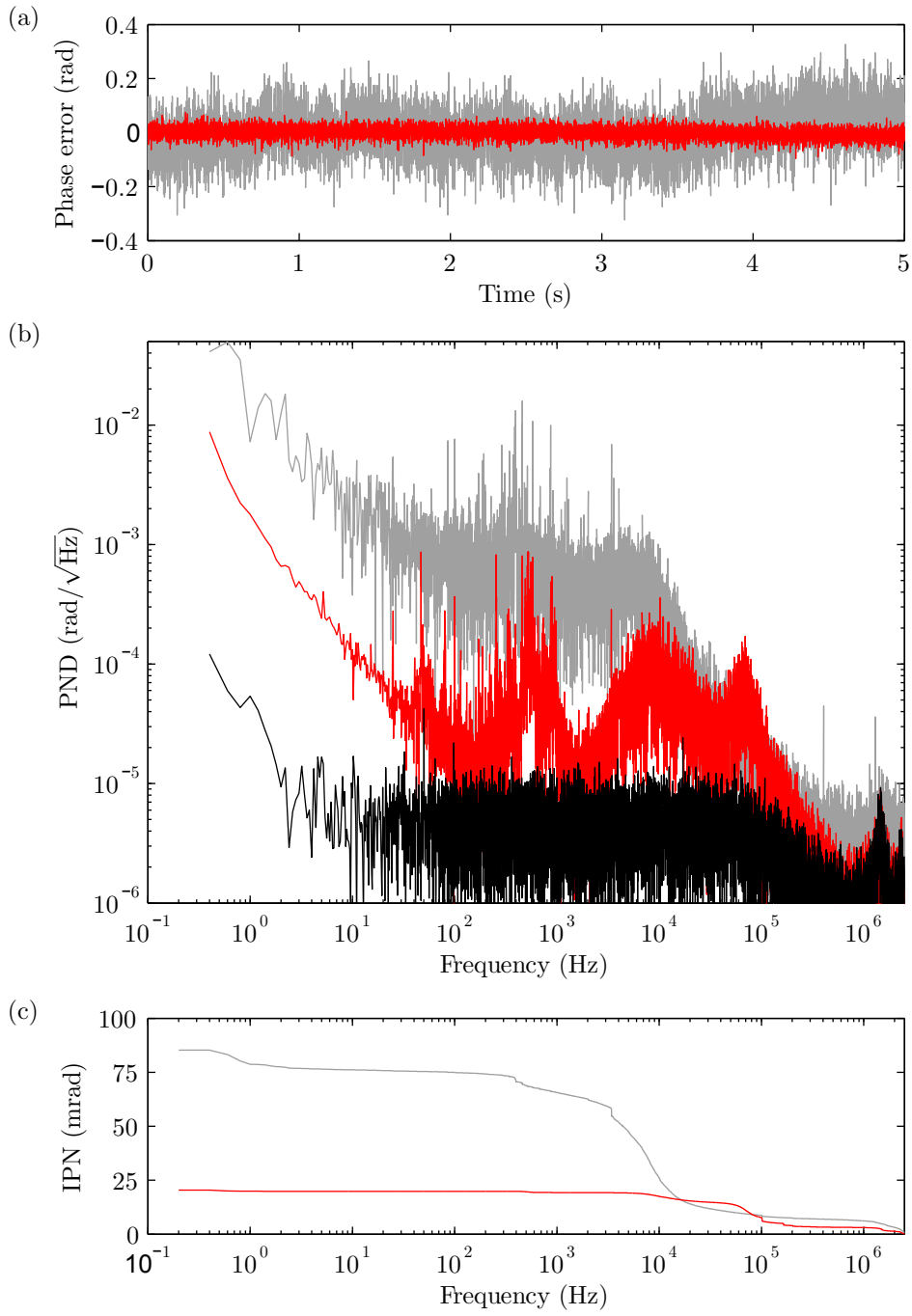

Figure 3.14: (a) Residual phase noise sampled at 5 MHz for the double stabilization setup (red trace) and for the feed-forward type stabilization only (gray trace). (b) Single-sided phase noise densities (PND) for both measurements as well as the detection noise. (c) Integrated phase noise (IPN) vs. frequency with integration starting at 2.5 MHz.

which represents, in all conscience, the most precise timing control of a physical quantity obtained so far.

Table 3.1 provides a comparison of the best reported CEP stabilization results that have been obtained with a feedback stabilization, a feed-forward stabilization, and with the demonstrated combination of both. Moreover, the measured phase jitters are plotted in Fig. 4.1 as a function of the respective S/N (full symbols), together with the determined detection limit (hollow symbols). Since the results were measured at different sampling rates, the calculated scaling of the detection noise-induced phase jitter for various upper integration limits is added to the plot (black lines), for comparison. It is remarkable that even though the setup from Koke *et al.* was mostly limited by detection shot noise (see low spread of the full and hollow symbols), the achieved 45 mrad rms CEP jitter was already two times lower than the 100 mrad jitter obtained by Fuji *et al.* with a feedback stabilization and a much higher S/N. This improvement remains even when the higher sampling rate of the latter work is taken into account, which clearly demonstrates the superiority of the feed-forward scheme. Compared to the results of Koke *et al.* the double stabilization presented here gives rise to another more than twofold reduction of the CEP jitter.

At the same time the double stabilization scheme enables long-term operation at this high level of CEP stability, given that the feedback loop is made sufficiently robust. In principle already a rather low loop bandwidth is sufficient to keep the CEP slip coarsely at the defined set point, which allows using mechanical feedback mechanisms, such as the translation of intracavity wedges.

Scheme	Reference	$\delta\varphi(f_{\mathrm{low}}, f_{\mathrm{high}})$	$f_{\mathrm{low}} - f_{\mathrm{high}}$	S/N
Feedback	Fuji *et al.* [69]	100 mrad	0.2 mHz – 35 MHz	55 dB
Feed-forward	Koke *et al.* [19]	45 mrad	0.2 Hz – 2.5 MHz	40 dB
Double stabilization	This work [121]	20 mrad	0.2 Hz – 2.5 MHz	60 dB

Table 3.1: Comparison of the best CEP stabilization results obtained with different stabilization schemes.

In summary the presented double stabilization setup achieves unprecedentedly high CEP stability, which is furthermore available for previously impossible long-term experiments, e.g., in attosecond science or frequency metrology.

3.2.2 Further Schemes for CEP Stabilization

The double stabilization scheme presented in the previous section has resolved the issue of additional phase noise in a feed-forward type stabilization that arises due to the inevitably delayed correction and a drifting beat frequency f_{CE}. Solving this problem with a feedback loop, however, comes at the expense of the characteristic drawbacks of the feedback approach. Any intervention in the intracavity dispersion

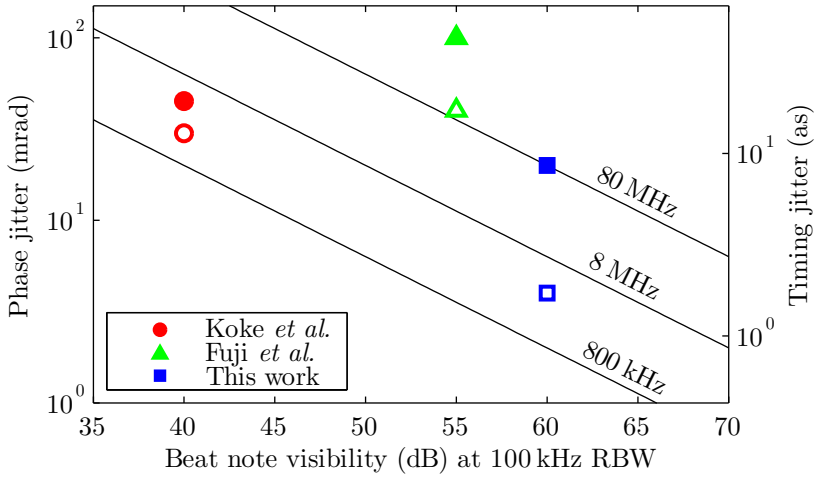

Figure 3.15: Comparison of the best reported CEP stabilization results obtained with a feed-forward type stabilization (Koke *et al.* [19]), a feedback stabilization (Fuji *et al.* [69]) and the double stabilization presented in this work. Full symbols represent the residual phase noise while hollow symbols correspond to the detection noise. For guidance, the calculated detection noise-induced phase jitters of an 80 MHz pulse train are indicated for different upper integration limits.

of the oscillator is accompanied by crosstalk to other laser parameters, such as output power or repetition rate, which are severe restrictions for amplifier as well as metrology applications. Additionally, the double stabilization increases the phase noise in the frequency range, where the control bandwidth of the feedback loop ceases. These arguments show that the presented double stabilization is still not the ideal solution to the issues of the feed-forward scheme and that a side effect-free CEP stabilization scheme, if existent, remains to be found. In order to come closer to this ideal conception, in the following several further CEP stabilization schemes will be discussed that deal with the limitations imposed by the delayed correction, all of which are working without any feedback to the laser oscillator.

True feed-forward stabilization via optical retardation

In principle, the total delay of the correction in a feed-forward type CEP stabilization could be minimized to increase the available control bandwidth and to lessen the effect of a drifting beat signal. In practice, however, the potential for such an optimization is rather limited, as the acoustical traveling time can not be made arbitrarily short without risking a damage of the electro-acoustic transducer. Moreover, the necessity to use electrical filters imposes a limitation, as these filters, depending on the steepness of their absorption characteristic induce a certain group delay in accordance with the Kramers-Kronig relation, see Eq. (2.1.25). Such electronic group delays easily amount to more than 100 ns even for several MHz wide bandpass filters, which is why the total group delay of a frequency shifter-based control mechanism cannot be reduced to significantly less than 500 ns.

The only way to further increase the control bandwidth is to perform the in-loop measurement prior to the correction in the AOFS and to add a subsequent optical delay line that ideally matches the delay of the correction mechanism. This way it can be made sure that each laser pulse experiences the correct phase shift in the AOFS, resulting in a true feed-forward CEP stabilization on a shot-to-shot basis. An appropriate delay line, however, requires the propagation over 150-300 m to fully bridge the time delay of the error signal. While the implementation of such large delays can be managed in completely fiber-intergated systems, it represents a challenging task for the free space propagation of ultrashort laser pulses. In fact, the strong impact of dispersion and diffraction on the beam over such long propagation distances makes the feasibility of the approach questionable. A potential solution to this problem is illustrated in Fig. 3.16(a), where an evacuated multipass cell is used as a folded optical delay line [132]. While such Herriott cells are typically used for spectroscopic absorption experiments, they provide a convenient way of introducing large optical delays within a compact setup. Naturally, the demands on the mechanical stability of the cell design as well as the necessary mirror quality are rising with the number of necessary reflections. As the current application realistically requires several hundred optical reflections, very large and precisely fabricated aspherical mirrors have to be used, making the overall cell design very costly.

Apart from these admittedly challenging technical difficulties, the scheme presented in Fig. 3.16(a) holds the unique potential for a true shot-to-shot CEP stabilization without sensitivity to f_{CE} drift. Only if the drift of the CEP slip becomes very large (>10 MHz), the AOFS driver signal diverges too much from the nominal working point and a drop in diffraction efficiency will be observed. The frequency comb offset of a thermalized Ti:sapphire oscillator, though, typically stays within a range of ±10 MHz at least for several hours making long term measurements possible. Nevertheless, a remaining issue of this stabilization scheme is still the uncompensated impact of a changing AOFS driver frequency on the diffraction angle, causing beam pointing variations of the CEP stabilized output.

Feed-forward stabilization with electronic group delay compensation

Instead of introducing an optical delay, as proposed in the previous section, the frequency dependent phase response $\varphi(f_{\mathrm{CE}})$ in the feed-forward type stabilization can also be addressed by a much easier to implement electronic compensation. This can be achieved by either active or passive means.

For an active compensation technique, the current beat frequency is monitored with an electronic frequency-to-voltage converter, the output voltage of which is then used to control the phase of the electric signal with an RF phase shifter. Given that the error voltage is properly mapped to the phase interval of the phase shifter, the corrected AOFS driver signal will no longer show the f_{CE} dependent phase response. Of course, the active electrical components possess an intrinsic response time, which is why f_{CE} jitters can only be corrected up to a certain bandwidth in the kilohertz range. Besides the discussed compensation technique, the employment of an adjustable RF phase shifter opens an additional possibility, i.e., the integration of a further CEP stabilization feedback loop for a low-repetition amplifier system that works without any side-effects on other laser parameters.

Another elegant way of compensating the frequency dependent phase response is given by a completely passive scheme, which extrapolates the phase of the currently measured beat signal to the instant of time at which the interaction with the optical frequency comb takes place. Assuming that the total delay of the error signal amounts to $\Delta t = 1\,\mu$s, one has to artificially age the beat signal exactly by this amount of time. To perform such an extrapolation one needs the information on how the phase has evolved within the last microsecond. Mathematically the extrapolated phase is given by the difference of twice the current phase and the phase from one microsecond ago

$$\varphi(\Delta t) = 2 \cdot \varphi(t=0) - \varphi(-\Delta t) \tag{3.2.2}$$

$$= 2 \cdot (\omega_{\mathrm{CE}} \cdot 0 + \varphi_0) - (-\omega_{\mathrm{CE}}\Delta t + \varphi_0) = \omega_{\mathrm{CE}}\Delta t + \varphi_0, \tag{3.2.3}$$

which implies that the beat frequency ω_{CE} does not change within the full two microsecond time span. In practice, the phase extrapolation therefore results in a two times lower control bandwidth.

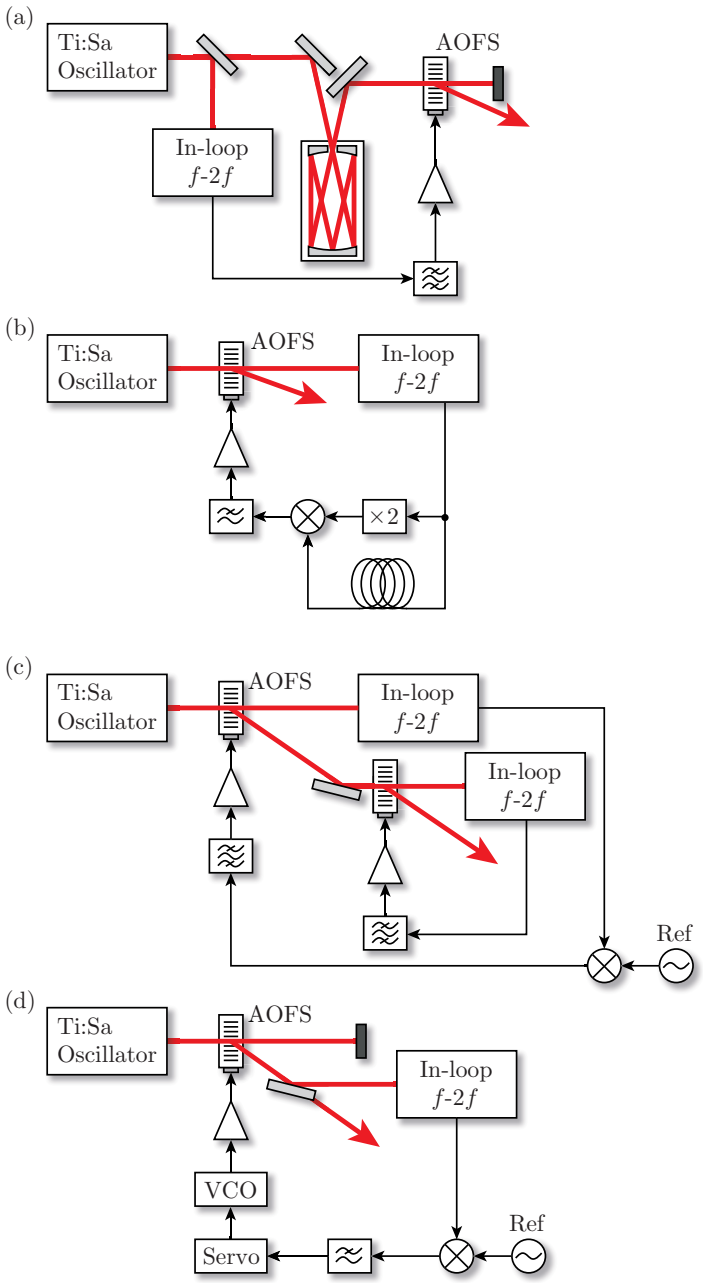

Figure 3.16: Different CEP stabilization schemes. (a) True feed-forward stabilization by optical retardation. (b) Feed-forward type stabilization with group delay compensation. (c) Cascaded feed-forward stabilization. (d) Feedback stabilization with an AOFS.

The electrical realization of this mathematical operation is given by frequency doubling of the currently measured beat signal and a subsequent mixing process with the delayed beat signal, as it is depicted in the wiring diagram in Fig. 3.16(b). Afterwards, the resulting mixing products are low-pass filtered to isolate the difference frequency signal at ω_{CE} from the sum frequency signal. The electronic delay line can be simply realized by a respective cable of several hundred meter length, which, however, requires the compensation of the strong electrical attenuation. An alternative delay line is given by an electro-optic transceiver, which transmits the signal over an almost lossless optical fiber link of the necessary length.

In total the described measures provide a rather easy to implement electronic compensation of the group delay-induced phase response in a feed-forward type CEP stabilization. A minor issue of the described passive scheme is the reduction of the control bandwidth by factor of two.

Cascaded feed-forward stabilization

So far different schemes have been discussed that aim at a precompensation of the frequency-dependent phase response in a feed-forward stabilization by optical or electrical means. In contrast to that, another approach to prevent such residual phase noise is given by the use of two successive AOFS, as illustrated in Fig. 3.16(c). This concept is very similar to the double stabilization presented in section 3.2.1, with the only difference being that the feedback loop is replaced by another feed-forward stabilization. In this case, the first shifter and the first in-loop interferometer are used to stabilize the CEP slip to a certain reference oscillator at f_{ref}. The residual phase noise present in the stabilized output is then measured with a second interferometer and fed to the second AOFS placed in the first diffraction order of the first shifter. Since the second shifter is constantly driven by a beat signal at f_{ref}, the frequency dependent phase response $\varphi(f_{\mathrm{CE}})$ is not compromising the CEP stability after the second shifter. This way a frequency comb with vanishing offset is generated in which all pulses exhibit the identical field structure, even if the frequency of the in-loop beat signal is subject to drift.

The downside of the presented scheme is that two frequency shifters and two separate interferometers result in a more complex setup and in a reduced total output power, due to the squared AOFS diffraction efficiency. To keep the losses at a minimum it is mandatory to place the interferometers in the respective zero diffraction orders, which would be wasted otherwise. A further problem could arise from the beam pointing variations of the first AOFS that cause small lateral shifts of the acousto-optical interaction zone in the second AOFS. Such translations of the beam relative to the index grating would introduce new phase noise. To prevent the appearance of such artifacts, the distance between the two successive shifters has to be kept as small as possible.

Feedback stabilization with an acousto-optical frequency shifter

Apart from all the feed-forward stabilization schemes presented above, an external AOFS can also be used for a classical feedback stabilization. The feedback approach has the advantage that the frequency-dependent phase noise does not survive within the loop bandwidth, since the phase detection is performed only after the correction signal has been applied. Moreover, feeding the error signal back to an external AOFS rather than to the oscillator itself eliminates the issue of the crosstalk to other laser parameters.

Figure 3.16(d) shows the schematic of such an extracavity feedback loop, where the in-loop error signal is measured in the first diffraction order of the AOFS rather than in the unaffected zero order. After phase comparison to an RF reference oscillator, the resulting error signal is used to control a VCO, which in turn drives the AOFS to close the loop. If one compares the present scheme to the usual feedback loop, the combination of the electrical VCO and the AOFS is taking over the role of the pump power modulated oscillator. A very similar feedback scheme was used in [6] to control the relative frequency comb offset of two independent laser sources.

Besides the remaining issues of the feedback approach, such as the limited loop bandwidth and the difficulty to produce frequency combs with vanishing offset frequency, the presented scheme provides a suitable stabilization technique that is insensitive to drifts of the free-running f_{CE}. Still, another drawback is the reduction of the usable output power, that is caused by the in-loop measurement in the diffracted beam.

Overview of the presented oscillator CEP stabilization schemes

A brief overview of the different stabilization schemes that have been presented throughout this thesis and a summary of their respective advantages and disadvantages is provided by Table 3.2.

Apart from the regular feedback stabilization with back action to the oscillator, five other schemes have been proposed, all of which are capable of removing the frequency dependent phase response observed in the feed-forward stabilization. However, only the double stabilization, which combines the feed-forward scheme with a feedback loop, eliminates the issue of beam pointing variations of the diffracted beam, as the AOFS driver frequency is always kept constant. Moreover, the double stabilization provides a high control bandwidth, but suffers from the crosstalk to other laser parameters. The true feed-forward scheme, on the other hand, provides the highest possible control bandwidth, but has to deal with the challenging optical delay line. This issue can be circumvented by the electrical compensation of the GD, which reduces the control bandwidth by a factor two compared to the feed-forward type stabilization. Another possibility of dealing with the frequency dependent phase response is the cascading of the feed-forward stabilization, which comes at the cost of a more complex setup and less optical

Scheme	$\varphi(f_{CE})$	Pointing	Control BW	Further Issues
Feedback to laser	-	-	10-100 kHz	Crosstalk
Feed-forward type	✓	✓	1-2 MHz	-
Feedback + feed-forward	-	-	1-2 MHz	Crosstalk
True feed-forward	-	✓	shot-to-shot	Delay line
Feed-forward + GD compensation	-	✓	0.5-1 MHz	-
Cascaded feed-forward	-	✓	1-2 MHz	Less output power
Feedback to AOFS	-	✓	100 kHz	Less output power

Table 3.2: Comparison of the key features of the different oscillator CEP stabilization schemes presented in this thesis.

output power. Finally, the AOFS can also be employed for an extracavity feedback scheme, which nonetheless comes with some of the general disadvantages of feedback loops.

The decision about which stabilization schemes after all represents the best solution, depends on the actual application and on the type of laser source to be stabilized. In particular, one has to take into account which type of crosstalk can be tolerated and which not. Naturally, a main criterion is the achievable stabilization performance, which still has to be experimentally investigated for the presented further schemes. From this perspective, it remains to be seen if the proposed techniques are able to keep up with the outstanding CEP stabilization performance of the double stabilization setup, presented in section 3.2.1.

Chapter 4

Limitations in CEP Stabilization of Amplified Laser Systems

While the previous chapter has treated the general limitations of the CEP stabilization of mode-locked oscillators, the following chapter represents a review of the most limiting constraints for the stabilization of amplified laser systems. To this end, the first section deals with technical issues that arise due to fluctuations of the environmental conditions and due to noise from the pump and seed laser. Furthermore, a new concept for a pulsed oscillator CEP stabilization is presented that is specifically designed for seeding a subsequent amplifier, solving some of the remaining issues of the feed-forward type stabilization. In contrast to these technical considerations, the second section covers the more fundamental limitation of shot noise that is also present in the detection of residual CEP noise of amplified laser pulses.

4.1 Technical CEP Noise Sources of Amplified Laser Systems

The CEP stability of amplified laser pulses is affected by fluctuations of the same environmental parameters that have already been discussed for the case of mode-locked oscillators, such as air pressure, humidity and temperature. Helbing *et al.* have estimated that a variation of the air pressure by 1 Pa induces a change of the CEP by 1 mrad for a propagation distance of 10 m [26]. Moreover, they estimated that a 1 K temperature difference of the Ti:sapphire crystal in a multipass chirped-pulse amplification (CPA) system with an effective crystal length of 10 cm results in a CEP change of 1.9 rad. With regard to the low repetition rates of amplifier systems and the commonly required long-term CEP stability, such variations of the lab environment can play a decisive role, even though shielding of the laser system typically allows the minimization of such effects to rather slow phase drifts

on longer time scales of minutes and hours.

For the compensation of such effects, the CEP drifts are typically measured by spectral interferometry, see section 2.4.2, and controlled with an additional slow feedback loop that is either combined with the control mechanism of the oscillator stabilization [133] or with some independent second control mechanism. Frequently, the CEP is controlled by the amount of material dispersion in the beam path with a pair of glass wedges [134] or by the introduction of geometrical dispersion in stretcher or compressor setups [135]. Apart from these slow mechanical feedback mechanisms, the CEP control was also demonstrated with a programmable acousto-optical dispersive filter (Dazzler) [136, 137], and with electro-optical modulators [113, 138].

Next to the varying environmental conditions, fluctuations in the laser parameters of the pump laser and the seed laser can strongly affect the CEP stability of the amplified laser pulses as well. Especially the relative intensity noise (RIN) of these lasers results in broadband CEP noise due to amplitude-to-phase coupling. The strength of this effect can be estimated for a given laser system from the dispersion of the nonlinear refractive index in the laser crystal $n_2(\omega)$ and the amplifier B integral $B = 2\pi/\lambda \int n_2 I(z)\mathrm{d}z$, which corresponds to the total nonlinear phase shift that is acquired along the optical path of the amplifier.

In order to quantify the amplitude-to-phase coupling of a typical Ti:sapphire amplifier, the nonlinear dispersion of sapphire was calculated according to the theoretical framework described in [90]. This model is based on the connection of the real and the imaginary part of the third order susceptibility, which is given by a nonlinear version of the Kramers-Kronig relation (compare to Eq. (2.1.25))

$$n_2(\omega) = \frac{c}{\pi} \int_0^\infty \frac{\alpha_2\left((\omega+\Omega)/2\right)}{\Omega^2 - \omega^2}\, \mathrm{d}\Omega, \tag{4.1.1}$$

where $\alpha_2(\omega)$ represents the degenerate two-photon absorption (TPA) coefficient [93, 95]. Besides the TPA, this theoretical model also includes further contributions from the Raman-effect and the ac-Stark effect [90]. The calculated dispersion profile, depicted in Fig. 4.1, is in good agreement with the experimental results from [139] that have been measured with the z-scan technique described in [140]. From these results the effective nonlinear group-phase offset coefficient is determined for a center wavelength of 800 nm: $\omega_\mathrm{c}\,(\mathrm{d}n_2/\mathrm{d}\omega)|_{\omega_\mathrm{c}} = 3.3 \times 10^{-17}\,\mathrm{cm}^2/\mathrm{W}$. This value corresponds to about 12% of the nonlinear refractive index at this wavelength: $n_2(\omega_\mathrm{c}) = 2.9 \times 10^{-16}\,\mathrm{cm}^2/\mathrm{W}$. Given the fact that the B integral in most amplifier systems is kept on the order of 2π to prevent catastrophic self focusing and other detrimental nonlinear effects, one can conclude that typical fluctuations of the amplifier output power of 1% correspond to only 8 mrad of phase jitter. This estimate, however, is by far lower than the phase jitters that reportedly lie in the range of 100-300 mrad, where the actual values depend on whether the acquisition of CEP noise uses averaging over multiple laser shots [78, 115, 138, 141].

This discrepancy can be explained to some extent by the fact that already the

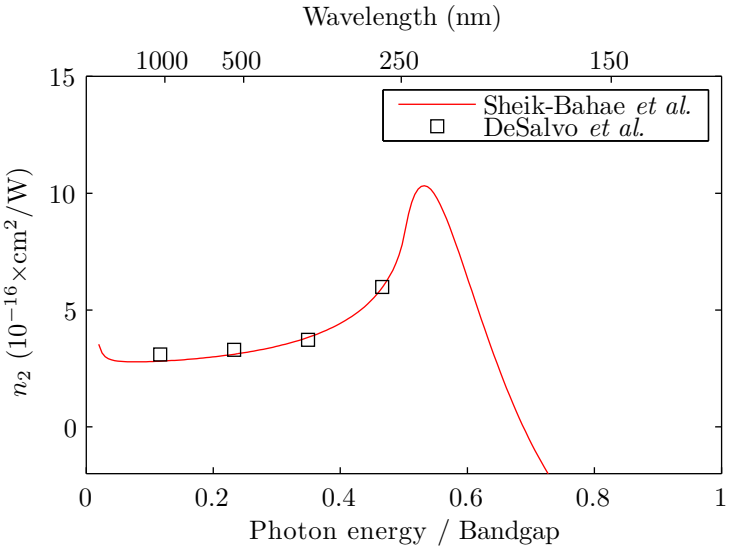

Figure 4.1: Dispersion of the nonlinear refractive index n_2 of sapphire. Calculation according to the theoretical framework presented in [90] (red line) and experimentally determined values (black squares) taken from [139].

residual phase noise of the oscillator stabilization constitutes a major part of the observed phase jitters. Another contribution to this mismatch is that the CEP detection of amplified pulses is much stronger affected by amplitude noise than the amplification process itself, due to the strong nonlinear interaction in the process of spectral broadening that is required for the spectral interferometry measurements. For the supercontinuum generation by filamentation in a sapphire substrate, Baltuška *et al.* have measured that an amplitude modulation of 1% already leads to an optical phase shift of 84 mrad [115], showing that the B integral for the broadening process is an order of magnitude higher than the nonlinear phase shift in the amplifier. Besides the fact that this coupling mechanism strongly limits the detection and the compensation of residual CEP noise, it also implies that amplifier systems which are externally broadened, e.g., by hollow fiber compressors, suffer from increased amplitude-to-phase coupling. If the CEP stabilization is supposed to be maintained for such compressed laser pulses, special care has to be taken to minimize amplitude noise from the pump and seed lasers to the extent possible.

Another source of CEP noise that is stemming from the pump and seed lasers are slow variations of the beam pointing, which couple to the CEP either indirectly by influencing the laser power via changes in the alignment or by geometrical effects in dispersive elements. In the stretcher and compressor sequences of CPA systems such beam pointing variations can strongly affect the dispersion and thus the CEP stability, especially for compressor/stretcher designs that make use of imaging optics. It has been reported that beam pointing variations must not exceed

the few-μrad range in such systems in order to preserve the CEP stability [26, 142]. Moreover, it should be mentioned that also the self-refraction at the Brewster-cut Ti:sapphire crystal induces a power dependent beam steering effect, which results in a complex mutual interplay of power fluctuations and beam pointing variations.

It has been discussed in section 3.2 that all of the presented feed-forward type stabilization schemes suffer from beam pointing variations of the diffracted output if the frequency of the AOFS driver signal is subject to drift. For the AOFS used in the presented oscillator stabilization experiments, this frequency dependent steering effect is as strong as 67 μrad/MHz, showing that seeding of a subsequent amplifier requires an additional feedback loop to lock the CEP slip to a reference frequency, as it was demonstrated by the double stabilization scheme in section 3.2.1. In the next section a new beneficial concept for the CEP stabilization of oscillators will be presented that is specifically designed for seeding an amplifier with short bursts of CEP stabilized pulses at the reduced amplifier repetition rate. This new concept is capable of removing the beam pointing issue without any feedback to the oscillator.

4.1.1 Acoustic Frequency Combs

Next to the previously discussed issue of beam deflections in the feed-forward type CEP stabilization of a free-running oscillator, a further issue arises if the CEP slip and with it the frequency of the AOFS driver signal is drifting too far from the optimal working point. Eventually, for a shift of f_{CE} by several MHz, the bandwidth of the used RF filters or even the bandwidth of the frequency shifter is exceeded, and a drop in the diffraction efficiency is observed.

These issues of the feed-forward scheme are now addressed by a novel concept for oscillator CEP stabilization that is virtually immune against a drifting beat signal and provides further advantages for the use with an amplifier system. The main idea behind this new concept is that it is not necessary to stabilize the CEP of every single oscillator pulse due to the reduced repetition rate of the amplification stage. In fact, it is already sufficient if the CEP is repeating every Nth pulse, if N is the ratio of the oscillator and the amplifier repetition rate: $f_{\mathrm{amp}} = f_{\mathrm{rep}}/N$. To achieve this condition the driver signal of the AOFS has to be of the form:

$$f_{\mathrm{AOFS}} = f_{\mathrm{CE}} + m f_{\mathrm{amp}} \quad m \in \mathbb{N}. \tag{4.1.2}$$

This way the offset of the stabilized frequency comb is a multiple integer of the amplifier repetition rate and the value of the CEP is recovered exactly after N consecutive oscillator pulses. It is crucial for the present stabilization scheme that the same result is achieved for every superposition of these driver frequencies as well. In practice, this allows to drive the AOFS with a narrowly spaced electrical frequency comb, described by (4.1.2).

The technical implementation of this stabilization scheme is illustrated in the schematic wiring diagram in Fig. 4.2. At first, the amplifier timing unit is used

to trigger the generation of very short electrical pulses with very steep rising and falling edges ($< 1\,\mathrm{ns}$) at the reduced repetition rate f_{amp}. As indicated by the subplot (1) in the right column of Fig. 4.2, these pulses correspond to a broad and narrowly spaced electrical frequency comb with a nearly constant spectral envelope over a wide frequency range. This frequency comb is filtered and shifted by the in-loop beat signal f_{CE} via multiplication in a mixer, yielding a new frequency comb of the form (4.1.2). Another bandpass filter centered around the optimal working point of the AOFS (f_{BP}) is then used to select some lines of the new frequency comb for driving the shifter with short electrical wave-packets that are repeated at the amplifier repetition rate f_{amp}, see also location (3) in Fig. 4.2. Inside the AOFS these transient signals are converted into acoustical wave-packets, which can also be seen as an acoustic frequency comb. For every trigger event the interaction with the optical frequency comb gives rise to the diffraction of a short burst of oscillator pulses. Characterization of these optical pulses is performed with an out-of-loop f-$2f$ interferometer, which detects the transient beat signals at the frequency

$$f_{\mathrm{CE,OOL}} = (f_{\mathrm{CE,IL}} - f_{\mathrm{BP}}) \bmod f_{\mathrm{rep}}. \tag{4.1.3}$$

Even though the CEP is still slipping from pulse to pulse at a rate that equals the frequency of the out-of-loop beat signal, see also subplot (4), the CEP is repeating every N oscillator pulses, which is observed as a constant phasing of the transient beat signals from one burst to another.

One major advantage of this pulsed stabilization scheme is that regardless of how far the beat signal f_{CE} is drifting over time, there will always be some lines of the synthesized frequency comb covering the spectral region around f_{BP} at which the frequency shifter is operated. Accordingly, a driver signal with a steady signal level and thus also a constant diffraction efficiency can be maintained as long as the "real" beat signal is not interfering with the mirror beat, see also subplot (2) in Fig. 4.2. This ambiguity ultimately limits the amount of drift that can be tolerated to $f_{\mathrm{rep}}/2$. Another advantage of the new concept is that the carrier frequency of the acoustic wave-packets is kept constant due to the fixed bandpass filter in front of the AOFS. In fact, it is only the phase of the electrical transients that is adjusted by probing the in-loop beat signal with the short electrical gate pulses. As a result, the diffraction angle of the first diffraction order is invariant, which removes the issue of beam pointing variations in the shifter-based stabilization scheme.

Apart from the increased immunity against a drifting beat signal, the pulsed operation also lessens the thermal load of the AOFS by reducing the overall average RF power. Depending on the actual duty cycle of the electrical wave-packets, the usually very high average RF power of 5-10 W in the continuous mode can be easily reduced a hundred or even a thousand times, thereby eliminating the need for active cooling and alleviating the risk of a thermal damage. Potentially, the gained safety margin can be exploited to drive the shifter with even stronger electric signals to further increase the diffraction efficiency.

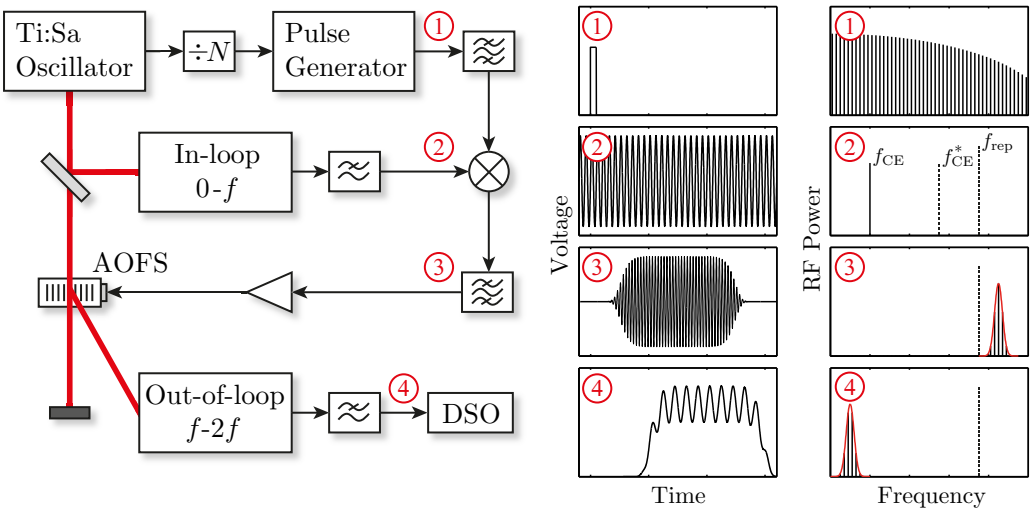

Figure 4.2: Left column: schematics. ÷N : frequency divider. AOFS: acousto-optic frequency shifter. DSO: digital sampling oscilloscope. Middle column: voltage vs. time at four different locations in the signal processing chain. (1) trigger pulse after pulse generator. (2) in-loop beat signal. (3) AOFS driver signal. (4) out-of-loop beat signal. Right column: corresponding RF power spectra.

Although not shown in the schematic in Fig. 4.2, it is also feasible to perform the in-loop f_{CE} measurement in the otherwise unused zero diffraction order of the AOFS, which is particularly beneficial for the pulsed scheme. At the instant of time when the AOFS driver signal is synthesized, the full oscillator power is still available in the zero diffraction order for the CEP detection, as no optical power is diffracted yet. The resulting strong light levels in the nonlinear interferometer guarantee the best possible S/N of the beat signal, as it was discussed in section 3.1. Only when the acoustic wave-packet reaches the interaction zone, the major part of the power is switched to the first diffraction order to seed the subsequent amplifier with CEP stabilized laser pulses. This switching is then repeated back and forth at every trigger event, enabling optimized power levels for both the in-loop CEP detection and the actual application.

Experimental Verification

The experimental verification of the pulsed stabilization scheme was performed in a collaboration of the Max-Born-institute and Femtolasers Produktions GmbH. The proof-of-concept experiments have been conducted together with Fabian Lücking and the results were commonly published in [143].

The CEP stabilization setup is based on a commercial Ti:sapphire oscillator (Femtolasers, Rainbow) that provides about 300 nm broad spectral content at a repetition rate of $f_{\mathrm{rep}} = 73\,\mathrm{MHz}$. This broad initial spectrum allows the measurement of the in-loop beat signal with a very stable monolithic 0-f interferometer, which performs the spectral broadening and the DFG in the same nonlinear PPLN crystal, as it was described in section 3.1.1. Due to the lack of a second monolithic interferometer, the out-of-loop beat signal is characterized with a classical fiber-based f-$2f$ interferometer that has already been used in previous experiments [95]. In order to circumvent the difficulty of aligning the out-of-loop interferometer in a pulsed mode, the beat signal was first optimized in a continuous mode before applying the new signal synthesis scheme. This enabled 40 dB and 50 dB S/N (100 kHz RBW) of the in-loop and out-of-loop beat signals, respectively.

For the electrical signal synthesis, the reduced repetition rate of a virtual amplification stage was deduced from the oscillator repetition rate f_{rep} with a variable frequency divider ($\div N$), which allowed the variation of f_{amp} in the range from 5,200 Hz to less than 1 Hz. Next, a pulse generator (SRS DG535) is used to produce steep rectangular pulses of 30 ns length, which are then mixed with the in-loop beat signal in a double balanced mixer. The filtering of the electrical frequency comb is performed with a narrowband 300 kHz surface acoustic wave (SAW) bandpass filter centered around $f_{\mathrm{BP}} = 85\,\mathrm{MHz}$ at the optimal driver frequency of the AOFS. The advantage of this narrow bandpass filter is the generation of rather long electrical transients with a duration of more than $3\,\mu\mathrm{s}$, simplifying the phase retrieval from the recorded transient out-of-loop beat signals. Moreover, SAW filters possess very low temperature coefficients in the ppm/K range, which lead to very stable center frequencies, thus reducing beam-pointing variations to a minimum.

The resulting out-of-loop beat signals are recorded with an oscilloscope (R&S RTO 1014) in memory segmentation mode, making it possible to use the internal memory most efficiently by pausing the data acquisition in between the individual transients. This way more than 18,000 consecutive transients can be recorded in a single measurement, which allows monitoring the evolution of the CEP over 3.5 s, given that the amplifier repetition rate is set to $f_{\mathrm{amp}} = 5.2\,\mathrm{kHz}$. In Fig. 4.3 histogram plots of such out-of-loop measurements are displayed for different beat frequencies, where the histogram information is encoded in the color scale. The measurements depicted in Fig. 4.3(a-c) show clear sinusoidal signals with only little apparent phase jitter, where the beat frequency has been massively varied by more than 10 MHz. From these results it becomes evident that the scheme is capable of sustaining the CEP stability also for free-running oscillators with unfavorably strong f_{CE} drift. The measurement presented in Fig. 4.3(d) serves as a crosscheck, demonstrating that the replacement of the in-loop beat signal by an unrelated local oscillator results in the loss of CEP stability.

Due to the fact that the stabilization scheme relies on a fixed AOFS driver frequency, the diffracted out-of-loop beat signal shows the same frequency drift as the in-loop signal. In combination with the inevitable GD of the correction mechanism that has already been discussed in the previous chapter, a variation of f_{CE} causes additional phase noise. Solely at zero delay, i.e., the instant of the electrical gate pulse, the phase is immune against such frequency drift. However, operation at this point would require an instantaneous correction mechanism or some electronic compensation of the phase lag, as discussed in section 3.2.2. It is found that the longer the GD of the correction mechanism is, the stronger drifts of the f_{CE} transfer into CEP noise, see also Eq. (3.2.1).

This contribution to the overall phase noise can now be identified in the measurements depicted in Fig. 4.3(a-c). To this end, the slip of the CEP within the individual segments $\varphi_{\mathrm{CE}}^{(k)}(\Delta t)$ is retrieved via the Takeda algorithm [128]. From this data the CEP jitter $\delta\varphi_{\mathrm{CE}}$ can be plotted as a function of the GD, as it is shown in Fig. 4.3(e) based on the measurement from Fig. 4.3(b). The plot clearly reveals a linearly increasing phase jitter, which is extrapolated to zero delay. This way the overall phase jitter is decomposed into two contributions: On the one hand, there is the noise contribution at zero delay, which represents the ultimate stabilization performance of the present scheme. This limit is determined by detection noise and is found to be $\delta\varphi_0 \approx 50\,\mathrm{mrad}$. On the other hand, the noise of the beat signal f_{CE} induces a linearly increasing component, which according to Eq. (3.2.1) is given by $2\pi\delta f_{\mathrm{CE}}\Delta t$.

These findings highlight again that it is important for a practical application of the present stabilization scheme to reduce the delay in the correction mechanism to the extent possible. In the present proof-of-concept experiment the GD is mainly caused by the used narrowband SAW filter, which was employed to facilitate the out-of-loop CEP detection by the generation of rather long acoustic transients. These long transients, however, are not necessary in real-life applications, where

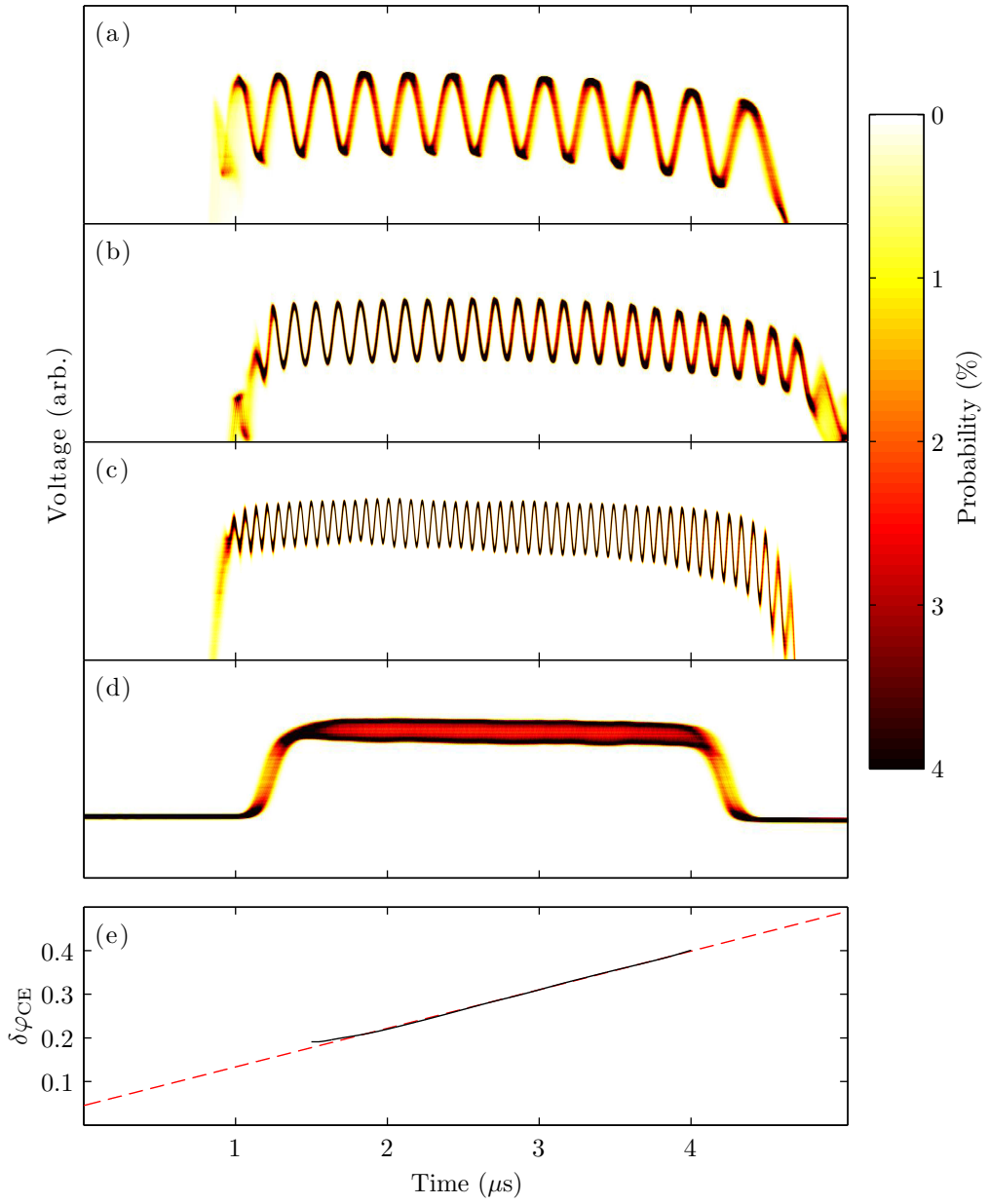

Figure 4.3: (a-d) Histogram plots of 18,462 out-of-loop transients measured at $f_{amp} = 5.2$ kHz for different beat frequencies. Histogram information is encoded in the color scale. Measured beat frequencies: (a) $f_{CE,OOL} = 3.3\,MHz$, (b) $6.7\,MHz$, (c) $13.5\,MHz$, and (d) $11.7\,MHz$. In (d) the in-loop beat signal was replaced by an unrelated local oscillator. (e) rms phase jitter vs. delay as measured in (b). Dashed line: linear fit to measured data.

the diffracted output is used to seed an amplifier. In the standard configuration the total GD of the commercial CEP stabilization module (CEP4, Femtolasers) is only 400 ns, which already converts into < 100 mrad residual phase jitter for the measurement in Fig 4.3(e). Such noise levels compare rather favorably to other kilohertz CEP detection schemes [78].

To further analyze the different noise contributions in the new stabilization scheme, both noise contributions are separated in the retrieved phase data of every individual recorded time segment as

$$\varphi_{\mathrm{CE}}^{(k)}(\Delta t) = \varphi_0^{(k)} + 2\pi f_{\mathrm{CE}}^{(k)} \Delta t,\ k = 1 \ldots 18,462, \tag{4.1.4}$$

where $\varphi_0^{(k)}$ and $f_{\mathrm{CE}}^{(k)}$ are determined from linear regression. The temporal evolution of the CEP at a specific group delay ($\Delta t = 2\,\mu$s) of all segments is plotted in Fig. 4.4(a), where the mean phase has been subtracted (black trace). The phase variations due to deviations from the mean beat frequency are plotted for comparison (red trace) in accordance with the second term in Eq. (4.1.4). It is found that both traces exhibit very similar features and show the same trend, which is indicative of a strong correlation and leads to the conclusion that frequency drift is a dominant noise source.

For further insight, a Fourier analysis of the different noise contributions was performed. The phase noise density depicted in Fig. 4.4(b) indicates a near-perfect agreement between the total phase noise and the frequency-drift-induced phase noise below 20 Hz, corroborating strong correlation on this time scale. At higher frequencies, however, the noise densities exhibit a nearly constant noise floor, which is determined by the detection limit of the present measurement scheme ($\sim 2 \times 10^{-3}\,\mathrm{rad}/\sqrt{\mathrm{Hz}}$). The noise floor is only interrupted by a broad noise band in the acoustic region at a few 100 Hz and by a rather narrow noise band centered around 20 Hz that was found to be induced by the laboratory air conditioning system. These features show up as small steps in the integrated phase noise, plotted in Fig. 4.4(c). Reducing the impact of such noise features, e.g. by replacing the fiber-based out-of-loop f-$2f$ interferometer by a less noise susceptible second 0-f interferometer, could help to minimize the measured overall phase jitter, which was determined to be 190 mrad at this specific group delay ($\Delta t = 2\,\mu$s). Given that the phase jitter accumulated from the f_{CE} noise already amounts to ~ 120 mrad clearly opens a path towards sub-100 mrad overall CEP jitters, provided that the total GD is reduced in further experiments.

Alternatively, the concept of the acoustic frequency comb can also be combined with one of the techniques presented in section 3.2.2 to compensate the effect of the GD either by electronic or optical means. Finally, the noise due to the non-instantaneous correction mechanism is also prevented if the beat signal is stabilized with an additional feedback loop, which, however, removes the advantage of leaving the oscillator untouched.

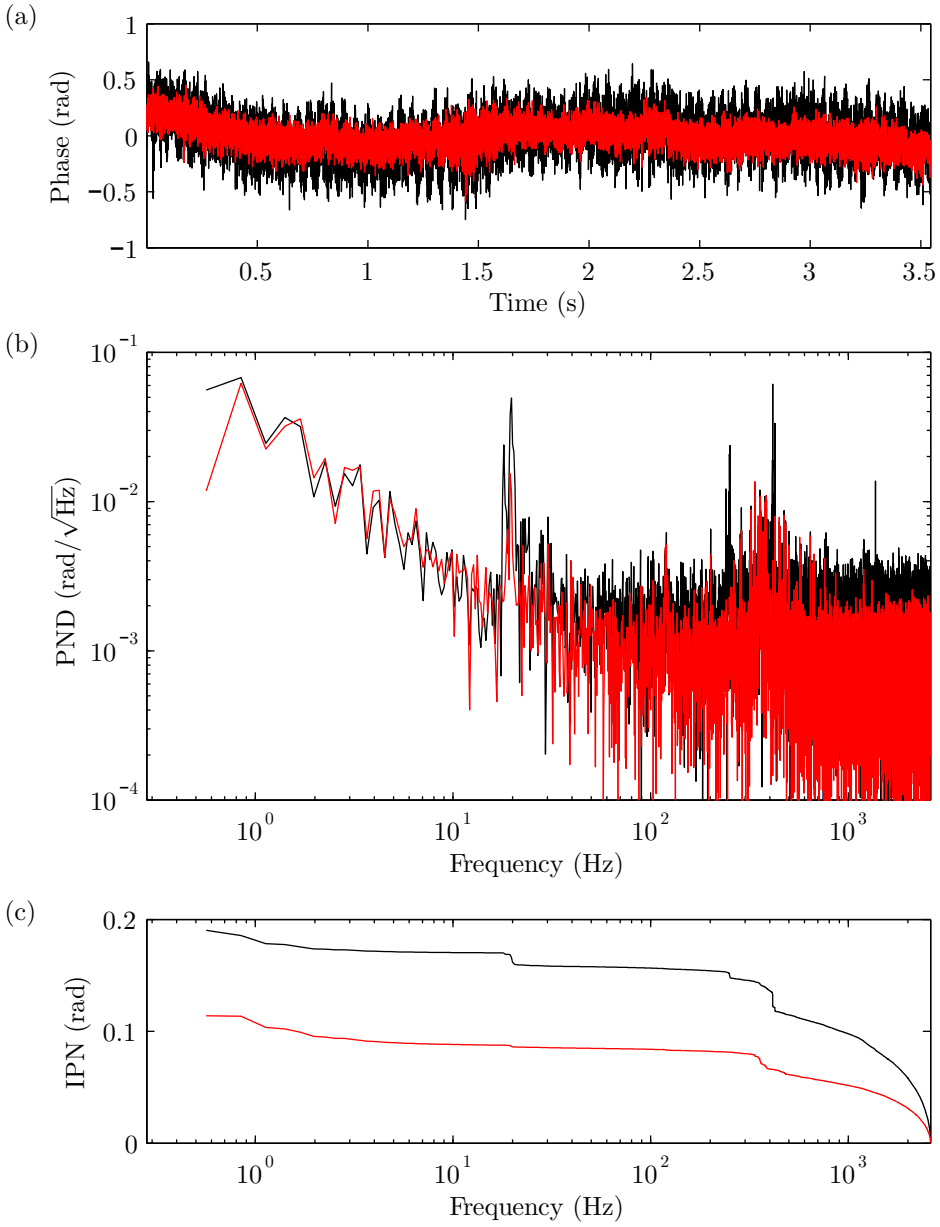

Figure 4.4: Phase noise analysis at the GD $\Delta t = 2\,\mu$s for an acquisition rate $f_{\mathrm{amp}} = 5.2\,$kHz. Black traces: total measured phase noise; red traces: noise induced by f_{CE} drift. (a) Temporal phase evolution over 18,462 segments. (b) Single-sided phase noise density. (c) Integrated phase noise vs. frequency.

In order to prove the versatility of the new concept, it is demonstrated that the pulsed stabilization scheme is applicable to virtually any amplifier repetition rate. To this end, the CEP stabilization was repeated at a rather low repetition rate of $f_{\mathrm{amp}} = 2.5\,\mathrm{Hz}$. From a time domain perspective the only difference to higher repetition rates is that the in-loop beat signal is gated by the electrical pulses less frequently. As a positive side-effect, the overall acquisition time for a single measurement could be extended to several hours. Figure 4.5 shows the analysis in the same fashion as before for a CEP stabilization measurement of 60 minutes. The ten minute data subset that is is depicted in Fig. 4.5(b) reveals again the strong correlation of the two noise traces. The overall integrated phase noise at the GD $\Delta t = 2\,\mu\mathrm{s}$ is 370 mrad, where the noise from f_{CE} drift alone amounts to 300 mrad. These results illustrate that sub-100 mrad phase jitters are also within reach for the long-term operation of low-repetition amplifier systems. Similar results have been achieved for repetition rates in the sub-Hz regime.

Outlook

It should be noted that apart from the above discussed straightforward measures to optimize the stabilization performance of the acoustic frequency comb concept, the CEP stabilization can in principle be performed in the same fashion with a collinear acousto-optic device (Dazzler), which is used in many commercial CPA systems as a programmable acousto-optical dispersive filter [136]. The working principle of this device is very similar to the presented pulsed scheme, as it also generates short acoustical transients that directly influence the optical phases of the diffracted pulses. By adapting the demonstrated signal synthesis scheme to the Dazzler hardware, an AOFS is no longer required to implement a CEP stabilization in such a system, which reduces the complexity and the costs of the optical setup. Furthermore, due to the feed-forward character of the proposed stabilization scheme, no interference is expected if the Dazzler is used simultaneously for a slow feedback loop to compensate residual phase jitter behind the amplifier. Such detrimental effects can occur when two feedback loops act on the same control parameter.

Another promising prospect is that the presented pulsed CEP detection scheme provides the unique possibility to identify the CEP noise contributions that are introduced by the amplification process itself if the detection scheme is combined with conventional CEP detection after the amplifier [77, 81]. The methods revealed in this section may therefore help to improve the understanding of the underlying physical limiting mechanisms for the CEP stabilization of amplifier systems.

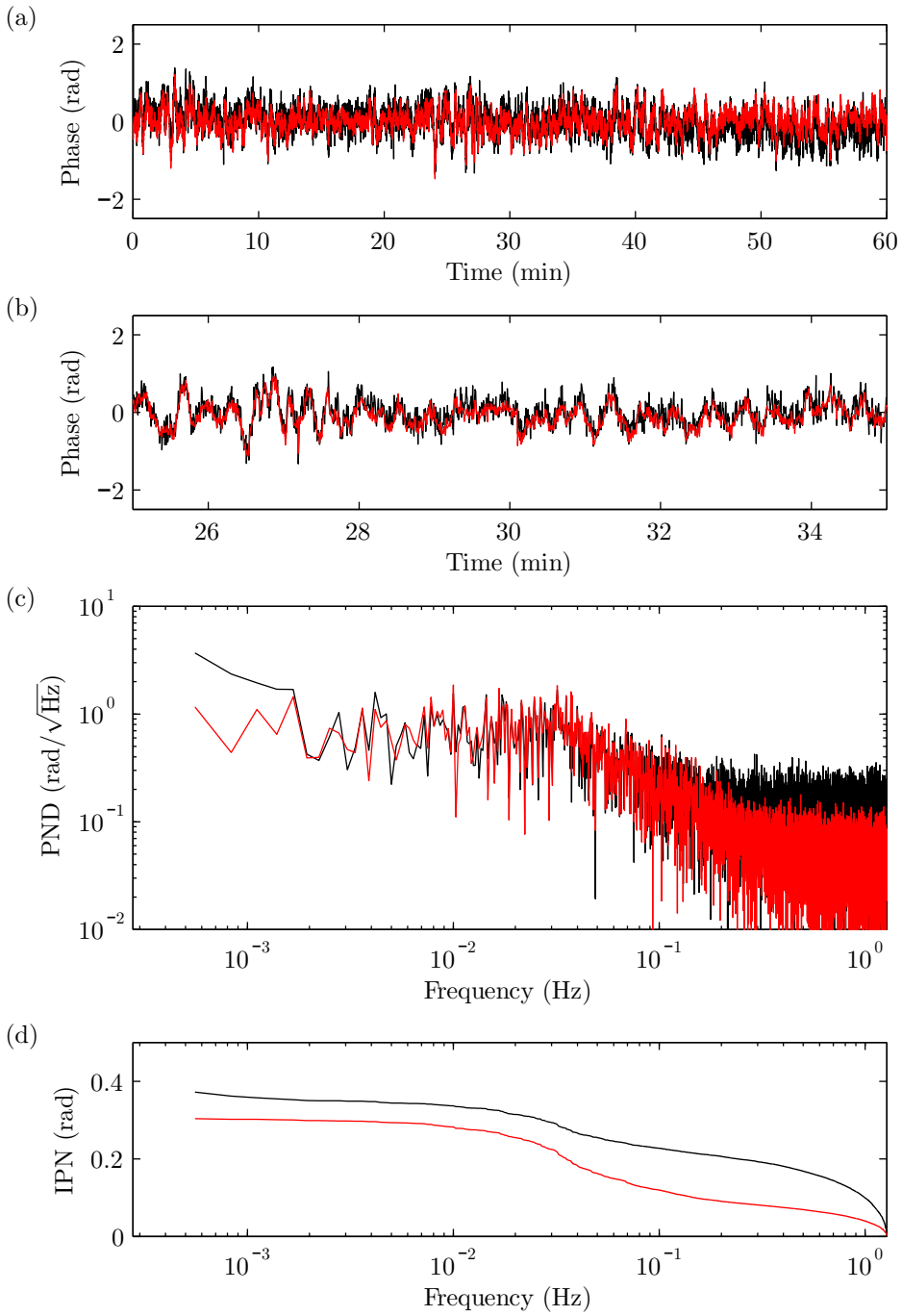

Figure 4.5: Phase noise analysis at the GD $\Delta t = 2\,\mu$s for an acquisition rate $f_{\mathrm{amp}} = 2.5\,$Hz. Black traces: total measured phase noise; red traces: noise induced by f_{CE} drift. (a) Temporal phase evolution over 9,158 segments. (b) 10 min subset of the phase evolution. (c) Single-sided phase noise density. (d) Integrated phase noise vs. frequency.

4.2 Shot Noise Limitations in Spectral Interferometry

As has been discussed in the previous chapter about oscillator CEP stabilization, the optical shot noise represents a fundamental barrier for the precision of the CEP detection, which exists even for a hypothetical laser that is free of any technical amplitude noise. Next to this inevitable consequence of the statistical properties of light, there are more limitations due to the electro-optic conversion in the light detector, which are most dominant under extreme low light conditions. In order to quantify the impact of these limiting constraints on the amplifier CEP stabilization, the CEP measurement via spectral interferometry is numerically investigated in section 4.2.1. Minimizing such effects by an optimization of the supercontinuum generation process is then subject of section 4.2.2.

Under the impression of the discussion about the light level dependence of the oscillator stabilization, it appears puzzling at first sight that shot noise can play a role in CEP stabilization of amplified laser pulses. CEP detection on a shot-to-shot basis should be readily feasible, as these laser sources typically provide pulse energies on the order of 1 mJ, which translate into photon numbers of about 10^{16}. Nevertheless, most of the different variants of CEP detection schemes that have been proposed [76–78] suffer from the same bottleneck as oscillator CEP detection, i.e., the efficiency of the supercontinuum generation. Given that the spectral broadening is mostly done in solid materials [97, 144], only a rather small fraction of the total pulse energy, about 100 nJ, can be effectively used as the critical power sets an upper limit before multifilamentary break up and crystal damage [145] will occur, see Eq. (2.4.14). The subsequent nonlinear conversion of a narrow wavelength interval at the spectral edge further reduces the number of photons typically to some 10^4, which is only about one order of magnitude more than in optimized oscillator scenarios. The difference to those rf heterodyning techniques, however, is that the spectral fringe pattern is detected with a pixel-based detector at the output of a spectrometer at a much lower repetition rate.

4.2.1 Numerical Simulation of CEP Detection Noise

In order to systematically investigate the different contributions to the CEP detection noise, the impact on the phase retrieval is first confined to the effect of pure optical shot noise, before the simulations are extended to typical detector noise levels of a one dimensional CCD sensor.

The numerical simulation of the CEP measurement with a spectral interference pattern is based on the amplitude-modulated time series Eq. (3.1.2) that has already been used for the simulation of RF heterodyning, with the only difference being that each element $N(k)$, $k \in \mathbb{N}$ now represents the number of photons that fall on one individual detector-pixel at the output plane of a spectrometer. For simplicity a perfect fringe contrast was assumed, corresponding to balanced light levels of the interfering spectral components. After adding Poissonian noise with the spread $\sqrt{N(k)}$ to the interference pattern, the next step is the read-out of the

fringe position, which enables the CEP retrieval except for the unknown interferometer phase.

Under experimental conditions, the phase extraction is usually done by FFT-based algorithms, which, however, require a fast data processing environment to minimize the latency of the phase retrieval, especially if an error signal is needed for an additional feedback loop. In fact, it is very challenging to perform the digital phase retrieval in real-time on a shot-to-shot basis at multi-kHz repetition rates, which is why analog signal processing schemes have been developed [78]. The digital phase extraction, though, can be made far more efficient, if only the phase of the Fourier component at the previously determined fringe period is calculated, which has been used in the presented numerical simulations.

To this end, the fringe pattern is spatially integrated after numerically mixing it with a reference signal at the desired fringe period, similar to lock-in detection in the time domain. This procedure is applied, both, with a sine and cosine reference signal

$$X = \sum_k N(k)\cos(2\pi f_k k); \quad Y = \sum_k N(k)\sin(2\pi f_k k), \tag{4.2.1}$$

where f_k is the spatial fringe frequency. The angle in the plane of these two orthogonal coordinates $\varphi = \tan^{-1}(Y/X)$ then yields the phase of the fringe pattern. The described phase detection is then repeated a thousand times in order to get statistical results on the shot-to-shot phase jitter.

The numerical calculations show that in the presence of pure shot noise the determined phase jitter is independent from the number of pixels L that are used for the detection. In fact, it is solely the total number of detected photons $N_{\mathrm{tot}} = \langle N \rangle \cdot L$ that determines the shot noise induced phase jitter. The numerical results are illustrated as black squares in Fig. 4.6. Given that a hundredfold phase jitter reduction from $\sim$100 mrad to $\sim$1 mrad is observed if the number of photons is increased by four orders of magnitude from one hundred to one million, one finds the characteristic $1/\sqrt{N_{\mathrm{tot}}}$ noise scaling that is expected for pure optical shot noise. Averaging over multiple pulses by increasing the integration time of the detector can simply be interpreted as a higher total number of photons, which leads to an accordingly lower shot noise induced phase jitter. Under practical conditions, though, one has to be aware that it is generally impossible to unveil the true shot-to-shot phase jitter from an averaged measurement, as the spectral distribution of noise can be very different in the presence of technical noise.

While the number of detector pixels could be neglected for the case of pure optical shot noise, it does play a role if the noise from the detector is considered. It is assumed in the following that the detection of the spectral fringe pattern in the relevant narrow wavelength interval is performed with one hundred pixels ($L = 100$) of a one dimensional CCD sensor. Under low light conditions the detection noise of an individual CCD pixel consists of the previously discussed optical shot noise, the electrical noise of the dark current and the so called read-out noise. While the

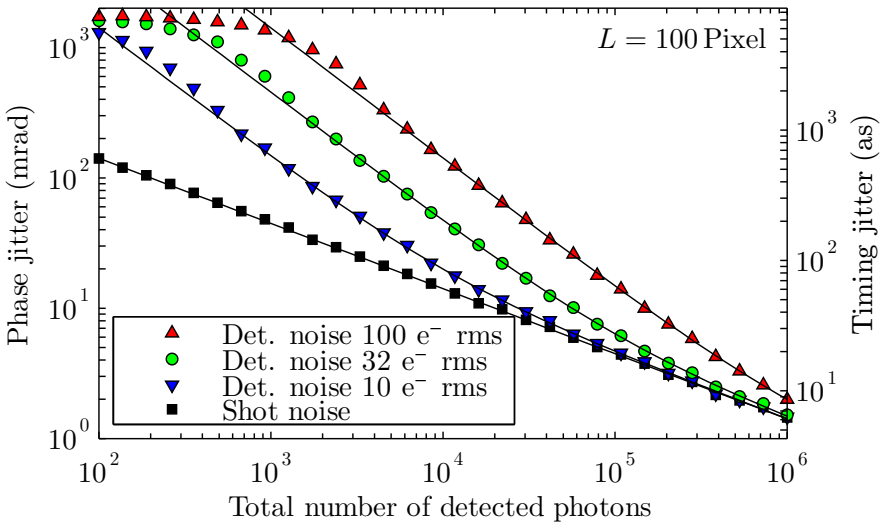

Figure 4.6: Numerically simulated detection noise induced phase jitter in a spectral interferometry detection scheme. Simulations include pure optical shot noise (black squares) as well as different levels of CCD-pixel read-out noise (colored symbols). Total number of incident photons refers to the sum over $L = 100$ pixels.

latter is caused by thermal noise in the electrical read-out circuits and the output amplifiers, dark noise is governed by the same physical characteristics as optical shot noise, but is determined by the number of electrons that are generated in the dark state when no light falls on the detector. In contrast to the optical shot noise, the strength of both noise sources is independent from the illumination. In fact, the only way to lessen the corruption by dark noise is a reduction of the dark current itself, which can be achieved via cooling of the detector. By doing so, the dark noise can be minimized below the level of the read-out noise, which thus represents the ultimate noise limit of a CCD sensor. Evaluating the specifications of fast (kHz acquisition) one dimensional CCD sensors that are designed for spectroscopic applications, one finds that typical read-out noise figures are on the order of some ten electrons (rms) per pixel and frame. Due to the very high quantum efficiencies of modern CCD sensors in the visible region, which can be as high as 90%, the absolute noise figures given in electron numbers are directly comparable to those given in photon numbers.

In the numerical calculations different detector noise levels between 10 and 100 electrons/photons (rms) have been added to the optical shot noise to monitor the resulting phase jitter scaling for different grades of detector noise corruption, which is shown by the colored data sets in Fig. 4.6. The outcome for the considered situation of one hundred illuminated CCD-pixels is that in the region of 10^6 photons, all the considered read-out noise levels are negligible, whereas the spread of the individual cases becomes significant at some 10^4 photons. In practice, these are typical light levels that are observed when supercontinuum generation in solid materials is applied. In this region it is mandatory to limit the rms read-out noise to ~ 10 electrons, in order to achieve a nearly shot-noise limited detection process. Otherwise the detection process itself can easily give rise to $\sim 100\,\mathrm{mrad}$ of phase jitter. For even lower light levels, the overall detection noise is strongly dominated by the read-out noise and eventually the high phase jitters are indicative of a random phase, rendering the phase retrieval virtually impossible.

Besides the optimization of the available photon numbers, which will be thoroughly discussed in the next section, the impact of the detection process on the phase jitter can only be minimized by using cooled and therefore less noisy CCD sensors, or by confining the same amount of light onto a lower number of pixels. The most extreme realization of the latter approach was reported in [78], where one spectral fringe was mapped onto two separate photo multipliers. These detectors, however, suffer from a lower quantum efficiency than optimized back-thinned CCDs, which is at best on the order of 40% in the short-wavelength visible region.

4.2.2 Optimization of Spectral Interferometry

The discussion on the light level dependence of the detection noise induced phase jitter has revealed that the CEP detection can be strongly corrupted even at amplifier pulse energies. For this reason, the optimization of the supercontinuum generation process as well as the subsequent nonlinear frequency conversion are

investigated in the following. Since there are many different materials that can be applied for both processes, the following calculations are supposed to provide some orientation on which materials are best suited to perform these tasks. At first, the optimal SHG crystal for an f-$2f$ interferometer is identified, whereupon the finding is used to calculate the photon yield of the frequency doubled light that can be expected from supercontinua generated in various solid and gaseous materials.

Comparison of SHG crystal performance for f-$2f$ interferometry

Based on the expression for the filament-based spectral broadening, Eq. (2.4.17), it is found that for a typical Ti:sapphire center wavelength the asymmetric spectral broadening gives rise to an octave-spanning spectrum spanning from 550 to 1100 nm. While this basic analytical model is derived under the assumption of a constant pulse shape, Yang and Shen [96] show that the broadening is even more pronounced on the anti-Stokes side if self-steepening is taken into account. For a Ti:sapphire system, the subsequent frequency doubling in an f-$2f$ interferometer is thus typically done at 1060 nm or at even shorter wavelengths. A more detailed simulation of the filament-based spectral broadening requires sophisticated modeling [146], which, however, is beyond the scope of the present considerations.

For the phase-matching of the nonlinear crystal, one can choose between critical and non-critical phase matching as well as quasi-phase-matching (QPM). Certainly, the most widely-used crystal for the present application is beta barium borate (BBO) that is critically phase-matchable at room temperature for 1060 nm [147]. Non-critical phase matching at this wavelength can be achieved with lithium triborate (LBO) at 427 K, and finally quasi-phase matching is done with a periodically poled magnesium-oxide-doped lithium niobate crystals (MgO:PPLN [148]) having a poling period of 6 μm and which is operated at 450 K.

In order to identify which one of these SHG crystals performs best at this specific wavelength, the SNLO software package[1] [149] was employed to calculate the output energy of the second harmonic. An LBO crystal of 10 mm length, supporting a phase-matching bandwidth of 3.8 nm at 1060 nm, serves as a reference in the following [78]. Due to the different acceptance bandwidth per unit length $\Delta\lambda$, the lengths l of the other crystals were chosen accordingly to support the same bandwidth, thus ensuring the comparability of the results. These values are listed in Table 4.1 together with the respective nonlinear conversion efficiencies d_{eff} and the normalized pulse energies of the second harmonic generation E_{SHG} provided by the SNLO software. For the calculations an input pulse energy of 10 pJ and a Fourier-limited pulse duration of 430 fs were assumed. Furthermore, the different crystal sizes made it necessary to thoroughly optimize the focusing geometry for each crystal, starting from a geometry with the focus at the center of the crystal.

Table 4.1 shows that LBO is the crystal with the highest acceptance bandwidth

[1] SNLO nonlinear optics code available from A. V. Smith, AS-Photonics, Albuquerque, NM, (http://www.asphotonics.com/snlo).

Crystal	$\Delta\lambda$ (nm/cm)	l (mm)	d_{eff} (pm/V)	E_{SHG}
LBO @ 427.2 K	3.8	10	0.85	1
BBO @ 293 K	1.9	5.0	2.01	0.49
PPLN @ 450 K	0.2	0.45	16.0	7.7

Table 4.1: Normalized energy of second harmonic radiation generated by crystals employing different phase-matching techniques, plus an overview of the crystal parameters entering the calculation with the SNLO package. All crystals support the same phase-matching bandwidth of 3.8 nm centered at 1060 nm.

per length, while it has the lowest conversion efficiency. In comparison, BBO has only half the acceptance bandwidth but exhibits a more than two times higher conversion efficiency. What renders BBO unfavorable,though, is the spatial walk-off of 56 mrad between the fundamental and second harmonic, which leads to a more than 50% lower energy output compared to LBO. The MgO:PPLN crystal has by far the highest conversion efficiency, almost 20 times higher than LBO, while the opposite is the case for the acceptance bandwidth. Because of the latter MgO:PPLN crystals as tiny as 0.4 mm have to be used to support the same bandwidth, and very hard focusing is necessary to obtain the maximum efficiency. Theoretically, the efficiency can be several times higher than that of LBO, but practically the intensities under these circumstances would greatly exceed the damage threshold of the MgO:PPLN crystals, given that the entire supercontinuum, containing several orders of magnitude more energy, is propagating along the radiation in the phase-matching interval. A potential work-around to this problem could be to filter the spectral content around 1060 nm to reduce the irradiance and to use a non-collinear interferometer topology to reestablish the spatial overlap with the fundamental radiation at 530 nm. This measure, however, would increase the complexity of the setup and make the benefit from using QPM instead of non-critical phase-matching questionable. For this reason, the logical choice for the most viable way of SHG is a non-critical phase matched LBO crystal.

Optimization of supercontinuum generation

After having identified LBO as the most practical SHG crystal, the SNLO software package will be used again in the following to calculate the number of photons that are available for CEP detection after spectral broadening in different materials and subsequent SHG in a 10 mm LBO crystal. These results will help to decide which material is best suited for supercontinuum generation at which available pulse energy and moreover provide an estimate on the resulting detection noise induced phase jitter.

Material	n_0	n_2 (m^2/W)	E_{SC} (J)	ϵ_{SHG}	N
LiF	1.39	9.0e-21	3.1e-7	4.0e-3	3.3e+5
SiO_2	1.47	2.1e-20	1.2e-7	1.5e-3	5.0e+4
Al_2O_3	1.8	2.9e-20	7.4e-8	9.5e-4	1.9e+4
Ar (1 bar)	≈ 1	1.0e-23	3.8e-4	0.69	7.0e+10
Xe (2 bar)	≈ 1	1.2e-22	3.2e-5	0.27	2.3e+9

Table 4.2: Number of photons available for CEP detection based on supercontinuum generation of a 40 fs pulse in a selection of solid and gaseous media and subsequent SHG in a 10 mm LBO crystal.

As it has been discussed above, the critical power P_{crit}, see Eq. (2.4.14), sets an upper limit for the pulse energy that can be used for spectral broadening. Assuming a modest pulse duration of 40 fs, one yields the pulsed energy E_{SC} that is contained in a filament at $P \approx P_{crit}$. These energy levels can be found in Table 4.2 for a selection of crystalline and gaseous media. The efficiency of the supercontinuum generation ϵ_{SC} is given by the ratio of the energy contained in the phase-matching bandwidth and the total energy E_{SC}. This efficiency is estimated to be on the order of 10^{-4} in fair agreement with experimentally measured supercontinua [97]. The energy that is available for the frequency doubling is then given by $E_{SC}\epsilon_{SC}$, serving as the input pulse energy for the SNLO software. After optimization of the focusing geometry for each case, the number of converted photons that are available for CEP detection reads $N = E_{SC}\epsilon_{SC}\epsilon_{SHG}/\hbar\omega$, where ϵ_{SHG} is the determined efficiency of the frequency doubling. The results for the different media are listed in Table 4.2.

The energy levels of the filaments in solid materials, which are on the order of 100 nJ allow for SHG efficiencies of several 10^{-3}, leading to light levels ranging from 10^4 up to some 10^5 photons. Given that a lot of assumptions entered the equation, the calculated 19,000 photons for sapphire (Al_2O_3) agree fairly well with the experimentally measured 32,000 photons reported in [78]. However, it has to be straightened out that these numbers are not directly comparable, as the latter number includes both fundamental and frequency doubled photons. Generally, it is found that a lower linear and nonlinear index of refraction leads to higher photon numbers in the generated f-2f output signal. For a given input peak power $\hat{P} \approx E_{SC}/\tau$, the following simple relationship (solid line in Fig. 4.7) can be used to estimate the nonlinear index of refraction

$$n_2 = 7.4 \times 10^{-10}\mathrm{cm}^2/\hat{P} \tag{4.2.2}$$

that leads to octave broadening with the highest possible number of photons. As indicated in Fig. 4.7 it is often difficult to fulfill Eq. (4.2.2) with available materials. Most oscillators only deliver a few nanojoules of pulse energy, which requires using materials with extremely high n_2, such as $LiNBO_3$ or KTP [139] for efficient

spectral broadening in a bulk material. Exploiting the highly efficient soliton fission mechanism in the fiber geometry is the only viable alternative for oscillators [150]. More importantly, there is a pronounced gap of convenient materials in the range from 0.2 to 30 μJ, which can only be circumvented by high-pressure gas cells [151, 152] or by the use of liquefied gases. Finally, using sapphire or other solid dielectric materials as the broadening medium does not appear to be the optimal choice for kHz amplifier systems. Significantly higher S/N appear to be in reach if suitable media in the gap region of Fig. 4.7 can be found. Such media should readily enable single-shot CEP detection schemes with residual phase jitters of a few 10 mrad or even below.

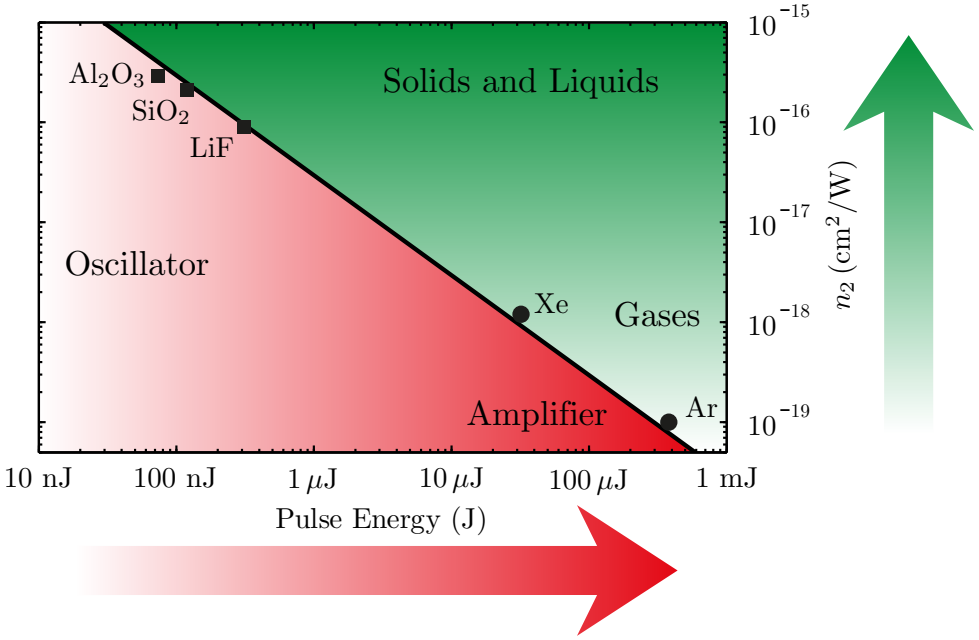

Figure 4.7: Ideal nonlinear refractive index n_2 to obtain octave-spanning supercontinuum generation for a given input pulse energy E_{SC} and a $\tau = 40$ fs pulse duration. Black circles and squares correspond to the gaseous and solid media from Table 4.2, respectively. The solid line represents a fit according to Eq. (4.2.2).

If the SHG step is factored in one observes that, at low SHG efficiencies, the photon number N scales simply as $(1/n_0 n_2)^2$. For gaseous media, however, the efficiencies are already so high that depletion becomes important and that the scaling behavior starts to deviate. In conclusion, one gets a similar result, as it was derived in section 3.1.2 for oscillators, that a lower nonlinearity yields a better S/N and therefore less shot noise-induced phase jitter. On the other hand, this improved immunity against shot noise comes at the price of a lower output power,

as all the energy that is used for CEP detection is lost for the actual application. Therefore the decision about which material is best suited depends on how much pulse energy can be spared for CEP control.

Considering only crystalline materials for the spectral broadening process, the calculations show that LiF is the best choice [97], theoretically allowing for photon levels that lead to phase jitters in the single mrad region. Of course, in practice, real phase jitters will be somewhat higher, simply due to non-ideal frequency doubling conditions, losses in the optical setup and due to a limited detection efficiency. The photon levels for supercontinuum generation in noble gases are several orders of magnitude higher, making the issue of shot noise in CEP detection negligible. However, for typical amplifier systems that deliver on the order of 1 mJ pulse energy, it is not favorable to spare almost 40% of this energy for CEP detection, e.g., as required in argon. In this case the best compromise is xenon, the noble gas with the highest nonlinearity, at a high pressure, so that only a few percent of the pulse energy have to be used, while shot noise still plays a negligible role.

However, apart from the considerations on the achievable light levels, one also has to take into account that broadening in bulk materials typically provides more stable output spectra than filamentation in gases, which is suffering from fluctuations due to gas dynamics. In fact, recent publications on femtosecond filamentation [153–155] give experimental and theoretical evidence for extremely long-lasting hydrodynamical and thermal effects that even play a role at rather low sub-kHz repetition rates.

In conclusion, the discussion of the supercontinuum generation process of amplified laser pulses shows which materials can be employed to achieve the highest possible light levels in the interferometer detection front-end. Furthermore, a very useful outcome of the analysis is the estimate of how much pulse energy is necessary to realize the CEP detection for a given material. Based on the available pulse energy for a given laser system, these results should allow making a decision about the most practical supercontinuum generation media. Even though the list of considered materials is not exhaustive, it does provide an idea of the required crystal properties, in particular the desired nonlinear refractive index. It was shown by the previous discussion of the CEP detection process that any material giving rise to photon numbers of some 10^5 to 10^6 is capable of pushing the impact of detection noise to a negligible level. Having identified several materials that deliver such high photon numbers implies that the fundamental limitation of detection noise can indeed be overcome, leaving room for further optimization of the CEP stabilization process mainly on the side of technical noise sources.

Chapter 5

Conclusions and Outlook

In the present thesis, the most limiting aspects of carrier-envelope phase stabilization were identified. It was found that the restrictions stem from both the CEP detection process, as well as from the control mechanism used to correct the measured phase deviations. Various measures to lessen the impact of the different noise sources were presented, addressing the stabilization of oscillator and amplifier laser systems alike. These improvements resulted in unprecedentedly high stabilization performance and improved usability for applications in frequency metrology and attosecond science.

In the first part of the thesis, limitations in CEP stabilization of oscillator pulse trains were discussed. It was shown that all the steps of the CEP detection process are corrupted by noise, including the required spectral broadening, the beat signal generation by RF-heterodyning techniques, and the electro-optic conversion at the light detector. In order to reduce the impact of the various technical noise sources on the phase detection at the interferometer, different interferometer topologies were discussed. For the experiments presented in this thesis, either a monolithic true common-path interferometer or a novel quasi-common-path interferometer design was used, both of which are particularly insensitive to external technical noise.

Besides these practical considerations, the noise stemming from the light detection was found to represent a more fundamental limitation of the CEP measurement. Depending on the detected light fluence, the noise is either dominated by optical shot noise or by noise stemming from the light detector itself. The series of numerical calculations presented in this thesis provides an estimate of the light levels necessary to achieve a certain beat signal-to-noise-ratio, and for the first time quantifies the impact of the detection noise on the residual phase jitter.

Given that some CEP detection schemes are mostly limited by the shot noise induced detection noise floor, the demonstrated improvement of the beat signal-to-noise-ratio by 20 dB to an overall beat visibility of 60 dB in a 100 kHz resolution bandwidth constitutes a major breakthrough in terms of detection sensitivity. This

progress was enabled by an optimization of the supercontinuum generation process. The experimental results confirmed the numerical simulation of the soliton fission based broadening process in a photonic crystal fiber, which indicates that rather short fibers of only several millimeters in length provide an ideal spectral distribution for the use with an f-$2f$ interferometer.

In combination with a novel double stabilization scheme, the improved CEP detection setup led to a new record-low residual phase jitter of only 20 mrad, translating into a timing jitter of the carrier with respect to the envelope of only 8 attoseconds. This outstanding stabilization performance has become possible by removing the remaining shortcomings of the feed-forward type CEP stabilization by the introduction of an additional classic feedback stabilization. This measure helped to prevent issues arising from a drifting carrier-envelope frequency in a shifter-based stabilization, such as beam-pointing variations and phase drifts in the stabilized output.

Despite the achievements of this double stabilization setup, the scheme still does not present the ultimate solution for CEP control, since it requires back action to the laser oscillator, which is accompanied by cross-talk to other laser parameters. To this end, several promising alternative stabilization techniques were proposed, all of which address the issues of the feed-forward stabilization without the necessity for feedback into the laser.

One of these new schemes is specifically designed to seed a subsequent amplifier, as it only generates CEP stabilized pulses at the reduced amplifier repetition rate. In this novel concept, referred to as the acoustic frequency comb, the synthesis of transient control signals allows for the operation of the frequency shifter in a pulsed mode, which has several technical advantages. The proof-of-concept experiments demonstrated the immunity against drifts of the carrier-envelope frequency, and the results clearly indicate the potential for sub-100 mrad CEP jitters of amplifiers at virtually any repetition rate. Furthermore, by comparing the CEP stability before and after the amplification process, the novel concept can help to improve the understanding of the underlying physical limiting mechanisms for the stabilization of amplifier systems.

In the last part of this thesis, it was shown that the noise from the light detection can be a limiting factor for CEP stabilization, even for intense, amplified laser pulses. Numerical calculations of the light levels present in a spectral f-$2f$ interferometer and computation of the resulting detection noise induced phase jitters helped to identify the materials that are best suited to minimize the noise corruption of the CEP detection process.

In summary, the analysis of the most limiting aspects of carrier-envelope phase stabilization led to the introduction of new concepts providing not only cutting-edge CEP stabilization performance, but also exceptional long-term stability, thus enabling experiments in frequency metrology and attosecond science that were previously considered impossible.

List of Acronyms

AM amplitude modulation

AOFS acousto-optical frequency shifter

AOM acousto-optical modulator

APD avalanche photodiode

ATI above-threshold ionization

CEF carrier-envelope frequency

CEP carrier-enelope phase

CPA chirped-pulse amplification

DFG difference frequency generation

DSO digital sampling oscilloscope

FOM figure of merit

FM frequency modulation

FROG frequency resolved optical gating

FWHM full width at half maximum

FWM four-wave mixing

GD group delay

GDD group delay dispersion

GPO group-phase offset

GVD group-velocity dispersion

KLM Kerr-lens mode-locking

MPA multi-photon absorption

NEP noise-equivalent power

PCF photonic crystal fiber

PLL phase-locked loop

PND phase noise density

QCP quasi-common-path

RBW resolution bandwidth

RF radio frequency

SAM self-amplitude modulation

SA saturable absorber

SAW surface acoustic wave

SHG second harmonic generation

SPIDER spectral phase interferometry for direct electric-field reconstruction

SPM self-phase modulation

SVEA slowly-varying envelope approximation

S/N signal-to-noise ratio

TOD third-order dispersion

TPA two-photon absorption

Publications

Publications Related to this Thesis

1. B. Borchers, S. Koke, A. Husakou, J. Herrmann, and G. Steinmeyer; *Carrier-envelope phase stabilization with sub-10 as residual timing jitter, Opt. Lett.* **36** (2011) 4146-4148.

2. B. Borchers, C. Brée, S. Birkholz, A. Demircan, and G. Steinmeyer; *Saturation of the all-optical Kerr effect in solids, Opt. Lett.* **37** (2012) 1541-1543.

3. P. Jójárt, A. Börzsönyi, B. Borchers, G. Steinmeyer, and K. Osvay; *Agile linear interferometric method for carrier-envelope phase drift measurement, Opt. Lett.* **37** (2012) 836-838.

4. G. Steinmeyer, B. Borchers, and F. Lücking; *Progress in Ultrafast Intense Laser Science IX, Chapter 6: Carrier-Envelope Phase Stabilization, Springer Series in Chemical Physics* **104** (2013).

5. A. von Veltheim, B. Manschwetus, W. Quan, B. Borchers, G. Steinmeyer, H. Rottke, and W. Sandner; *Frustrated Tunnel Ionization of Noble Gas Dimers with Rydberg-Electron Shakeoff by Electron Charge Oscillation, Phys. Rev. Lett.* **110** (2013) 023001.

6. B. Borchers, A. Anderson, and G. Steinmeyer; *On the role of shot noise in carrier-envelope phase stabilization, Laser Photon. Rev.* **8** (2014) 303-315.

7. B. Borchers, F. Lücking, and G. Steinmeyer; *Acoustic frequency combs for carrier-envelope phase stabilization, Opt. Lett.* **39** (2014) 544-547.

8. A. von Veltheim, B. Borchers, G. Steinmeyer, H. Rottke; *Imaging the impulsive alignment of noble gas dimers via Coulomb explosion, Phys. Rev. A* **89** (2014) 023432.

Conference Contributions

Contributions presented by myself are indicated by *.

1. S. Koke, B. Borchers*, C. Grebing, H. Frei, A. Anderson, A. Assion, and G. Steinmeyer; *Sub-Poissonian Noise Signatures in the Carrier-Envelope Phase Jitter of Highly Stabilized Mode-Locked Lasers*; CLEO Europe-EQEC, Munich, 2011.

2. S. Koke, B. Borchers, C. Grebing, H. Frei, A. Anderson, A. Assion, and G. Steinmeyer; *Signatures of sub-Poissonian noise in the carrier-envelope phaser of highly stabilized mode-locked lasers*; CLEO US-QELS, Baltimore, MD, USA, 2011.

3. B. Borchers, C. Grebing, S. Koke, and G. Steinmeyer; *Quantum Non-Demolition Measurements of Light via the Carrier-Envelope Phase of Mode-Locked Lasers*; CLEO US-QELS, Baltimore, MD, USA, 2011.

4. B. Borchers*, C. Brée, and G. Steinmeyer; *Saturation of the all-optical Kerr effect in solids*; DPG Frühjahrstagung, Stuttgart, 2012.

5. B. Borchers*, S. Koke, and G. Steinmeyer; *Carrier-envelope phase double stabilization setup with sub-10 attosecond timing jitter*; (invited) HILAS, Berlin, 2012.

6. B. Borchers*, S.Koke, A. Husakou, J. Herrmann and G. Steinmeyer; *Carrier-envelope phase double stabilization with eight attosecond residual timing jitter*; CLEO, San Jose, CA, USA, 2012.

7. B. Borchers*, S. Birkholz, C. Brée, and G. Steinmeyer; *Saturation of the all-optical Kerr effect in solids*; CLEO, San Jose, CA, USA, 2012.

8. S. K. Das, M. Bock, R. Grunwald, B. Borchers, G. Steinmeyer, D. Ristau, T. Vockerodt, and U. Morgner; *First experimental evidence for a non-instantaneous lifetime of nonlinear optical $\chi^{(3)}$ effects*; CLEO, San Jose, USA, 2012.

9. B. Borchers, M. Mero, and G. Steinmeyer; *Acoustic frequency combs for versatile carrier-envelope phase control*; CLEO Europe-EQEC, Munich, 2013.

10. B. Borchers, M. Mero, and G. Steinmeyer; *Acoustic frequency combs for unconditionally stable long-term carrier-envelope phase stabilization*; CLEO, San Jose, CA, USA, 2013.

11. F. Lücking, B. Borchers*, A. Assion, G. Steinmeyer; *Acoustic frequency comb meets optical frequency comb for carrier-envelope phase stabilization*; HILAS, Berlin, 2014.

12. F. Lücking, B. Borchers, G. Steinmeyer; *Carrier-envelope phase stabilization via acoustic frequency combs*; CLEO, San Jose, CA, USA, 2014.

Awards

1. *Best Student Presentation* at the High-Intensity Sources and High-Field Phenomena (HILAS) Meeting, Berlin, Germany, 2012.

Bibliography

[1] M. DiDomenico, *Small-signal analysis of internal (coupling-type) modulation of lasers*, *J. Appl. Phys.* **35** (1964) 2870–2876.

[2] L. E. Hargrove, R. L. Fork, and M. A. Pollack, *Locking of He-Ne laser modes induced by synchronous intracavity modulation*, *Appl. Phys. Lett.* **5** (1964) 4–5.

[3] R. L. Fork, C. H. Brito Cruz, P. C. Becker, and C. V. Shank, *Compression of optical pulses to six femtoseconds by using cubic phase compensation*, *Opt. Lett.* **12** (1987) 483–485.

[4] A. Yariv and P. Yeh, *Optical waves in crystals*. Wiley, Hoboken, New Jersey, USA, 2nd ed., 1984.

[5] S. Rausch, T. Binhammer, A. Harth, J. Kim, R. Ell, F. X. Kärtner, and U. Morgner, *Controlled waveforms on the single-cycle scale from a femtosecond oscillator*, *Opt. Express* **16** (2008) 9739–9745.

[6] J. A. Cox, W. P. Putnam, A. Sell, A. Leitenstorfer, and F. X. Kärtner, *Pulse synthesis in the single-cycle regime from independent mode-locked lasers using attosecond-precision feedback*, *Opt. Lett.* **37** (2012) 3579–3581.

[7] A. de Bohan, P. Antoine, D. B. Miloševic, and B. Piraux, *Phase-dependent harmonic emission with ultrashort laser pulses*, *Phys. Rev. Lett.* **81** (1998) 1837–1840.

[8] G. Tempea, M. Geissler, and T. Brabec, *Phase sensitivity of high-order harmonic generation with few-cycle laser pulses*, *J. Opt. Soc. Am. B* **16** (1999) 669–673.

[9] E. Goulielmakis, M. Uiberacker, R. Kienberger, A. Baltuska, V. Yakovlev, A. Scrinzi, T. Westerwalbesloh, U. Kleineberg, U. Heinzmann, M. Drescher, and F. Krausz, *Direct measurement of light waves*, *Science* **305** (2004) 1267–1269.

[10] J. N. Eckstein, *High resolution spectroscopy using multiple coherent interactions*. PhD thesis, Stanford University, 1978.

[11] L. Xu, C. Spielmann, A. Poppe, T. Brabec, F. Krausz, and T. W. Hänsch, *Route to phase control of ultrashort light pulses*, *Opt. Lett.* **21** (1996) 2008–2010.

[12] H. R. Telle, G. Steinmeyer, A. E. Dunlop, J. Stenger, D. H. Sutter, and U. Keller, *Carrier-envelope offset phase control: A novel concept for absolute optical frequency measurement and ultrashort pulse generation*, *Appl. Phys. B* **69** (1999) 327–332.

[13] J. Reichert, R. Holzwarth, T. Udem, and T. W. Hänsch, *Measuring the frequency of light with mode-locked lasers*, *Opt. Commun.* **172** (1999) 59 – 68.

[14] D. J. Jones, S. A. Diddams, J. K. Ranka, A. Stentz, R. S. Windeler, J. L. Hall, and S. T. Cundiff, *Carrier-envelope phase control of femtosecond mode-locked lasers and direct optical frequency synthesis*, *Science* **288** (2000) 635–639.

[15] T. Udem, R. Holzwarth, and T. W. Hänsch, *Optical frequency metrology*, *Nature* **416** (2002) 233–237.

[16] S. A. Diddams, D. J. Jones, J. Ye, S. T. Cundiff, J. L. Hall, J. K. Ranka, R. S. Windeler, R. Holzwarth, T. Udem, and T. W. Hänsch, *Direct link between microwave and optical frequencies with a 300 THz femtosecond laser comb*, *Phys. Rev. Lett.* **84** (2000) 5102–5105.

[17] H. Schnatz, B. Lipphardt, J. Helmcke, F. Riehle, and G. Zinner, *First phase-coherent frequency measurement of visible radiation*, *Phys. Rev. Lett.* **76** (1996) 18–21.

[18] T. W. Hänsch, *Nobel lecture: Passion for precision*, *Rev. Mod. Phys.* **78** (2006) 1297.

[19] S. Koke, C. Grebing, H. Frei, A. Anderson, A. Assion, and G. Steinmeyer, *Direct frequency comb synthesis with arbitrary offset and shot-noise-limited phase noise*, *Nature Photon.* **4** (2010) 462–465.

[20] J. C. Maxwell, *On physical lines of force*, *Philosophical Magazine and Journal of Science* **25** (1861) 161.

[21] M. Born and E. Wolf, *Principles of Optics: Electromagnetic Theory of Propagation, Interference and Diffraction of Light*. Cambridge University Press, Cambridge, UK, 7th ed., Oct., 1999.

[22] J.-C. Diels and W. Rudolph, *Ultrashort Laser Pulse Phenomena: Fundamentals, Techniques, and Applications on a Femtosecond Time Scale (Optics and Photonics Series)*. Academic Press, Burlington, MA, USA, 2nd ed., May, 1996.

[23] T. Brabec and F. Krausz, *Nonlinear optical pulse propagation in the single-cycle regime*, *Phys. Rev. Lett.* **78** (1997) 3282–3285.

[24] M. A. Porras, *Propagation of single-cycle pulsed light beams in dispersive media*, *Phys. Rev. A* **60** (1999) 5069–5073.

[25] P. Kinsler and G. H. C. New, *Few-cycle pulse propagation*, *Phys. Rev. A* **67** (2003) 023813.

[26] F. W. Helbing, G. Steinmeyer, J. Stenger, H. R. Telle, and U. Keller, *Carrier-envelope-offset dynamics and stabilization of femtosecond pulses*, *Appl. Phys. B* **74** (2002) 35–42.

[27] G. P. Agrawal, *Nonlinear Fiber Optics*. Academic Press, San Diego, CA, USA, 3rd ed., 2003.

[28] H. A. Kramers, *La diffusion de la lumière par les atomes*, *Atti Cong. Intern. Fisica* **2** (1927) 545–557.

[29] R. de L. Kronig, *On the theory of dispersion of x-rays*, *J. Opt. Soc. Am.* **12** (1926) 547–556.

[30] R. W. Boyd, *Nonlinear Optics*. Academic Press, London, UK, 2nd ed., 2003.

[31] A. E. Siegman, *Lasers*. Univ. Science Books, Sausalito, CA, USA, 1986.

[32] A. J. DeMaria, D. A. Stetser, and H. Heynau, *Self mode-locking of lasers with saturable absorbers*, *Appl. Phys. Lett.* **8** (1966) 174–176.

[33] U. Keller, D. A. B. Miller, G. D. Boyd, T. H. Chiu, J. F. Ferguson, and M. T. Asom, *Solid-state low-loss intracavity saturable absorber for Nd:YLF lasers: an antiresonant semiconductor Fabry-Perot saturable absorber*, *Opt. Lett.* **17** (1992) 505–507.

[34] A. Schmidt, S. Rivier, G. Steinmeyer, J. H. Yim, W. B. Cho, S. Lee, F. Rotermund, M. C. Pujol, X. Mateos, M. Aguiló, F. Díaz, V. Petrov, and U. Griebner, *Passive mode locking of Yb:KLuW using a single-walled carbon nanotube saturable absorber*, *Opt. Lett.* **33** (2008) 729–731.

[35] R. Hellwarth, J. Cherlow, and T.-T. Yang, *Origin and frequency dependence of nonlinear optical susceptibilities of glasses*, *Phys. Rev. B* **11** (1975) 964–967.

[36] V. J. Matsas, T. P. Newson, D. J. Richardson, and D. N. Payne, *Self-starting passively mode-locked fibre ring soliton laser exploiting nonlinear polarisation rotation*, *Electron. Lett.* **28** (1992) 1391–1393.

[37] K. Tamura, H. A. Haus, and E. P. Ippen, *Self-starting additive pulse mode-locked erbium fibre ring laser*, *Electron. Lett.* **28** (1992) 2226–2228.

[38] E. P. Ippen, H. A. Haus, and L. Y. Liu, *Additive pulse mode locking*, *J. Opt. Soc. Am. B* **6** (1989) 1736–1745.

[39] P. N. Kean, X. Zhu, D. W. Crust, R. S. Grant, N. Langford, and W. Sibbett, *Enhanced mode locking of color-center lasers*, *Opt. Lett.* **14** (1989) 39–41.

[40] D. E. Spence, P. N. Kean, and W. Sibbett, *60-fsec pulse generation from a self-mode-locked Ti:sapphire laser*, *Opt. Lett.* **16** (1991) 42–44.

[41] U. Keller, G. W. 'tHooft, W. H. Knox, and J. E. Cunningham, *Femtosecond pulses from a continuously self-starting passively mode-locked Ti:sapphire laser*, *Opt. Lett.* **16** (1991) 1022–1024.

[42] T. Brabec, C. Spielmann, and F. Krausz, *Mode locking in solitary lasers*, *Opt. Lett.* **16** (1991) 1961–1963.

[43] Y. Chen, F. X. Kärtner, U. Morgner, S. H. Cho, H. A. Haus, E. P. Ippen, and J. G. Fujimoto, *Dispersion-managed mode locking*, *J. Opt. Soc. Am. B* **16** (1999) 1999–2004.

[44] R. Szipöcs, C. Spielmann, F. Krausz, and K. Ferencz, *Chirped multilayer coatings for broadband dispersion control in femtosecond lasers*, *Opt. Lett.* **19** (1994) 201–203.

[45] F. W. Helbing, G. Steinmeyer, and U. Keller, *Carrier-envelope offset phase-locking with attosecond timing jitter*, *IEEE J. Sel. Top. Quantum Electron.* **9** (2003) 1030–1040.

[46] T. Udem, J. Reichert, R. Holzwarth, and T. W. Hänsch, *Accurate measurement of large optical frequency differences with a mode-locked laser*, *Opt. Lett.* **24** (1999) 881–883.

[47] S. T. Cundiff and J. Ye, *Colloquium: Femtosecond optical frequency combs*, *Rev. Mod. Phys.* **75** (2003) 325–342.

[48] L. Hollberg, S. Diddams, A. Bartels, T. Fortier, and K. Kim, *The measurement of optical frequencies*, *Metrologia* **42** (2005) 105.

[49] V. Gerginov, C. E. Tanner, S. A. Diddams, A. Bartels, and L. Hollberg, *High-resolution spectroscopy with a femtosecond laser frequency comb*, *Opt. Lett.* **30** (2005) 1734–1736.

[50] M. J. Thorpe, K. D. Moll, R. J. Jones, B. Safdi, and J. Ye, *Broadband cavity ringdown spectroscopy for sensitive and rapid molecular detection*, *Science* **311** (2006) 1595–1599.

[51] S. Schiller, *Spectrometry with frequency combs*, *Opt. Lett.* **27** (2002) 766–768.

[52] C. W. Chou, D. B. Hume, J. C. J. Koelemeij, D. J. Wineland, and T. Rosenband, *Frequency comparison of two high-accuracy Al^+ optical clocks*, *Phys. Rev. Lett.* **104** (2010) 070802.

[53] K. Predehl, G. Grosche, S. M. F. Raupach, S. Droste, O. Terra, J. Alnis, T. Legero, T. W. Hänsch, T. Udem, R. Holzwarth, and H. Schnatz, *A 920-kilometer optical fiber link for frequency metrology at the 19th decimal place*, *Science* **336** (2012) 441–444.

[54] M. Fischer, N. Kolachevsky, M. Zimmermann, R. Holzwarth, T. Udem, T. W. Hänsch, M. Abgrall, J. Grünert, I. Maksimovic, S. Bize, H. Marion, F. P. D. Santos, P. Lemonde, G. Santarelli, P. Laurent, A. Clairon, C. Salomon, M. Haas, U. D. Jentschura, and C. H. Keitel, *New limits on the drift of fundamental constants from laboratory measurements*, *Phys. Rev. Lett.* **92** (2004) 230802.

[55] P. B. Corkum, *Plasma perspective on strong field multiphoton ionization*, *Phys. Rev. Lett.* **71** (1993) 1994–1997.

[56] R. Kienberger, E. Goulielmakis, M. Uiberacker, A. Baltuška, V. Yakovlev, F. Bammer, A. Scrinzi, T. Westerwalbesloh, U. Kleineberg, U. Heinzmann, M. Drescher, and F. Krausz, *Atomic transient recorder*, *Nature* **427** (2004) 817–821.

[57] I. J. Sola, E. Mevel, L. Elouga, E. Constant, V. Strelkov, L. Poletto, P. Villoresi, E. Benedetti, J.-P. Caumes, S. Stagira, C. Vozzi, G. Sansone, and M. Nisoli, *Controlling attosecond electron dynamics by phase-stabilized polarization gating*, *Nature Phys.* **2** (2006) 319–322.

[58] K. Zhao, Q. Zhang, M. Chini, Y. Wu, X. Wang, and Z. Chang, *Tailoring a 67 attosecond pulse through advantageous phase-mismatch*, *Opt. Lett.* **37** (2012) 3891–3893.

[59] E. Goulielmakis, M. Schultze, M. Hofstetter, V. S. Yakovlev, J. Gagnon, M. Uiberacker, A. L. Aquila, E. M. Gullikson, D. T. Attwood, R. Kienberger, F. Krausz, and U. Kleineberg, *Single-cycle nonlinear optics*, *Science* **320** (2008) 1614–1617.

[60] M. Drescher, M. Hentschel, R. Kienberger, M. Uiberacker, V. Yakovlev, A. Scrinzi, T. Westerwalbesloh, U. Kleineberg, U. Heinzmann, and

F. Krausz, *Time-resolved atomic inner-shell spectroscopy*, *Nature* **419** (2002) 803–807.

[61] N. Milosevic, P. B. Corkum, and T. Brabec, *How to use lasers for imaging attosecond dynamics of nuclear processes*, *Phys. Rev. Lett.* **92** (2004) 013002.

[62] M. Uiberacker, T. Uphues, M. Schultze, A. J. Verhoef, V. Yakovlev, M. F. Kling, J. Rauschenberger, N. M. Kabachnik, H. Schroder, M. Lezius, K. L. Kompa, H.-G. Muller, M. J. J. Vrakking, S. Hendel, U. Kleineberg, U. Heinzmann, M. Drescher, and F. Krausz, *Attosecond real-time observation of electron tunnelling in atoms*, *Nature* **446** (2007) 627–632.

[63] P. Eckle, M. Smolarski, P. Schlup, J. Biegert, A. Staudte, M. Schoffler, H. G. Muller, R. Dorner, and U. Keller, *Attosecond angular streaking*, *Nature Phys.* **4** (2008) 565–570.

[64] J. A. Armstrong, *Measurement of picosecond laser pulse widths*, *Appl. Phys. Lett.* **10** (1967) 16–18.

[65] D. J. Kane and R. Trebino, *Characterization of arbitrary femtosecond pulses using frequency-resolved optical gating*, *IEEE J. Quantum Electron.* **29** (1993) 571–579.

[66] C. Iaconis and I. Walmsley, *Spectral phase interferometry for direct electric-field reconstruction of ultrashort optical pulses*, *Opt. Lett.* **23** (1998) 792–794.

[67] K. Osvay, M. Görbe, C. Grebing, and G. Steinmeyer, *Bandwidth-independent linear method for detection of the carrier-envelope offset phase*, *Opt. Lett.* **32** (2007) 3095–3097.

[68] P. Jójárt, A. Börzsönyi, B. Borchers, G. Steinmeyer, and K. Osvay, *Agile linear interferometric method for carrier-envelope phase drift measurement*, *Opt. Lett.* **37** (2012) 836–838.

[69] T. Fuji, J. Rauschenberger, C. Gohle, A. Apolonski, T. Udem, V. S. Yakovlev, G. Tempea, T. W. Hänsch, and F. Krausz, *Attosecond control of optical waveforms*, *New J. Phys.* **7** (2005) 116.

[70] J.-h. Lee, Y. S. Lee, J. Park, T. J. Yu, and C. H. Nam, *Long-term carrier-envelope-phase stabilization of a femtosecond laser by the direct locking method*, *Opt. Express* **16** (2008) 12624–12631.

[71] T. J. Yu, K.-H. Hong, H.-G. Choi, J. H. Sung, I. W. Choi, D.-K. Ko, J. Lee, J. Kim, D. E. Kim, and C. H. Nam, *Precise and long-term stabilization of the carrier-envelope phase of femtosecond laser pulses using an enhanced direct locking technique*, *Opt. Express* **15** (2007) 8203–8211.

[72] A. Baltuška, T. Fuji, and T. Kobayashi, *Controlling the carrier-envelope phase of ultrashort light pulses with optical parametric amplifiers*, *Phys. Rev. Lett.* **88** (2002) 133901.

[73] J. A. Armstrong, N. Bloembergen, J. Ducuing, and P. S. Pershan, *Interactions between light waves in a nonlinear dielectric*, *Phys. Rev.* **127** (1962) 1918–1939.

[74] M. Bellini and T. W. Hänsch, *Phase-locked white-light continuum pulses: toward a universal optical frequency-comb synthesizer*, *Opt. Lett.* **25** (2000) 1049–1051.

[75] F. Lücking, A. Assion, A. Apolonski, F. Krausz, and G. Steinmeyer, *Long-term carrier-envelope-phase-stable few-cycle pulses by use of the feed-forward method*, *Opt. Lett.* **37** (2012) 2076–2078.

[76] M. Mehendale, S. A. Mitchell, J.-P. Likforman, D. M. Villeneuve, and P. B. Corkum, *Method for single-shot measurement of the carrier envelope phase of a few-cycle laser pulse*, *Opt. Lett.* **25** (2000) 1672–1674.

[77] M. Kakehata, H. Takada, Y. Kobayashi, K. Torizuka, Y. Fujihira, T. Homma, and H. Takahashi, *Single-shot measurement of carrier-envelope phase changes by spectral interferometry*, *Opt. Lett.* **26** (2001) 1436–1438.

[78] S. Koke, C. Grebing, B. Manschwetus, and G. Steinmeyer, *Fast f-to-2f interferometer for a direct measurement of the carrier-envelope phase drift of ultrashort amplified laser pulses*, *Opt. Lett.* **33** (2008) 2545–2547.

[79] C. Lemell, X.-M. Tong, F. Krausz, and J. Burgdörfer, *Electron emission from metal surfaces by ultrashort pulses: Determination of the carrier-envelope phase*, *Phys. Rev. Lett.* **90** (2003) 076403.

[80] A. Apolonski, P. Dombi, G. G. Paulus, M. Kakehata, R. Holzwarth, T. Udem, C. Lemell, K. Torizuka, J. Burgdörfer, T. W. Hänsch, and F. Krausz, *Observation of light-phase-sensitive photoemission from a metal*, *Phys. Rev. Lett.* **92** (2004) 073902.

[81] G. G. Paulus, F. Lindner, H. Walther, A. Baltuška, E. Goulielmakis, M. Lezius, and F. Krausz, *Measurement of the phase of few-cycle laser pulses*, *Phys. Rev. Lett.* **91** (2003) 253004.

[82] T. Wittmann, B. Horvath, W. Helml, M. G. Schätzel, X. Gu, A. L. Cavalieri, G. G. Paulus, and R. Kienberger, *Single-shot carrier-envelope phase measurement of few-cycle laser pulses*, *Nature Phys.* **5** (2009) 357–362.

[83] A. M. Sayler, T. Rathje, W. Müller, K. Rühle, R. Kienberger, and G. G. Paulus, *Precise, real-time, every-single-shot, carrier-envelope phase measurement of ultrashort laser pulses*, *Opt. Lett.* **36** (2011) 1–3.

[84] T. Paasch-Colberg, A. Schiffrin, N. Karpowicz, S. Kruchinin, S. Özge, S. Keiber, O. Razskazovskaya, S. Muhlbrandt, A. Alnaser, M. Kubel, V. Apalkov, D. Gerster, J. Reichert, T. Wittmann, J. V. Barth, M. I. Stockman, R. Ernstorfer, V. S. Yakovlev, R. Kienberger, and F. Krausz, *Solid-state light-phase detector*, *Nature Photon. - advance online publication* (2014).

[85] J. H. Marburger, *Self-focusing: theory*, *Prog. Quantum Electron.* **4** (1975) 35.

[86] L. V. Keldysh, *Ionization in the field of a strong electromagnetic wave*, *Sov. Phys. JETP* **20** (1965) 1307–1314.

[87] A. M. Perelomov, V. S. Popov, and M. V. Terent'ev, *Ionization of atoms in alternating electric field*, *Sov. Phys. JETP* **23** (1966) 924–934.

[88] R. H. Stolen and C. Lin, *Self-phase-modulation in silica optical fibers*, *Phys. Rev. A* **17** (1978) 1448–1453.

[89] F. DeMartini, C. H. Townes, T. K. Gustafson, and P. L. Kelley, *Self-steepening of light pulses*, *Phys. Rev.* **164** (1967) 312–323.

[90] M. Sheik-Bahae, D. C. Hutchings, D. J. Hagan, and E. W. Van Stryland, *Dispersion of bound electron nonlinear refraction in solids*, *IEEE J. Quantum Electron.* **27** (1991) 1296–1309.

[91] A. L. Gaeta, *Catastrophic collapse of ultrashort pulses*, *Phys. Rev. Lett.* **84** (2000) 3582–3585.

[92] V. Loriot, E. Hertz, O. Faucher, and B. Lavorel, *Measurement of high order Kerr refractive index of major air components*, *Opt. Express* **17** (2009) 13429–13434.

[93] C. Brée, A. Demircan, and G. Steinmeyer, *Saturation of the all-optical Kerr effect*, *Phys. Rev. Lett.* **106** (2011) 183902.

[94] J. K. Wahlstrand and H. M. Milchberg, *Effect of a plasma grating on pump-probe experiments near the ionization threshold in gases*, *Opt. Lett.* **36** (2011) 3822–3824.

[95] B. Borchers, C. Brée, S. Birkholz, A. Demircan, and G. Steinmeyer, *Saturation of the all-optical Kerr effect in solids*, *Opt. Lett.* **37** (2012) 1541–1543.

[96] G. Yang and Y. R. Shen, *Spectral broadening of ultrashort pulses in a nonlinear medium*, *Opt. Lett.* **9** (1984) 510–512.

[97] A. Brodeur and S. L. Chin, *Ultrafast white-light continuum generation and self-focusing in transparent condensed media*, *J. Opt. Soc. Am. B* **16** (1999) 637–650.

[98] J. B. Ashcom, R. R. Gattass, C. B. Schaffer, and E. Mazur, *Numerical aperture dependence of damage and supercontinuum generation from femtosecond laser pulses in bulk fused silica*, *J. Opt. Soc. Am. B* **23** (2006) 2317–2322.

[99] J. C. Knight, T. A. Birks, P. St. J. Russell, and D. M. Atkin, *All-silica single-mode optical fiber with photonic crystal cladding*, *Opt. Lett.* **21** (1996) 1547–1549.

[100] J. K. Ranka, R. S. Windeler, and A. J. Stentz, *Visible continuum generation in air-silica microstructure optical fibers with anomalous dispersion at 800 nm*, *Opt. Lett.* **25** (2000) 25–27.

[101] T. A. Birks, W. J. Wadsworth, and P. S. J. Russell, *Supercontinuum generation in tapered fibers*, *Opt. Lett.* **25** (2000) 1415–1417.

[102] A. V. Husakou and J. Herrmann, *Supercontinuum generation of higher-order solitons by fission in photonic crystal fibers*, *Phys. Rev. Lett.* **87** (2001) 203901.

[103] F. M. Mitschke and L. F. Mollenauer, *Discovery of the soliton self-frequency shift*, *Opt. Lett.* **11** (1986) 659–661.

[104] J. M. Dudley, G. Genty, and S. Coen, *Supercontinuum generation in photonic crystal fiber*, *Rev. Mod. Phys.* **78** (2006) 1135–1184.

[105] A. Apolonski, A. Poppe, G. Tempea, C. Spielmann, T. Udem, R. Holzwarth, T. W. Hänsch, and F. Krausz, *Controlling the phase evolution of few-cycle light pulses*, *Phys. Rev. Lett.* **85** (2000) 740–743.

[106] T. M. Fortier, D. J. Jones, J. Ye, S. T. Cundiff, and R. S. Windeler, *Long-term carrier-envelope phase coherence*, *Opt. Lett.* **27** (2002) 1436–1438.

[107] M. Y. Sander, E. P. Ippen, and F. X. Kärtner, *Carrier-envelope phase dynamics of octave-spanning dispersion-managed Ti: sapphire lasers*, *Opt. Express* **18** (2010) 4948–4960.

[108] L. Matos, O. D. Mücke, J. Chen, and F. X. Kärtner, *Carrier-envelope phase dynamics and noise analysis in octave-spanning Ti:sapphire lasers*, *Opt. Express* **14** (2006) 2497–2511.

[109] P. Horowitz and W. Hill, *The Art of Electronics.* Cambridge University Press, Cambridge, UK, 2nd ed., July, 1989.

[110] R. W. Dixon, *Photoelastic properties of selected materials and their relevance for applications to acoustic light modulators and scanners*, *J. Appl. Phys.* **38** (1967) 5149–5153.

[111] E. Benkler, H. R. Telle, K. Weingarten, L. Krainer, G. Spühler, and U. Keller, *Characterization of ultrashort optical pulse properties by amplitude-modulation-balanced heterodyne gating*, *Opt. Lett.* **30** (2005) 2016–2018.

[112] G. Gademann, F. Plé, P.-M. Paul, and M. J. J. Vrakking, *Carrier-envelope phase stabilization of a terawatt level chirped pulse amplifier for generation of intense isolated attosecond pulses*, *Opt. Express* **19** (2011) 24922–24932.

[113] J.-F. Hergott, O. Tcherbakoff, P.-M. Paul, P. Demengeot, M. Perdrix, F. Lepetit, D. Garzella, D. Guillaumet, M. Comte, P. D. Oliveira, and O. Gobert, *Carrier-envelope phase stabilization of a 20 W, grating based, chirped-pulse amplified laser, using electro-optic effect in a $LiNbO_3$ crystal*, *Opt. Express* **19** (2011) 19935–19941.

[114] T. M. Fortier, J. Ye, S. T. Cundiff, and R. S. Windeler, *Nonlinear phase noise generated in air-silica microstructure fiber and its effect on carrier-envelope phase*, *Opt. Lett.* **27** (2002) 445–447.

[115] A. Baltuška, M. Uiberacker, E. Goulielmakis, R. Kienberger, V. S. Yakovlev, T. Udem, T. W. Hänsch, and F. Krausz, *Phase-controlled amplification of few-cycle laser pulses*, *IEEE J. Sel. Top. Quantum Electron.* **9** (2003) 972 – 989.

[116] N. Haverkamp and H. R. Telle, *Complex intensity modulation transfer function for supercontinuum generation in microstructure fibers*, *Opt. Express* **12** (2004) 582–587.

[117] B. Washburn and N. Newbury, *Phase, timing, and amplitude noise on supercontinua generated in microstructure fiber*, *Opt. Express* **12** (2004) 2166–2175.

[118] M. Pawlowska, F. Ozimek, P. Fita, and C. Radzewicz, *Collinear interferometer with variable delay for carrier-envelope offset frequency measurement*, *Rev. Sci. Instrum.* **80** (2009) 083101.

[119] C. Grebing, S. Koke, B. Manschwetus, and G. Steinmeyer, *Performance comparison of interferometer topologies for carrier-envelope phase detection*, *Appl. Phys. B* **95** (2009) 81–84.

[120] S. Koke, *Fundamental limitations in the measurement and stabilization of the Carrier-envelope phase of ultrashort laser pulses.* PhD thesis, Humboldt-University, Berlin, 2011.

[121] B. Borchers, S. Koke, A. V. Husakou, J. Herrmann, and G. Steinmeyer, *Carrier-envelope phase stabilization with sub-10 as residual timing jitter*, *Opt. Lett.* **36** (2011) 4146–4148.

[122] N. Campbell, *The study of discontinuous phenomena*, *Math. Proc. Cambridge Phil. Soc.* **15** (1909) 117–136.

[123] W. Schottky, *Über spontane Stromschwankungen in verschiedenen Elektrizitätsleitern*, *Ann. Physik* **57** (1918) 541.

[124] S. Rice, *Mathematical analysis of random noise*, *Bell Syst. Tech. J.* **23** (1944) 282–332.

[125] E. N. Gilbert and H. O. Pollak, *Amplitude distribution of shot noise*, *Bell Syst. Tech. J.* **39** (1960) 333.

[126] R. J. Glauber, *Coherent and incoherent states of the radiation field*, *Phys. Rev.* **131** (1963) 2766.

[127] D. F. Walls, *Squeezed states of light*, *Nature* **306** (1983) 141–146.

[128] M. Takeda, H. Ina, and S. Kobayashi, *Fourier-transform method of fringe-pattern analysis for computer-based topography and interferometry*, *J. Opt. Soc. Am.* **72** (1982) 156–160.

[129] A. V. Husakou and J. Herrmann, *Supercontinuum generation, four-wave mixing, and fission of higher-order solitons in photonic-crystal fibers*, *J. Opt. Soc. Am. B* **19** (2002) 2171–2182.

[130] R. Paschotta, *Timing jitter and phase noise of mode-locked fiber lasers*, *Opt. Express* **18** (2010) 5041–5054.

[131] C.-C. Lee, C. Mohr, J. Bethge, S. Suzuki, M. E. Fermann, I. Hartl, and T. R. Schibli, *Frequency comb stabilization with bandwidth beyond the limit of gain lifetime by an intracavity graphene electro-optic modulator*, *Opt. Lett.* **37** (2012) 3084–3086.

[132] D. R. Herriott and H. J. Schulte, *Folded optical delay lines*, *Appl. Opt.* **4** (1965) 883–889.

[133] A. Baltuška, T. Udem, M. Uiberacker, M. Hentschel, E. Goulielmakis, C. Gohle, R. Holzwarth, V. S. Yakovlev, A. Scrinzi, T. W. Hänsch, and F. Krausz, *Attosecond control of electronic processes by intense light fields*, *Nature* **421** (2003) 611–615.

[134] M. G. Schätzel, F. Lindner, G. G. Paulus, H. Walther, E. Goulielmakis, A. Baltuška, M. Lezius, and F. Krausz, *Long-term stabilization of the carrier-envelope phase of few-cycle laser pulses*, *Appl. Phys. B* **79** (2004) 1021–1025.

[135] C. Li, E. Moon, H. Mashiko, C. M. Nakamura, P. Ranitovic, C. M. Maharjan, C. L. Cocke, Z. Chang, and G. G. Paulus, *Precision control of carrier-envelope phase in grating based chirped pulse amplifiers*, *Opt. Express* **14** (2006) 11468–11476.

[136] F. Verluise, V. Laude, Z. Cheng, C. Spielmann, and P. Tournois, *Amplitude and phase control of ultrashort pulses by use of an acousto-optic programmable dispersive filter: pulse compression and shaping*, *Opt. Lett.* **25** (2000) 575–577.

[137] N. Forget, L. Canova, X. Chen, A. Jullien, and R. Lopez-Martens, *Closed-loop carrier-envelope phase stabilization with an acousto-optic programmable dispersive filter*, *Opt. Lett.* **34** (2009) 3647–3649.

[138] O. Gobert, P. M. Paul, J. F. Hergott, O. Tcherbakoff, F. Lepetit, P. D. 'Oliveira, F. Viala, and M. Comte, *Carrier-envelope phase control using linear electro-optic effect*, *Opt. Express* **19** (2011) 5410–5418.

[139] R. DeSalvo, A. A. Said, D. J. Hagan, E. W. Van Stryland, and M. Sheik-Bahae, *Infrared to ultraviolet measurements of two-photon absorption and n_2 in wide bandgap solids*, *IEEE J. Quantum Electron.* **32** (1996) 1324–1333.

[140] M. Sheik-Bahae, A. A. Said, and E. W. Van Stryland, *High-sensitivity, single-beam n_2 measurements*, *Opt. Lett.* **14** (1989) 955–957.

[141] G. Sansone, E. Benedetti, J.-P. Caumes, S. Stagira, C. Vozzi, S. De Silvestri, and M. Nisoli, *Control of long electron quantum paths in high-order harmonic generation by phase-stabilized light pulses*, *Phys. Rev. A* **73** (2006) 053408.

[142] M. Kakehata, Y. Fujihira, H. Takada, Y. Kobayashi, K. Torizuka, T. Homma, and H. Takahashi, *Measurements of carrier-envelope phase changes of 100-Hz amplified laser pulses*, *Appl. Phys. B* **74** (2002) 43–50.

[143] B. Borchers, F. Lücking, and G. Steinmeyer, *Acoustic frequency combs for carrier-envelope phase stabilization*, *Opt. Lett.* **39** (2014) 544–547.

[144] M. Bradler, P. Baum, and E. Riedle, *Femtosecond continuum generation in bulk laser host materials with sub-μJ pump pulses*, *Appl. Phys. B* **97** (2009) 561–574.

[145] M. Mero, J. Liu, W. Rudolph, D. Ristau, and K. Starke, *Scaling laws of femtosecond laser pulse induced breakdown in oxide films*, *Phys. Rev. B* **71** (2005) 115109.

[146] L. Bergé and S. Skupin, *Self-channeling of ultrashort laser pulses in materials with anomalous dispersion*, *Phys. Rev. E* **71** (2005) 065601.

[147] V. G. Dmitriev, G. G. Gurzadyan, and D. N. Nikogosyan, *Handbook of nonlinear optical crystals*. Springer, Berlin, 3rd ed., 1999.

[148] M. Iwai, T. Yoshino, S. Yamaguchi, M. Imaeda, N. Pavel, I. Shoji, and T. Taira, *High-power blue generation from a periodically poled $MgO:LiNbO_3$ ridge-type waveguide by frequency doubling of a diode end-pumped $Nd:Y_3Al_5O_{12}$ laser*, *Appl. Phys. Lett.* **83** (2003) 3659–3661.

[149] A. V. Smith, R. J. Gehr, and M. S. Bowers, *Numerical models of broad-bandwidth nanosecond optical parametric oscillators*, *J. Opt. Soc. Am. B* **16** (1999) 609–619.

[150] J. Herrmann, U. Griebner, N. Zhavoronkov, A. Husakou, D. Nickel, J. C. Knight, W. J. Wadsworth, P. St. J. Russell, and G. Korn, *Experimental evidence for supercontinuum generation by fission of higher-order solitons in photonic fibers*, *Phys. Rev. Lett.* **88** (2002) 173901.

[151] F. Lindner, G. G. Paulus, F. Grasbon, A. Dreischuh, and H. Walther, *Dispersion control in a 100-kHz-repetition-rate 35-fs Ti:sapphire regenerative amplifier system*, *IEEE J. Quantum Electron.* **38** (2002) 1465 – 1470.

[152] E. Goulielmakis, S. Koehler, B. Reiter, M. Schultze, A. J. Verhoef, E. E. Serebryannikov, A. M. Zheltikov, and F. Krausz, *Ultrabroadband, coherent light source based on self-channeling of few-cycle pulses in helium*, *Opt. Lett.* **33** (2008) 1407–1409.

[153] Y.-H. Cheng, J. K. Wahlstrand, N. Jhajj, and H. M. Milchberg, *The effect of long timescale gas dynamics on femtosecond filamentation*, *Opt. Express* **21** (2013) 4740–4751.

[154] N. Jhajj, Y.-H. Cheng, J. K. Wahlstrand, and H. M. Milchberg, *Optical beam dynamics in a gas repetitively heated by femtosecond filaments*, *Optics Express* **21** (2013) 28980–28986.

[155] N. Jhajj, E. W. Rosenthal, R. Birnbaum, J. K. Wahlstrand, and H. M. Milchberg, *Demonstration of long-lived high-power optical waveguides in air*, *Phys. Rev. X* **4** (2014) 011027.

Selbständigkeitserklärung

Hiermit erkläre ich, die vorliegende Arbeit selbständig und nur unter Verwendung der angegebenen Literatur und Hilfsmittel angefertigt zu haben.

Ich habe mich anderwärts nicht um einen Doktorgrad beworben und besitze keinen entsprechenden Doktorgrad.

Desweiteren erkläre ich die Kenntnisnahme der dem Verfahren zugrunde liegenden Promotionsordnung der Mathematisch-Naturwissenschaftlichen Fakultät der Humboldt-Universität zu Berlin.

Berlin, den 20.05.2014 Bastian Borchers